Aaron Taylor
Candidate

Physics and Astronomy
Department

This dissertation is approved, and it is acceptable in quality and form for publication:

Approved by the Dissertation Committee:

Dr. Sally Seidel , Chairperson

Dr. Pavel Reznicek

Dr. Huaiyu Duan

Dr. Douglas Fields

Dr. Bruce Schumm

SEARCH FOR NEW PHYSICS PROCESSES WITH HEAVY QUARK SIGNATURES IN THE ATLAS EXPERIMENT

by

AARON TAYLOR

B.A., Mathematics, University of California, Santa Cruz, 2011
M.S., Physics, University of New Mexico, 2014

DISSERTATION

Submitted in Partial Fulfillment of the
Requirements for the Degree of

Doctor of Philosophy
Physics

The University of New Mexico
Albuquerque, New Mexico

May, 2017

Acknowledgements

I would like to thank Professor Sally Seidel, for her constant support and guidance in my research. I would also like to thank her for her patience in helping me to develop my technical writing and presentation skills; without her assistance, I would never have gained the skill I have in that field.

I would like to thank Konstantin Toms, for his constant assistance with the ATLAS code, and for generally giving advice on how to handle data analysis. The $B_s \rightarrow 4\mu$ analysis likely wouldn't have gotten anywhere without him.

I would like to deeply thank Pavel Reznicek, without whom I would never have gotten as great an understanding of ATLAS code as I currently have. It is no exaggeration to say that I would not have been half as successful as I have been without his constant patience and understanding. Thank you.

Many thanks to Martin Hoeferkamp, who taught me much about instrumentation and physical measurements. I would also like to thank him for his work on the diode array, for which I only designed the controlling software.

I would like to thank Bruce Schumm and Vitaliy Fadeyev, faculty at UCSC. They assisted me greatly in completing my undergraduate research work, and helped me find my place in graduate school.

Finally, I would like to thank my mother and family for their unconditional love and support for these last years.

Search for New Physics Processes with Heavy Quark Signatures in the ATLAS Experiment

by

Aaron Taylor

B.A., Mathematics, University of California, Santa Cruz, 2011

M.S., Physics, University of New Mexico, 2014

Ph.D., Physics, University of New Mexico, 2017

Abstract

A program involving searches for new physics with heavy quark final states using data from the ATLAS experiment at the LHC is presented here. The signal and expected backgrounds for the decay $B_s \rightarrow \mu^+\mu^-\mu^+\mu^-$, a rare decay whose branching ratio may be enhanced by the presence of certain Beyond the Standard Model processes, are studied, and the groundwork is laid for a future analysis. Possible mediators include horizontal gauge bosons, supersymmetry via sgoldstinos, and interactions with the hidden sector. To this end, a set of twelve triggers have been selected and studied, and their efficiency figures of merit have been calculated. A truth trigger efficiency study was performed in order to determine if new triggers should be installed for the analysis. The backgrounds have been studied, and a mass window technique was used to reduce their amplitude

relative to the signal. A proposal to improve the efficiency of some of the ATLAS High-Level B-physics Triggers, based on refining the selection criteria for the quality of the fit for $J/\psi \rightarrow \mu^+\mu^-$ vertices, was developed. A new J/ψ vertex fit χ^2 selection criterion was developed using Run-1 triggers, reducing the original $\chi^2 < 20$ criterion to $\chi^2 < 10$. This was installed for Run-2 data-taking. A similar study was performed on Run-2 data, and signal efficiency, background rejection, and Receiver Operating Characteristic plots were generated for these data. Instrumentation for future ATLAS runs has been developed as well, including software for a diode array used to measure charged particle beam fluence in real time. Noise reduction studies of a device for studying charge collection in irradiated particle sensors was performed, and it was determined that the noise might be decreased by an additional electronic noise filter.

Table of Contents

List of Figures

List of Tables

Chapter 1: Introduction

The quest to understand the universe is a fundamental part of human nature. Numerous theories have been made for this purpose. One of the oldest is that of the philosopher Democritus, who, along with his mentor Leucippus, came up with the idea of atoma, "unsplittable ones." These were the smallest possible unit of matter, a chunk of mass that was indestructible, solid, invisible, and internally homogeneous. Of course, in the modern day atoms can be split quite easily, demonstrating the progression of human knowledge. In the modern day, the primary theory of fundamental matter is the Standard Model of Particle Physics (SM), a highly successful physical theory to which thus far only one contradiction has been observed, the non-zero mass of neutrinos. The SM describes objects even smaller than the atom, including the nucleons, residing at the atom's core, and the electrons, surrounding the nucleus in a cloud. It goes even deeper, however: the SM describes the constituents of the nucleons, the up and down valence quarks that compose the proton and neutron, and four other quarks besides, the charm, strange, bottom, and top quarks. It also describes five leptons other than the electron, including the muon, tau, and three neutrinos each corresponding to a charged lepton, and five bosons, including the photon, Z, $W^{\pm}$, and Higgs boson. There are several phenomena that the Standard Model does not adequately describe, such as the matter-antimatter asymmetry, the mass of the neutrino, the nature of gravity, and dark matter. It is the purpose of one of the studies presented here to attempt to use certain rare interactions of the bottom quark to seek physics beyond this Standard Model.

This search for physics beyond the Standard Model examines the rate of the process $B_s \rightarrow \mu^+\mu^-\mu^+\mu^-$. In the text that follows, this decay will sometimes be referred to as $B_s \rightarrow 4\mu$. Under the Standard Model (see Chapter 2), this decay is very rare, but several theories suggest mechanisms that could enhance this decay significantly, such as certain forms of supersymmetry, horizontal gauge bosons, and the hidden sector. Details on the theory can be found in Chapter 4; a description of preparations for the search itself can be found in Chapter 5.

The pursuit of understanding of the universe requires a variety of complex instruments. One of these is the Large Hadron Collider (LHC) at CERN, the largest particle collider in the world. All studies in this dissertation focus on data from ATLAS, one of the four main detectors attached to the LHC. More details can be found in Chapter 3.

The ATLAS detector is a complex instrument that acquires and processes an extraordinary amount of data every second. In order for the most important data to be processed and stored for later analysis, ATLAS uses a triggering system, which examines events and discards the unwanted data. Chapter 6 describes a project in which the ATLAS High-Level Trigger system is studied, leading to a proposal of a means to increase the efficiency for which interesting data are accepted, less interesting data rejected.

High-energy physics, and b-quark physics especially, need a great deal of data for analyses to be performed; this means that accelerators, such as the LHC, need to be run for a long time at high energies to get the necessary integrated luminosity. Consequently, experiments such as ATLAS demand instrumentation that can survive the extreme radiation environment near the collision point. To this end, new experimental materials and devices, need to be studied to determine if they are compatible with integration into

ATLAS. Many of these technologies are intended for the Inner Detector, data from which is used to study b-physics, and on which the $B_s \rightarrow 4\mu$ study depends. These devices need to be tested for their performance in high-radiation environments by irradiating them in particle beams in other facilities around the world. One such facility is at Los Alamos, where devices from research groups around the world are irradiated in its 800 MeV proton test beam. To facilitate this irradiation, it is necessary to understand the profile and fluence of the beam; to this end, a diode array capable of measuring these quantities in real-time has been developed. Understanding the charge collection in irradiated sensors is a related topic of importance, and efforts to improve an instrument for detecting that charge are described. Details can be found in Chapter 7.

Chapter 8 contains an overview of the results found throughout this dissertation. It also contains an analysis of the applications of those results, and future studies that can be performed on those topics.

Appendix A includes all the parameters used for the fit of the reconstructed K^*, B_d, and B_s invariant mass distributions, which are otherwise detailed in Chapter 5.

Chapter 2: Theoretical Background

2.1 Introduction

As the major study in this dissertation involves a study of a Standard Model decay, and a search for physics beyond the Standard Model, an overview of the SM is necessary. Presented here is a brief description of the parts of the Standard Model relevant to this study.

2.2 The Standard Model

The Standard Model is a highly successful theory of particle physics, and it composes all of modern understanding of subatomic particle structure. It describes the fundamental interactions between the elementary particles via the electromagnetic, weak, and strong force carriers; the gravitational interaction is not included in this description. It first took form in 1961, with Sheldon Glashow's discovery[1] of a way to combine the electromagnetic and weak interactions in the energy regime above 100 GeV. In 1967, Steven Weinberg incorporated[2] the Higgs mechanism[3] into this electroweak theory. When the neutral weak currents were discovered[4] in 1973 at CERN, the description of the strong interaction acquired its modern form, and when the existence of fractionally-charged particles (quarks) within nucleons was confirmed[5], the Standard Model attained its current form. The discovery of the Higgs boson in 2012 by ATLAS[6] and CMS[7] at the LHC is the crowning achievement of the Standard Model, demonstrating its self-consistency and accuracy.

The Standard Model states that matter is made of, and forces are carried by, two types of particles: the fermions (half-spin particles), and the bosons (integer spin particles). Fermions, both quarks and leptons, are observed in three generations. Every individual fermion has an associated antiparticle, with which it can annihilate, converting both from matter into energy. Bosons have been observed with two spins, the spin-1 gauge bosons and the spin-0 Higgs boson. A schematic picture of all these particles can be seen in Figure 1.

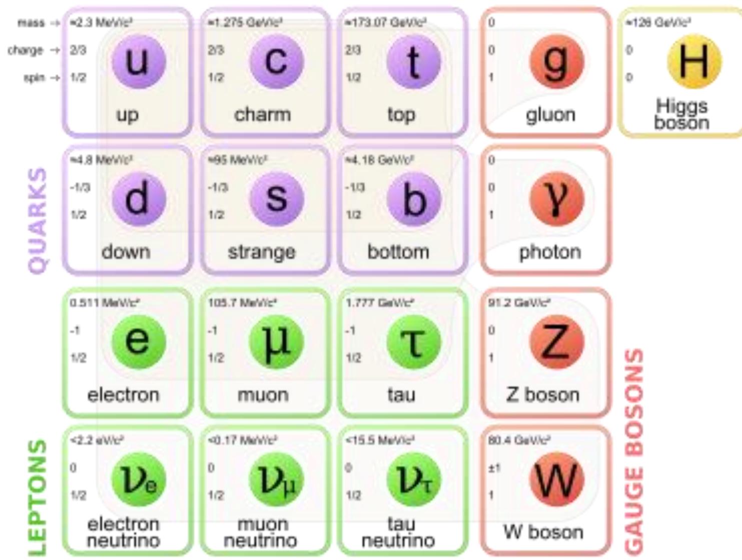

Figure 1: The particles composing the Standard Model, arranged by generation and spin. From [8].

The Standard Model describes particle interactions in the form of gauge symmetry in $SU(3)_C \times SU(2)_W \times U(1)_Y$, and the invariance under this theory leads to renormalizability. The indices refer to the quantities each transformation conserves: Color (C) in SU(3), weak isospin (W) in SU(2) (although only for left-handed particles), and weak hypercharge (Y) in U(1). These gauge symmetries give rise to the three fundamental interactions, electromagnetism, weak, and strong. The Higgs boson gives rise to mass by way of spontaneous electroweak symmetry breaking. While the Higgs potential is invariant with respect to transformations under electroweak symmetry, the minimum of the potential is situated at a non-zero field value, the vacuum expectation value, which enables the spontaneous break in symmetry.

The Standard Model accurately describes a wide variety of experimental results. It doesn't describe gravity, neutrino mass, the degree of matter-antimatter asymmetry present in the universe, dark matter, and the cause of the accelerating expansion of the universe (often attributed to dark energy).

2.3 Elementary Particles and Force Carriers

2.3.1 Fermions

Fermions have twelve flavors, split into three generations and two types. Each of the three generations is a doublet of two quarks, one with a charge q of +2/3 of the elementary charge e and one with a charge q of -1/3, and two leptons, a negatively-charged ($q = -1$) particle and an associated neutrino. Each progressive generation of quarks and charged leptons is composed of particles of increasing mass and decreasing stability. The mass of individual neutrinos isn't well-understood and may or may not increase with generation, although it is known that they are stable.

Quarks are the fundamental particles that compose all hadronic matter, and they interact by the strong, weak, and electromagnetic forces. Quarks have never been observed outside of bound states, and this observation has been incorporated into the theoretical description of the strong force. The quarks of the first generation are the up ($q = +2/3$) and down ($q = -1/3$) quarks; of the second, the charm ($q = +2/3$) and strange ($q = -1/3$) quarks; and of the third, the top ($q = +2/3$) and bottom ($q = -1/3$) quarks. They range in mass from 2.3 MeV (up) to 173.07 GeV (top)[9].

The leptons include the negatively-charged electrons, muons, and tau, along with their associated (uncharged) neutrinos (called electron neutrino, etc.). As with quarks, leptons occur in three generations, composed of the doublets electron and electron neutrino, muon and muon neutrino, and tau and tau neutrino. As with the quarks, the mass of the charged leptons increases with generation, and their stability decreases. Their masses range from 0.511 MeV (electron), to 105.7 MeV (muon), to 1.777 GeV (tau). The (first-generation) electron is stable, with a lifetime exceeding 4.6 x 10^{26} years, while the (third-generation) tau has a lifetime of ~2.9 x 10^{-13} seconds[9]. The neutrinos are ultra-low mass particles that transmit lepton number and energy in weak interactions. Their lack of charge and nature as leptons make them immune to strong and electromagnetic interactions, leaving them to only be affected by the weak and gravitational forces. The weak coupling of the weak interaction means that neutrinos can pass through vast amounts of matter unaffected. In 2001, neutrinos were discovered to oscillate[10], such that a produced electron neutrino might arrive elsewhere as a muon or tau neutrino; this is a consequence of a mixture between neutrino mass eigenstates, i.e. the three neutrino states that interact with charged leptons are actually each a different superposition of the three neutrino mass eigenstates. Neutrino oscillation is not explained in the SM.

2.3.2 Bosons

Bosons do not form generations. Bosons transmit the electromagnetic, weak, and strong forces; no particle has been discovered that carries gravity, although the existence of a graviton has been hypothesized since the 1930s[11]. The gauge bosons come in three types:

- The photon is a massless boson that mediates the electromagnetic force between charged particles; particles with no charge do not interact with the photon at first order. The process of its interaction is described by quantum electrodynamics (QED).
- The $W^{\pm}$ and Z^0 bosons are massive bosons that mediate the weak interaction between fermions. Their mass is due to the breaking of $SU(2)_L \times U(1)_Y$ symmetry, which also serves to limit the range of the weak interaction to ~10^{-18} m, less than a thousandth of the diameter of a proton. The W^+ and W^- are antiparticles of each other, and act only on left-handed particles and right-handed antiparticles. They are further involved in lepton and neutrino absorption/emission, and as a consequence play a significant role in nuclear decays. The Z^0 boson does not carry quark or lepton numbers and has no electric charge; it mediates the transfer of momentum, energy, and spin between quarks, leptons, and neutrinos in weak interactions. These bosons can couple with each other in a WWZ vertex, or with photons in a WWZγ vertex.
- Gluons are massless bosons that mediate the strong force, the interaction between color-charged quarks in baryons and mesons. Gluons carry color charge, and as a consequence can interact with other gluons; these processes are described by the theory of Quantum Chromodynamics (QCD).
- Finally, the Higgs boson is a massive (~126 GeV)[6], spinless, charge-neutral particle that gives rise to the mass of fermions and weak bosons alike. The Higgs boson is estimated to have a very short lifetime (~1.56×10^{-22} seconds)[12] and can

interact with itself. The Higgs was first observed by both ATLAS and CMS in 2012[6,7].

2.3.3 Quantum Chromodynamics

The B_s meson is a strongly bound system; the theory of this interaction will thus be provided here. Quantum Chromodynamics is the $SU(3)_C$ portion of the Standard Model that describes strong interactions. QCD adds a quantum number, called color charge, which was originally invented to explain how quarks could exist in hadrons without violating the Pauli Exclusion Principle. It has three values: red, green, and blue, with the combination of the three (red + green + blue) being colorless. The colors also have associated anti-colors, with quarks carrying color and anti-quarks anti-color; a color and its anti-color together make a color-neutral bound state. In QCD, hadrons are color-neutral; baryons are linear superpositions of several different three-quark states with no net color. Mesons have one quark with color and the other with the corresponding anti-color, permitting the same. As the generators of the $SU(3)_C$ symmetry group, gluons form a color octet, where all eight color-anticolor linear combinations are orthogonal.

QCD has two properties that set it apart from Quantum Electrodynamics: confinement and asymptotic freedom. The property of confinement states that the force of attraction between quarks (the strong force) does not diminish with distance; the further the quarks separate, the more potential energy exists in the gluon field between them. Eventually, with continued separation of the quarks, this field gains so much energy that it converts into a new quark-antiquark pair; this will continue until the resulting group of bound particles is color-neutral. Confinement prevents non-neutral color states from existing in nature. When a colored bound state is produced, it undergoes fragmentation and hadronizes by pulling additional quark pairs from the vacuum to form color-neutral bound states. Asymptotic freedom is the property that in very high-energy reactions, quarks and gluons interact only very weakly. In other words, the strong coupling decreases as the interaction distance becomes smaller, allowing one to treat a hadron's component quarks as essentially free particles when studying certain interactions.

2.4 Hadrons

The $B_s \rightarrow 4\mu$ decay and its backgrounds involve production of hadrons, both in the initial particle and in some of the decay products; thus, an overview of hadrons is provided here. The structure of hadrons, both the three-quark baryons and the two-quark mesons, is described in what is known as the Quark Model[13]. This model was developed as many hadrons were being discovered, and it was speculated that they could not all be elementary particles. The three lightest quarks can be modeled by SU(3) flavor symmetry, also known as the Eightfold Way[14]. The triplet state acts as the fundamental building block of SU(3) symmetry. Every quark is assigned spin-1/2 and a baryon number B of 1/3, while antiquarks have a baryon number of -1/3. As a result, baryons, which have a baryon number of ±1, can only be constructed from three quarks or three antiquarks; and mesons, which have a baryon number of 0, can only be constructed from a quark and an antiquark.

Hadrons also possess the hypercharge quantum number Y, defined as:

$$Y = S + C + B' + T + B$$

where S is the strangeness, C the charm, B' the bottomness, T the topness, and B the baryon number of the quark. The terms S, C, B', and T are conserved under the strong and electromagnetic interactions, but not the weak interaction, as is the hypercharge Y; the conservation of the baryon number B follows from this. The charge Q of the particle is then defined by

$$Q = I_3 + \frac{1}{2}Y$$

where I_3 is the third component of isospin. Isospin is a quantum number related to the strong interaction and its independence of electric charge. Some groups of particles, like protons and neutrons, differ only in charge-related properties. As such, they can be considered different states of the same particle (in the case of the proton and neutron, that particle is the nucleon). The proton is assigned isospin of $I_3 = +1/2$, while the neutron is assigned $I_3 = -1/2$; the proton-neutron composite state thus has a total isospin of $I = 1$ or 0. The mathematical structure used to describe isospin is identical to the quantum mechanical formulation of spin, although isospin has nothing to do with angular momentum, and thus the composite proton(p) -neutron(n) system can be expressed in a singlet and triplet of isospin:

$$\begin{cases} |I = 1, I_3 = +1\rangle = pp \\ |I = 1, I_3 = 0\rangle = \frac{1}{\sqrt{2}}(pn + np) \\ |I = 1, I_3 = -1\rangle = nn \end{cases}$$

$$|I = 0, I_3 = 0\rangle = \frac{1}{\sqrt{2}}(pn - np)$$

Mesons, being composed of one quark and one antiquark, follow Bose-Einstein statistics; mesons have integer spin, and are spin-0 or spin-1 (although higher spins are possible), depending on whether the quarks' spin alignment is parallel or antiparallel. There are five observed types of mesons: scalar (such as the $K_0^*(1430)$), pseudoscalar (such as the π, K and B), pseudovector (such as the $f_1(1285)$, $K_1(1270)$, and χ_{c1}), vector (such as the ω, ρ, and J/ψ), and tensor (such as the $f_2(1270)$). Meson types are described by their parity and their total angular momentum. Parity P is defined for the meson as $P = (-1)^{\ell+1}$, and is defined as +1 for quarks and -1 for antiquarks. Total angular momentum J is defined as $J = L + S$, where L is the total orbital momentum and S the total spin momentum, with its corresponding quantum number j spanning the range $|\ell - s| < j < |\ell + s|$. Scalar mesons have a total spin of 0 and even parity ($J^P = 0^+$), pseudoscalar mesons have a total spin of 0 and odd parity ($J^P = 0^-$), vector mesons have a total spin of 1 and odd parity ($J^P = 1^-$), pseudovector mesons have a total spin of 1 and even parity ($J^P = 1^+$), and tensor mesons have a total spin of 1, a total angular momentum of 2, and even parity ($J^P = 2^+$).

Using the three lightest flavors of quark, there are nine possible quark-antiquark combinations. These nine states form an SU(3) octet and an SU(3) singlet.. The singlet state is a linear combination to which all three quark flavors contribute equally,

$$\psi = \sqrt{\frac{1}{3}}\left(u\bar{u} + d\bar{d} + s\bar{s}\right)$$

2.5 B-Physics

B-physics is the discipline that studies b-hadrons, which are mesons and baryons with at least one bottom quark, and their decays, such as $B_s \rightarrow 4\mu$. The bottom quark was proposed in 1973 by Makoto Kobayashi and Toshihide Maskawa to explain CP violation in the framework of the renormalizable theory of the weak interaction[15]. It was discovered[16] at Fermilab in 1977 by experiment E288. A dimuon resonance had been found at 9.5 GeV, which was discovered to be the decay product of the Upsilon Y, a state of bottomonium ($b\bar{b}$).

2.5.1 Production of b-Quarks at the LHC

In the pp collisions at the LHC, b-quark production results from three subprocesses (examples are shown in Figures 2a, b, and c). They are:

- Flavor creation (FCR), which involves mutual annihilation of two gluons or quarks to produce a heavy quark-antiquark pair. At leading order this process is described by $gg \rightarrow b\bar{b}$ and $q\bar{q} \rightarrow b\bar{b}$.
- Flavor excitation (FEX), which occurs when a $b\bar{b}$ pair from the quark sea of the proton collision gets excited to the final state due to one of the b-quarks undergoing a hard QCD interaction with one of the partons of the other proton.
- Gluon splitting (GSP), which involves a gluon spontaneously decaying into a $b\bar{b}$ pair in the initial or final state, $g \rightarrow b\bar{b}$.

FCR is the leading production method, with a probability proportional to α_s^2. The next most probable contributions, with probability proportional to α_s^3, are FEX and GSP. The high energies of the LHC do not result in a suppression of FEX and GSP by a factor of α_s; rather, they contribute more to b-quark production than FCR, as can be seen in Figure 3. This is due to the fact that, in for example FEX, the $gg \rightarrow gg$ scattering is more strongly favored than $gg \rightarrow q\bar{q}$ by up to two orders of magnitude. Even when it is reduced by a factor of α_s, the contribution from FEX is larger than that from the Leading Order (LO) FCR.

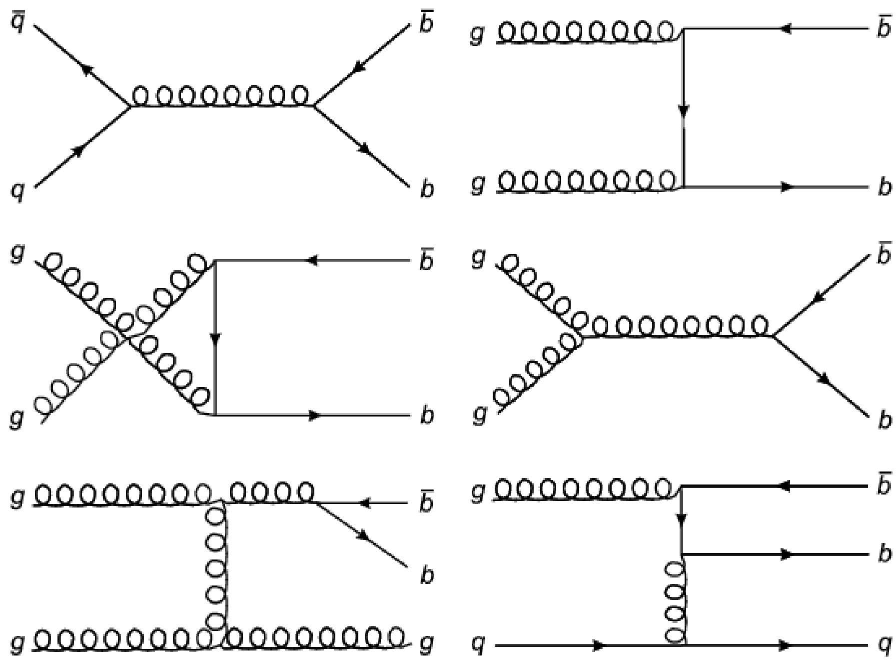

Figure 2: a (top two rows), b (bottom left), and c (bottom right), correspond to flavor creation, gluon splitting, and flavor excitation respectively. From [17].

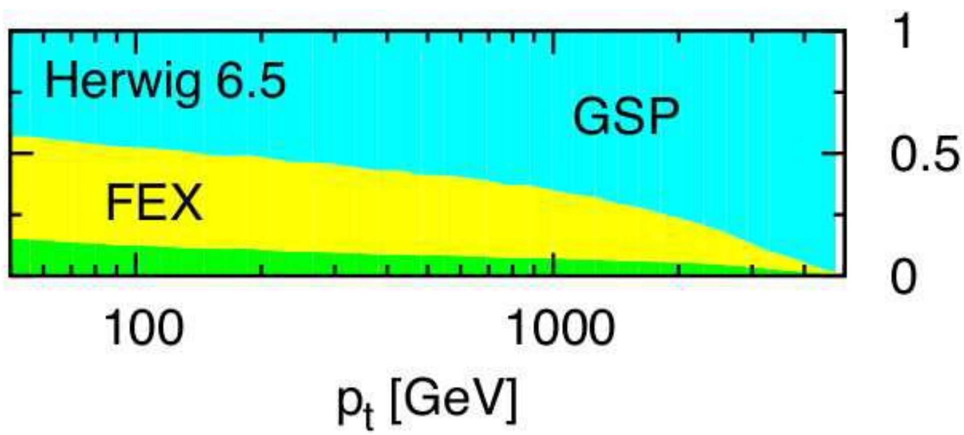

Figure 3: A breakdown of the inclusive b spectrum split into its three major contributions: FCR (green), FEX (yellow), and GSP (cyan). The symbol p_t indicates the transverse momentum of the hardest jet in the event. From [18].

After a quark, such as the b, is produced, it undergoes fragmentation. This consists of two steps, the perturbative fragmentation and the hadronization. During the perturbative fragmentation, the produced bottom and anti-bottom quarks radiate gluons, a process described by QCD and calculable both analytically and with Monte Carlo techniques. It is called the “perturbative” fragmentation because on the scale $Q^2 \gg \Lambda_{QCD}$, the strong coupling α_s is small. During the hadronization step, the quarks separate and the strong coupling between them grows, until the energy in the field is sufficient to create a new quark-antiquark pair from the vacuum. This process is repeated until the energy of the system that is not in the form of mass or binding energy is less than that of the lightest quark-antiquark pair, at which point all quarks have formed color-neutral states. This process is not perturbative and cannot be determined analytically. It is necessary to quantify the mathematical boundaries between the perturbative and non-perturbative regime of the fragmentation. To do this, a parameter called the factorization scale is defined. Soft-gluon resummation has made the fragmentation functions scale-independent[19].

2.5.2 Motivation for Studies of B-Physics and the $B_s \rightarrow 4\mu$ Decay

In pp reactions at the LHC, B-physics is studied to provide precision tests of the Standard Model and to search for new phenomena whose explanation pushes theory beyond the Standard Model (BSM). B-physics is also used to characterize the quark-gluon plasma, to study the quark-mass dependence of fragmentation, and to study other forms of high-energy physics that are difficult to examine with lighter quarks. The b-quark offers a direct way to determine weak mixing angles, test the unitarity of the CKM matrix, understand the mechanism of CP violation, and understand the origin of the universe’s matter-antimatter asymmetry, the magnitude of which is not explained in the SM. Heavy-quark hadronic weak decays also serve as a probe of quark and gluon confinement inside the hadron, one of the least-understood aspects of the strong interaction.

The purpose of the search for the $B_s \rightarrow 4\mu$ decay, which is anticipated to be rare, is to search for physics beyond the Standard Model. The process $B_s \rightarrow \mu^+\mu^-\mu^+\mu^-$ is anticipated to have a very small branching ratio, with theory indicating that it lies between 1.3×10^{-10}[20] and 3.5×10^{-11}[21]. However, this decay could be mediated by previously unobserved BSM species including horizontal gauge bosons[22], supersymmetry via sgoldstinos[23], and/or hidden sector particles[24]. This search is being performed using data collected by the ATLAS Experiment during LHC's Run-2, the LHC's 13 TeV 2015 run. The data are provided by colliding protons on protons at center-of-mass energy 13 TeV. The decay $B_d \rightarrow 4\mu$, which is estimated to have a branching ratio (BR) one-tenth of the B_s[25], will interfere with the $B_s \rightarrow 4\mu$ measurement, and as such methods will need to be explored to separate these two decays. This much smaller BR is also the primary reason why this search uses the B_s, and not the B_d.

The search for this decay has been performed by the LHCb Experiment[25] in 2013, using 1 fb^{-1} of $\sqrt{s} = 7$ TeV data recorded in 2011. LHCb set a limit on the branching ratio of the $B_s \rightarrow 4\mu$ decay such that the SM non-resonant decay mode is restricted to $BR(B_s \rightarrow 4\mu) < 1.6\ (1.2)\times10^{-8}$ at 95% (90%) CL. LHCb's measurement set limits in the context of the supersymmetric model, at the same level as the non-resonant mode. Their measurements were restricted to events which had displacement only in the B-vertex, not considering possible non-zero lifetimes of the supersymmetric particles; this leaves unexplored parameter space for non-zero-lifetime sgoldstinos to exist. In those theoretical predictions where the supersymmetric sgoldstinos have nonzero lifetime, they would produce displaced tertiary vertices in the $B_s \rightarrow 4\mu$ decay. ATLAS can reconstruct particles with long or short lifetimes, making it able to detect these particles, should they exist. To detect these BSM physics, the $B_s \rightarrow 4\mu$ branching ratio will need to be measured and compared to SM expectations; if there is a deviation due to BSM physics, ATLAS should be able to detect and characterize it.

Horizontal gauge bosons are hypothesized[22] particles capable of coupling between generations, for example mediating transitions between down and strange quarks. This theory was motivated by the Family Problem[26] of particle physics, the question of why fermions are observed in three generations, as well as the need to describe CP-violating phenomena. The theory of these particles is an alternative to theories such as supergravity and non-minimal supersymmetric models. The existence of horizontal gauge bosons would necessitate a simple extension beyond the SM gauge group. The major phenomenon this is predicted to give rise to is flavor-changing neutral currents.

Some of the more promising BSM theories involve supersymmetry. $B_s \rightarrow 4\mu$ decays may be mediated by supersymmetric particles called sgoldstinos. These are the hypothetical spin-0 superpartners of the goldstino, the Nambu-Goldstone fermion thought to emerge from the spontaneous breaking of supersymmetry. The goldstino is the fermionic analog of the Nambu-Goldstone boson, and controls the breaking of ordinary bosonic symmetry in supersymmetric models that involve the spontaneous breaking of continuous symmetries. One of the properties of this hypothetical particle is flavor-changing neutral currents, which could cause resonance in the $B_s \rightarrow 4\mu$ decay.

The hidden sector refers to quantum fields and particles that do not interact with SM particles by means of the strong or electroweak forces. This is different from supersymmetric theories, which include particles that do interact via the strong and electroweak processes. These SM gauge group-neutral states do not need to be in the high-GeV range, and in fact can be light while evading flavor and electroweak constraints, because their coupling to SM particles may be very weak. Hidden sector particles may be detected via detection of weak decays occurring at high luminosity, at rates beyond what is determined by the Standard Model. The $B_s \rightarrow 4\mu$ decay may be enhanced by these hidden sector interactions.

The overall goal of this study is to look for enhancement in the $BR(B_s \rightarrow 4\mu)$ beyond the Standard Model's prediction, with specific attention towards enhancement from the aforementioned BSM species. Such an enhancement should be detectable by the ATLAS detector. As this study seeks new physics, this will be a search, not a measurement, and consequently a blind analysis. This means that, during the analysis proper, the signal region of the $B_s \rightarrow 4\mu$ will be obscured, and the study to create selection criteria will be performed on the sidebands. The blind analysis will use 100 fb^{-1} of 13 TeV ATLAS data, and after unblinding, the contribution, if any, from each of the theories can be examined. However, the goal of this dissertation is only to lay the groundwork for this study. Its purpose is to perform a study on the quality of muon transverse momentum triggers to be used in the project, to determine if new topological triggers will be necessary for the project, and to study and reduce the decay's primary backgrounds.

2.6 References

1. Glashow, Sheldon L. (1961). Partial-symmetries of weak interactions. Nucl. Phys. 22, 579-588.

2. Weinberg, Steven (1967). A Model of Leptons. Phys. Rev. Lett. 19, 1264-1266.
3. Higgs, Peter W. (1964). Broken Symmetries and the Masses of Gauge Bosons. Phys. Rev. Lett. 13, 508-509.
4. Gargamelle Neutrino Collaboration (1973). Observation of Neutrino Like Interactions Without Muon Or Electron in the Gargamelle Neutrino Experiment. Phys. Lett. B46, 138-140.
5. Fritzsch, H., Gell-Mann, Murray, Leutwyler, H. (1973). Advantages of the Color Octet Gluon Picture. Phys. Lett. B47, 365-368.
6. ATLAS Collaboration (2012). Observation of a new particle in the search for the Standard Model Higgs boson with the ATLAS detector at the LHC. Phys. Lett. B716, 1-29.
7. CMS Collaboration (2012). Observation of a new boson at a mass of 125 GeV with the CMS experiment at the LHC. Phys. Lett. B716, 30-61.
8. Wikipedia user MissMJ (2006). Standard Model of Elementary Particles. https://en.wikipedia.org/wiki/File:Standard_Model_of_Elementary_Particles.svg.
9. Particle Data Group (2014). Review of Particle Physics. Chin. Phys. C, 38, 090001.
10. SNO Collaboration (2001). Measurement of the rate of $\upsilon_e + d \rightarrow p + p + e^-$ interactions produced by ^{8}B solar neutrinos at the Sudbury Neutrino Observatory. Phys. Rev. Lett. 87, 071301.
11. Rovelli, Carlo (2000). Notes for a brief history of quantum gravity. Proc. 9th Marcel Grossman Meeting, p.742-768. arXiv:gr-qc/0006061.

12. CMS Collaboration (2015). Limits on the Higgs boson lifetime and width from its decay to four charged leptons. Phys. Rev. D92, 7, 072010.

13. Gell-Mann, Murray (1964). A Schematic Model of Baryons and Mesons. Phys. Lett. 8, 214-215.

14. Gell-Mann, Murray, & Ne'eman, Y. (1964). The Eightfold Way. Boulder, Colorado: Westview Press.

15. Kobayashi, Makoto, & Maskawa, Toshihide (1973). CP Violation in the Renormalizable Theory of Weak Interaction. Prog. Theor. Phys. 49, 652-657.

16. Herb, S. W., *et al.* (1977). Observation of a Dimuon Resonance at 9.5-GeV in 400-GeV Proton-Nucleus Collisions. Phys. Rev. Lett. 39, 252-255.

17. Fornal, Bartosz, and Trott, Michael (2010). High p_T Production of $b\bar{b}$ at LHC and New SU(3) Bosons. JHEP 1006, 110.

18. Zanderighi, Giulia (2007). Accurate predictions for heavy quark jets. CERN-PH-TH-2007-081.

19. Bonciani, Roberto, Catani, Stefano, Mangano, Michelangelo, and Nason, Paolo (1998). NLL resummation of the heavy quark hadroproduction cross-section. Nucl. Phys. B529, 424-450.

20. Melikhov, Dmitri, and Nikitin, Nikolai (2004). Rare radiative leptonic decays $B_{d,s} \to l^+l^-\gamma$. PRD 70, 114028.

21. Dincer, Yusuf, and Sehgal, L. M. (2003). Electroweak effects in the double Dalitz decay $B_s \to l^+l^-l^+l^-$. Physics Letters B 556, 169–176.

22. Wilczek, F., & Zee, A. (1979). Horizontal Interaction and Weak Mixing Angles. Phys. Rev. Lett. 42, 421.

23. Gorbunov, D. S., & Rubakov, V. A. (2005). On sgoldstino interpretation of HyperCP events. Phys. Rev. D73, 035002.

24. Batell, Brian, Pospelov, Maxim, & Ritz, Adam (2011). Multi-lepton Signatures of a Hidden Sector in Rare B Decays. Phys. Rev. D83, 054005.

25. Aaij, R. (LHCb Collaboration) (2013). Search for rare $B^0_{(s)} \to \mu^+\mu^-\mu^+\mu^-$ Decays. Phys. Rev. Lett. 110, 211801.

26. Hwang, W-Y. Pauchy (2008). The Family Problem. arXiv:0808.2091.

Chapter 3: The ATLAS Detector and the Large Hadron Collider

3.1 Introduction

Both the study of the $B_s \rightarrow \mu^+\mu^-\mu^+\mu^-$ decay and the project to optimize the B-physics trigger make use of data from the ATLAS experiment at the LHC. Overviews of both are presented here.

3.2 The Large Hadron Collider

The Large Hadron Collider[1] (LHC) at the European Organization for Nuclear Research (CERN) in Switzerland is the world's largest and most complex experimental facility ever built, the largest single machine ever built, and the world's most powerful particle collider. The LHC was built between 1998 and 2008 by a collaboration of over 10,000 scientists and engineers from over 100 countries and hundreds of universities and laboratories, including the University of New Mexico. It is a two-ring superconducting proton-proton accelerator 27 kilometers in circumference and placed up to 175 meters deep. Its initial run, spanning the years 2010-2013, provided collisions with a center-of-mass energy of 7 TeV, upgraded later to 8 TeV; the current run, 2015-present, reaches 13 TeV, with plans[2] to upgrade it further to 14 TeV. The next upgrade in the 2020s, called the High Luminosity LHC[3], will not increase the center-of-mass energy, but will instead increase the instantaneous luminosity by a factor of 10. Two proton beams are accelerated in opposite directions in separate vacuum pipes, and are brought into collision at four different intersection sites where the various detectors are located. While its primary mode of operation is proton-proton collision, the LHC is also able to collide protons with lead nuclei, and lead with lead. The former was performed for short periods in 2013 and 2016, while the latter was performed in 2010, 2011, 2013, and 2015.

The protons are produced by stripping the electrons from hydrogen atoms with a strong electric field. They are then accelerated with the linear accelerator Linac2 to 50 MeV. They are next injected into the Proton Synchrotron Booster, where they are accelerated to 1.4 GeV. Next, they are sent to the Proton Synchrotron, where the energy of the protons is increased to 450 GeV, and are finally sent to the LHC's primary accelerators. It takes about 20 minutes to fully accelerate the protons. The primary accelerator ring includes 1,232 dipole magnets, to keep the beams in a circular path, and 392 quadrupole magnets to keep the beam focused. Eight superconducting radio-frequency cavities, each of which delivers 2 MeV at 400 MHz, are used to accelerate and bunch the protons. Each bunch has ~115 billion protons, and the bunch collision rate is 40 MHz.

The LHC has attached to it (at the four interaction sites, see Figure 1) four major experiments:

- ALICE[4] (A Large Ion Collider Experiment) is a detector designed to study lead-lead collisions with a center-of-mass energy of 2.76 TeV; the resulting energy density and temperature produce quark-gluon plasma, allowing ALICE to probe QCD in extreme environments.
- ATLAS[5] (A Toroidal LHC ApparatuS) is one of two large, general-purpose detectors at the LHC, optimized for high transverse momentum events, and able to detect the majority of the products of a collision.

- CMS[6] (Compact Muon Solenoid) is the other large, general-purpose detector with goals nearly identical to those of ATLAS; they are designed to complement each other, to both extend reach and to corroborate findings.
- LHCb[7] (Large Hadron Collider beauty) is a single-arm forward spectrometer with a focus on rare B-decays and CP violation in B-decays.

The LHC has three other, smaller, more highly specialized experiments: TOTEM (TOTal Elastic and diffractive cross section Measurement), MoEDAL (Monopole and Exotics Detector At the LHC), and LHCf (Large Hadron Collider forward). This dissertation uses data from the ATLAS detector.

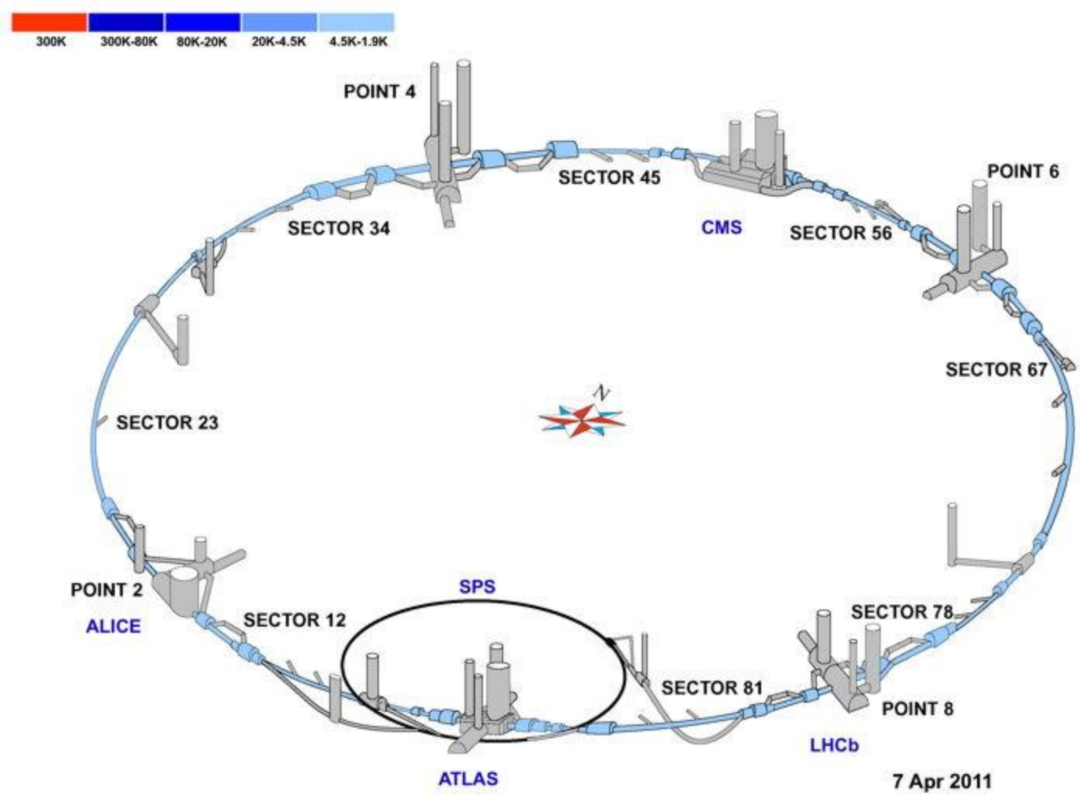

Figure 1: A diagram of the LHC, showing the four main detectors. From [8].

3.3 The ATLAS Experiment

ATLAS is a general-purpose detector 46 meters long and 25 meters in diameter, with a mass of ~7000 tons. The various detector layers of ATLAS cover the majority of the solid angle around the interaction point, out to an absolute pseudorapidity of 2.5, and are designed to characterize known particles and interactions, and to identify missing energy indicative of neutrino generation or Beyond the Standard Model physics. One of its most important goals is to investigate and characterize the Higgs boson. Its other goals include investigating CP violation in matter/antimatter asymmetry and investigating the properties of the top quark and other particles.

The ATLAS detector has four components: The Inner Detector, the Calorimeter, the Muon Spectrometer, and the Magnet System. Data are collected from the Trigger and Data Acquisition System (TDAQ), and events are later reconstructed by the Computing System. See Figure 2 for a diagram of the physical components.

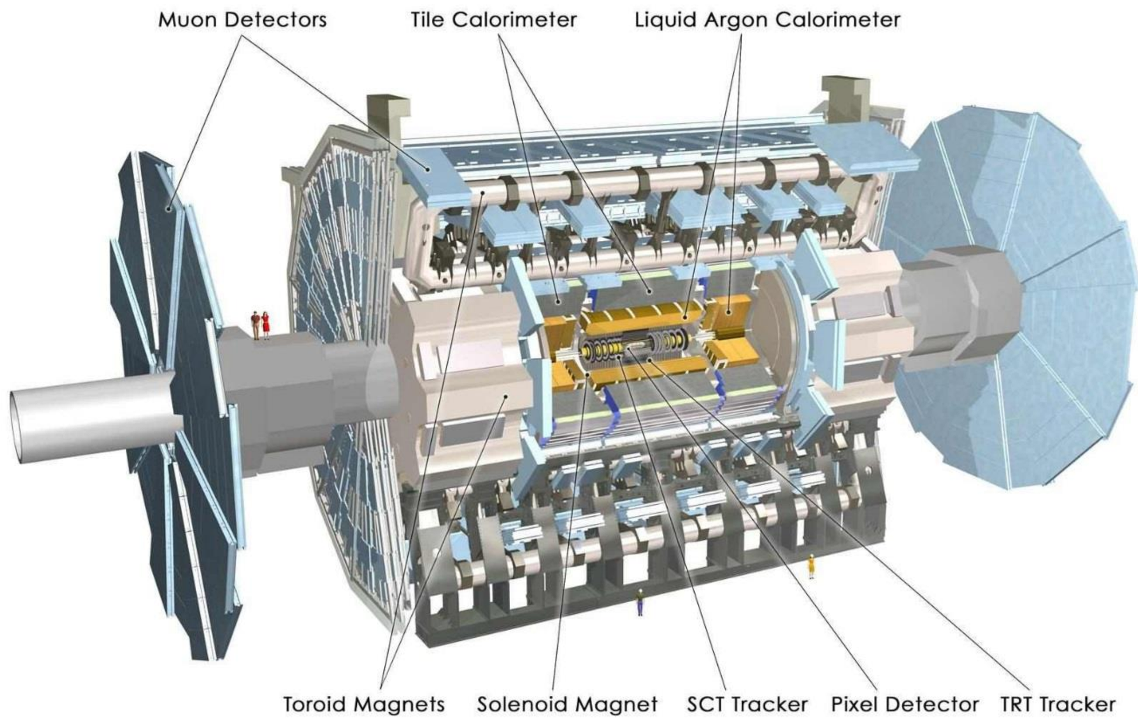

Figure 2: A diagram of the Run-1 ATLAS detector, with all the major components labeled. Note that this does not include the innermost pixel layer (the Insertable B-Layer[9]), which was added for the Run-2 data-taking period. From [10].

3.3.1 The Inner Detector

The Inner Detector (ID, Figure 3) is the innermost part of the ATLAS detector, covering the radial range from 33 millimeters from the interaction point to a radius of 1.2 meters, with a length of 6.2 meters along the pipe. It tracks charged particles by their interaction with material at discrete points and is comprised of the Silicon Pixel Detector (Pixel), the SemiConductor Tracker (SCT), and the Transition Radiation Tracker (TRT). The solenoidal magnetic field in which the ID is located causes charged particles to travel on curved trajectories. Measurements of these trajectories reveal the particles' momentum and charge. The principles by which the particles are detected involve a different process for each subsystem. For example, high-energy particles traversing a silicon sensor deposit some of their energy in the sensor's bulk, creating electron-hole

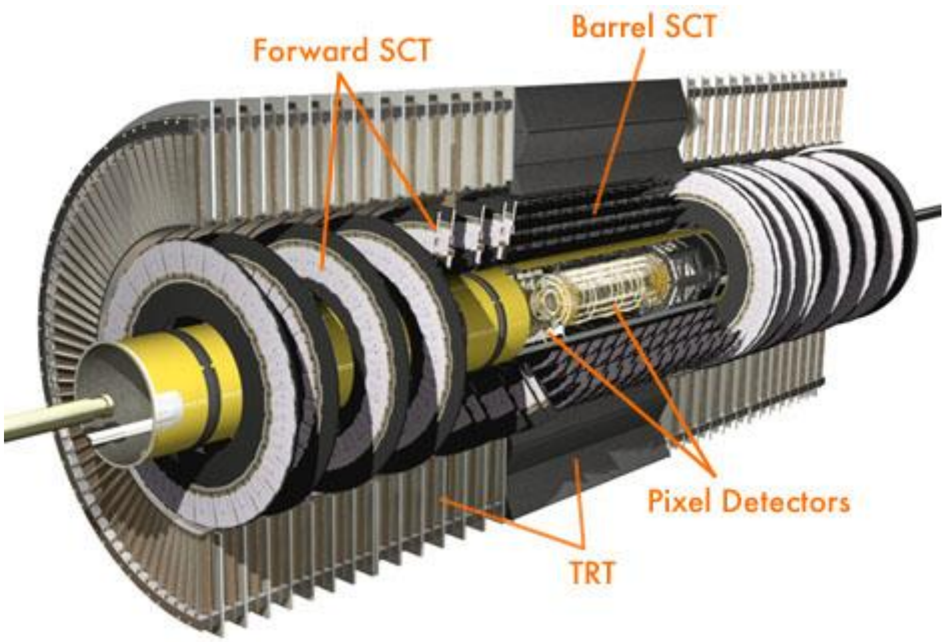

Figure 3: A diagram of the Inner Detector, with the Pixel Detector, Semiconductor Tracker, and Transition Radiation Tracker labeled. From [11].

pairs. The charge released is measured by the detector electronics, and the track is reconstructed based on a pattern of hit points left by a charged particle crossing the fiducial volume. As an example, if a set of particle tracks reconstruct to a vertex other than the proton-proton collision, it may imply that the particles are the product of the decay of a particle itself produced in the primary collision.

The Inner Detector can measure events in the pseudorapidity range $|\eta| \leq 2.9$, and over the whole range of the azimuthal angle φ. Within the central η region, $0 \leq |\eta| \leq 1.05$, the "barrel" of ATLAS, the Inner Detector is designed to have a transverse momentum resolution of $\sigma_{p_T}/p_T = 0.05\%\ p_T\ \text{GeV} \oplus 1\%$ in the plane perpendicular to the beam axis, and a transverse impact parameter resolution of 10 micrometers for high momentum particles. For single track muons, the reconstruction efficiency is ~99.5%[12], with pion efficiency 5-10% lower due to interactions with the detector material. Electron efficiencies are lower than for muons due to Bremsstrahlung energy losses. Jets, narrow cones of hadrons and other particles produced by the hadronization of quarks and gluons, have an efficiency of ~92% in the barrel, and ~85% in the endcaps, although this efficiency can depend on the jet's kinematic properties.

The Pixel Detector is the innermost subsystem of ATLAS; it has three concentric layers and three disks on the endcaps (the parts at the ends of the cylindrical detector). The Pixel Detector is 1.4 meters long and extends from the beam pipe, at 50.5 mm, out to 150 mm. It has a total of 1,744 modules, each 2x6 cm^2, comprised of 250 μm-thick silicon. The smallest structures in the Pixel Detector are the pixels themselves, 50x400 μm^2 structures of which there are 46,080 per module, giving the Pixel Detector over 80 million readout channels. It covers a pseudorapidity range of $|\eta| \leq 2.5$. This represents about 50% of all channels in the ATLAS detector. For perpendicular incidences, the fractional radiation length of this detector is approximately 0.107[13] of integrated radiation length X_0, defined as the distance over which an electron on average loses all but 1/e of its energy to Bremsstrahlung radiation.

The IBL[9] is located inside the Pixel Detector, starting 33 mm from the pipe, out to 50.5 mm. It is a single layer comprised of 26,880 50x250 μm^2 pixels, arranged in 80 columns and 336 rows, covering a range $|\eta| \leq 2.9$. IBL pixels use planar silicon sensors, covering 75% of the active sensing area, and 3D sensors covering the outer 25% sensing area. For the IBL, the fractional radiation length is only 0.019 of X_0.

The Semiconductor Tracker is the middle portion of the ID. It uses planar silicon sensors similar to those of the Pixel Detector, save that the sensors are long, narrow strips, in order to more effectively cover a larger area and reduce the amount of data to be read out. It has four double layers of 12 cm x 80 μm silicon strips in the barrel and 9 in each endcap, comprising 4088 two-sided modules and six million readout channels. The SCT's active silicon covers a much larger area than the Pixel Detector (60 m^2 vs. the Pixel's 1.7 m^2), and covers the radial range from 299 mm to 560 mm. As with the Pixel Detector, it covers a pseudorapidity range of $|\eta| \leq 2.5$. For the SCT, the fractional radiation length is approximately 0.118[12] of X_0.

The Transition Radiation Tracker is the outermost portion of the ID, with a volume of 12 m^3, and a radial range of 563 mm to 1066 mm. It uses a combination of a straw tracker and a transition radiation detector. The straw tracker is made of 212,188 straw tubes, a type of gaseous ionization detector comprised of a 4 mm-diameter and up to 144 mm long Kapton tube with a wire along the axis. When a particle passes through it, the 70:27:3 gas mixture of Xenon:CO_2:O_2 becomes ionized, and the potential difference maintained between the wire and the wall of the tube causes the free electrons and ions to move to the wire and wall. The current produced from this separation indicates that a particle has passed through the chamber. The transition radiation detector contains multiple layers of materials with different indices of refraction, such that the probability of transition radiation increases with the relativistic gamma factor at each interface. This system is not as precise as the other two components of the Inner Detector, but covers the largest area at the least cost. The TRT has about 300,000 straws total, 50,000 in the barrel and 250,000 in the endcaps. In the barrel region, these straws are arranged in three concentric cylindrical layers, while in the endcaps radially-oriented straws are arranged in eighty wheel-like layers. The TRT's layout is designed such that a charged particle with $p_T > 0.5$ GeV and $|\eta| \leq 2.0$ will cross more than 30 straws. The

TRT also provides electron identification by way of transition radiation from interleaved polypropylene fibers in the barrel and foils in the endcap. As before, it covers a pseudorapidity range of $|\eta| \leq 2.5$. For the TRT, the fractional radiation length is approximately 0.20[12] of X_0.

3.3.2 The Calorimeters

Immediately outside the ID is a solenoid magnet, providing a 2 Tesla magnetic field; outside of that are the calorimeters. The magnet has a fractional radiation length of 0.66 X_0[12] and an interaction length of 0.172 λ_I, where λ_I is the mean free path of the hadron, the average distance traveled by a particle between collisions with other particles. This section has two different calorimeters: The ElectroMagnetic Calorimeter (EMC, Figure 4), and the Hadronic Calorimeter (HC).

The EMC is the inner calorimeter, and uses lead as an absorber and liquid argon cooled to 90 K as a sampling material. It covers an η range of $0 \leq |\eta| \leq 3.2$, with $0 \leq |\eta| \leq 1.05$ being the barrel section and $|\eta| \geq 1.05$ constituting the endcaps. The EMC's "accordion" geometry allowing complete φ-coverage without azimuthal cracks. It is 6.4 meters long and 53 centimeters thick, and it has 110,000 channels. It detects particles that interact primarily electromagnetically, specifically electrons and photons. When the particles pass through the energy-absorbing lead and stainless steel casing and into the argon, showers are generated that liberate electrons and partons, which are then recorded. It has a perpendicular fractional radiation length of 24 X_0[12], and a perpendicular interaction length of ~1.5 λ_I. The EMC has an energy resolution $\Delta E/E = 11.5\%/\sqrt{E} \oplus 0.5\%$ and a resolution of the polar direction of a particle shower of $\Delta\theta = 50\ \mathrm{mrad}/\sqrt{E}$.

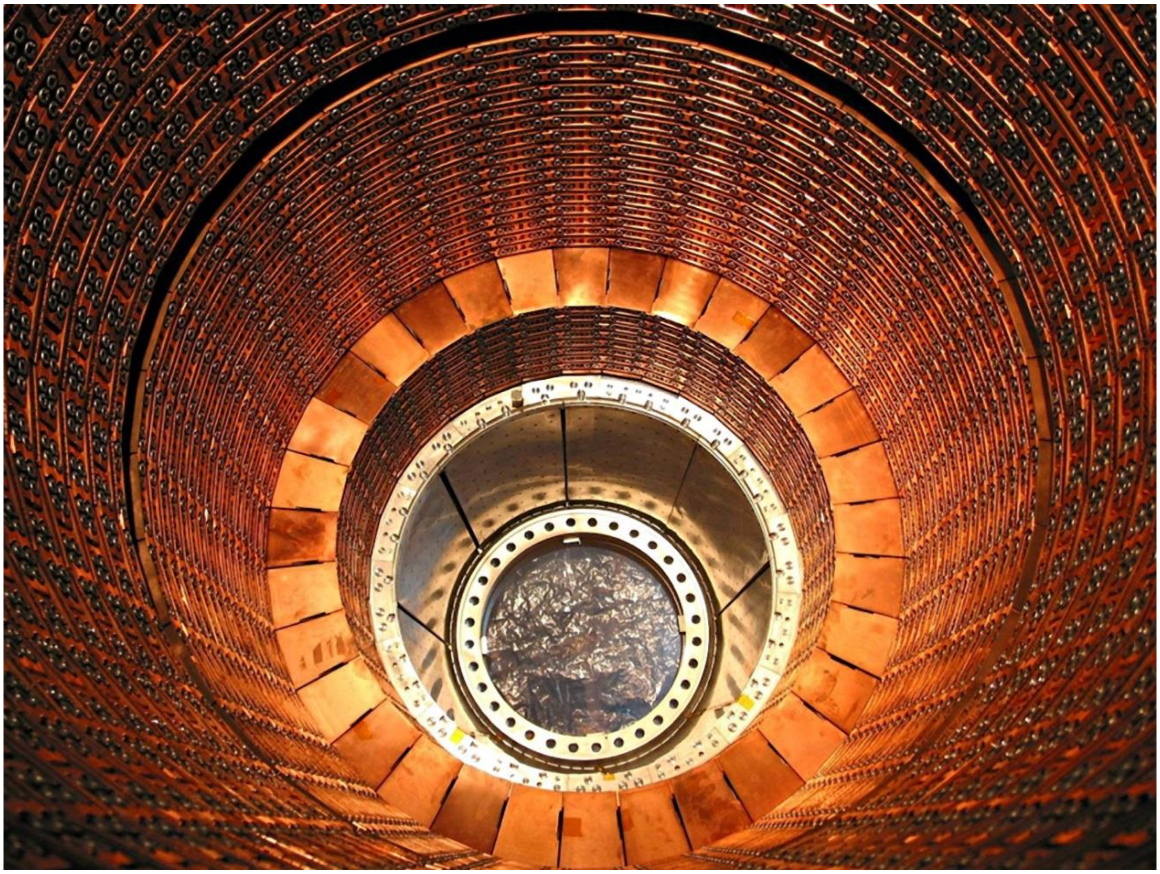

Figure 4: A view inside ATLAS's Electromagnetic Calorimeter. From [14].

The HC is the outer calorimeter, and it is made of steel and tiles of scintillating plastic; for this reason, it is sometimes called the Tile Calorimeter. The barrel section of the HC covers the pseudorapidity region $|\eta| \leq 1.7$, while the end cap region covers the range $1.5 \leq |\eta| \leq 3.2$. It is composed of 500,000 tiles, with 64 5.6-meter long wedges in the barrel and 64 2.6-meter long wedges in each endcap. These are small gaps of a couple of millimeters between different sections of the tile calorimeter; these are filled with steel-scintillator sandwiches and thin scintillation counters, in order to partially recover energy lost in the crack region of the detector. The HC is designed to interact with particles that pass through the EMC without interacting, but that do interact through the strong force, primarily hadrons and hadronic decay products of tau leptons. Showers are created in these tiles as these particles pass through, causing them to emit light which is transmitted by optical fibers to photomultiplier tubes, where it is detected and recorded. The HC extends over 7.4 interaction lengths, and it has an average jet energy resolution of $\Delta E/E = 50\%/\sqrt{E} \oplus 3\%$, and a segmentation of $\Delta\eta\times\Delta\varphi = 0.1\times0.1$.

3.3.3 The Muon Spectrometer

The Muon Spectrometer (MS, Figure 5) is the largest subsystem of the ATLAS Experiment, with a diameter of 22 meters, a length of 44 meters, and a total surface area of about 12,000 m^2 throughout its layers of detectors[15]. This size is necessary to accurately measure the momentum of muons, which have sufficiently high energy and low interaction rate that they can pass through all the other ATLAS subsystems. The MS is designed to measure the momentum of charged particles in the pseudorapidity range $|\eta| \leq 2.7$, and to trigger on said particles in the range $|\eta| \leq 2.4$. In the barrel region, the magnetic field in the MS varies between 0.15 T and 2.5 T, depending on radial position and azimuthal angle, with an average of 0.5 T. The Muon Spectrometer has a stand-alone transverse momentum resolution of approximately 10% for 1 TeV tracks, which translates into a sagitta along the z (beam) axis of about 500 μm, to be measured with a resolution of ≤ 50 micrometers.

The MS has three parts: a magnetic field, created by eight superconducting toroidal magnets, with a field varying between 0.5 and 2 Tesla; a set of 1200 chambers designed to measure the tracks of outgoing muons with high precision; and a set of triggering chambers with precise time-resolution. Four different types of detectors are used: Monitored Drift Tubes (MDT), Cathode Strip Chambers (CSC), Resistive Plate

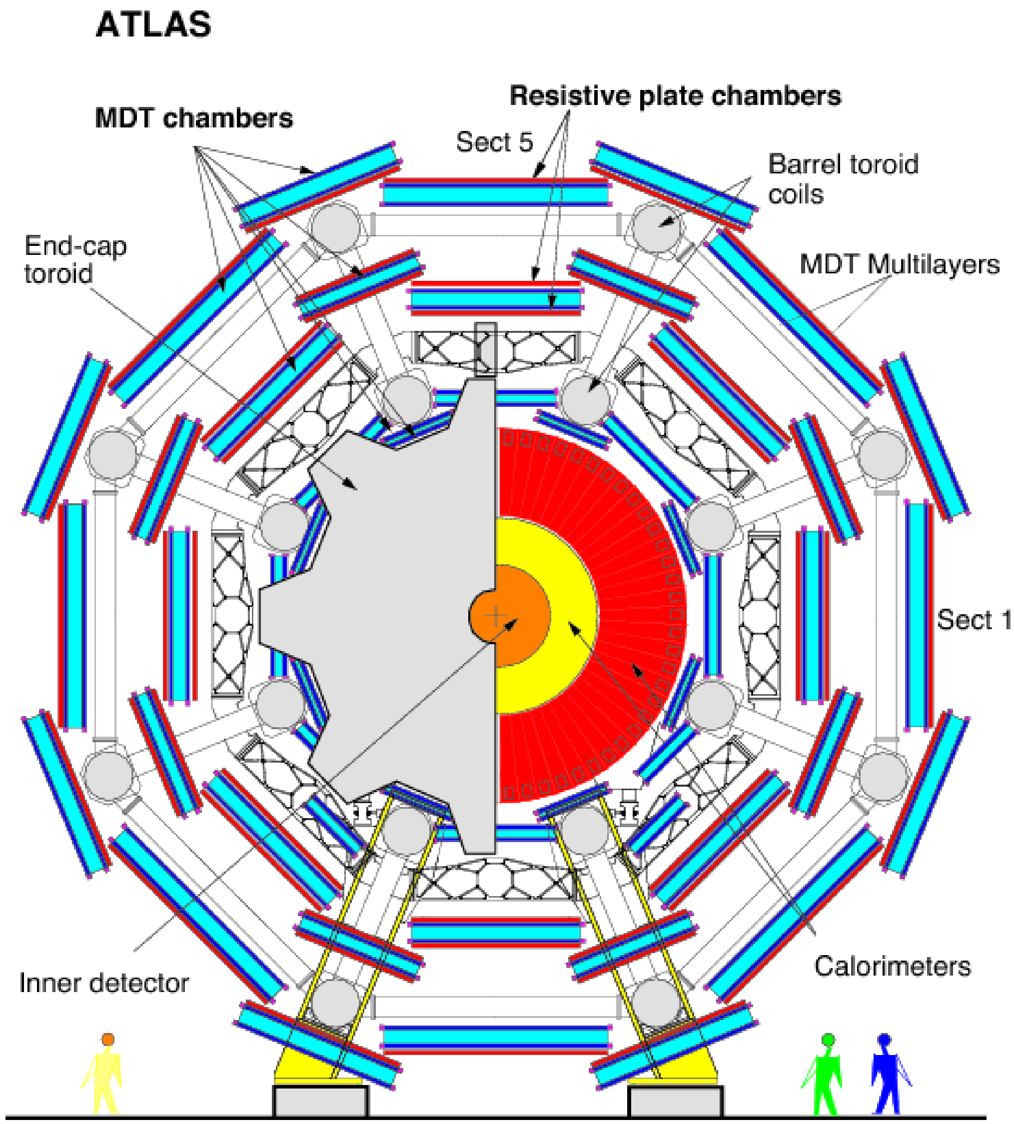

Figure 5: A diagram of the various sections of the Muon Spectrometer. From [16].

Chambers (RPC), and Thin Gap Chambers (TGC). The RPC and TGC act as triggering chambers, while the MDT and CSC are for precision measurements.

The MDTs are 30 mm-diameter, 400 μm-thick aluminum tubes filled with a 93%:7% mixture of $Ar:CO_2$. Along the axis of the tube is a wire, and as with the straw chambers, a potential is maintained between the wire and the tube. The MDTs are arranged in two sets of three or four layers, each separated by a mechanical spacer. When a charged particle traverses the tube, it liberates electrons; the free electrons are drawn towards the wire, and positive ions towards the wall of the tube. The resulting current presents a signal to the readout electronics attached to the tube.

The CSCs are multiwire chambers that are used instead of the MDTs in high-occupancy regions because they have smaller electron drift times. CSCs are constructed of cathode planes, segmented into strips, with anode wires running orthogonal to the cathodes. The assembly is filled with an 80%:20% argon and carbon dioxide gas mixture. When a particle passes through, it creates free electron/ion pairs in the gas which induce a current into the detector electronics.

The RPCs are another type of gaseous detector, made of two parallel resistive electrode plates of phenolic-melaminic plastic laminate. These are separated from each other by 2 millimeter mechanical spacers. The signal is read out from the metallic strips mounted to the outer faces of the resistive plates.

The TGCs are multi-wire chambers consisting of two cathode plates, separated by 2.8 millimeters, with anode wires passing through the middle. The TGCs are filled with a mixture of carbon dioxide and n-pentane. These are primarily endcap detectors, the high electric field and short distance between anode wires (1.8 mm) giving a very good time resolution for most tracks.

The Muon Spectrometer's primary background is composed of neutrons and gamma photons with energies typically below 1 MeV and 100 keV, respectively[15]. The fluence values for these backgrounds are estimated to be of order 1 kHz/cm^2 throughout most of the detector. For the MS to register a muon as a hit, it requires a minimum p_T of 3-4 GeV, depending on its pseudorapidity[17]. ATLAS uses three different algorithms to identify muons[18]: combined reconstruction, standalone reconstruction, and tagging. Reconstruction of combined muons is performed by taking data from both the ID and MS and finding tracks that point approximately to the interaction point. Reconstruction of standalone muons is performed similarly, although in that case data are taken only from the MS. Tagging allows reconstruction of additional muon candidates by tagging ID tracks with MS or calorimeter data and extrapolating them back to the MS. The efficiency of the MS to reconstruct muons as combined muons (with the inner tracker) with $p_T > 20$ GeV is ~95%, while muon trigger efficiency, when the muon has been reconstructed, is ~80%[19].

3.3.4 The Magnet System

The ATLAS detector has three superconducting magnet systems: the central solenoid, the barrel toroid, and the endcap toroid. See Figure 6.

The central solenoid produces a 2T field and is located between the Inner Detector and the calorimeters. This causes the charged particles produced in LHC collisions to curve sufficiently that their momentum can be measured. A solenoid magnet

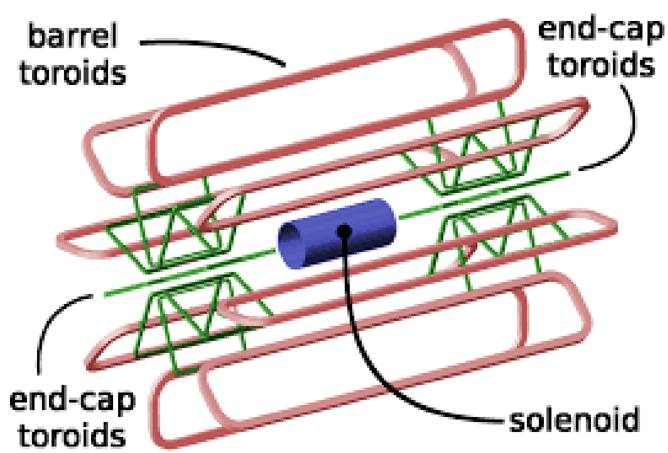

Figure 6: A diagram of the Magnet System. The Inner Detector is inside of the central solenoid, while the barrel toroids are interspersed with the Muon Spectrometer. From [20].

is used due to the uniformity of its interior magnetic field, which permits very precise measurements. Particles with momenta less than 400 MeV will be curved so strongly that they loop within the Inner Detector.

The barrel and endcap toroidal magnetic field is produced by eight large air-core superconducting coils around the barrel, and another eight smaller coils at the endcaps. These magnets are outside of the calorimeters, within the structure of the Muon Spectrometer. The barrel magnet provides a field spatially varying between 0.5 and 2 Tesla, while the endcap field is between 1 and 2 Tesla.

3.3.5 The Trigger and Data Acquisition System

During Run-1, the name of the data and software from the LHC's 8 TeV 2012 run, ATLAS generated about 25 Mb of data per event, or about a petabyte per second. In order to cope with the enormous data rate given computing and storage limitations, while still retaining the ability to study various physics processes, ATLAS uses a sophisticated, three-stage trigger system to preserve interesting events while reducing the amount of data stored.

There are three components of the ATLAS Trigger and Data Acquisition System: The Level-1 Trigger (L1), the Level-2 Trigger (L2), and the Event Filter (EF). These last two are collectively called the High-Level Trigger (HLT). The architecture of this system can be seen in Figure 7.

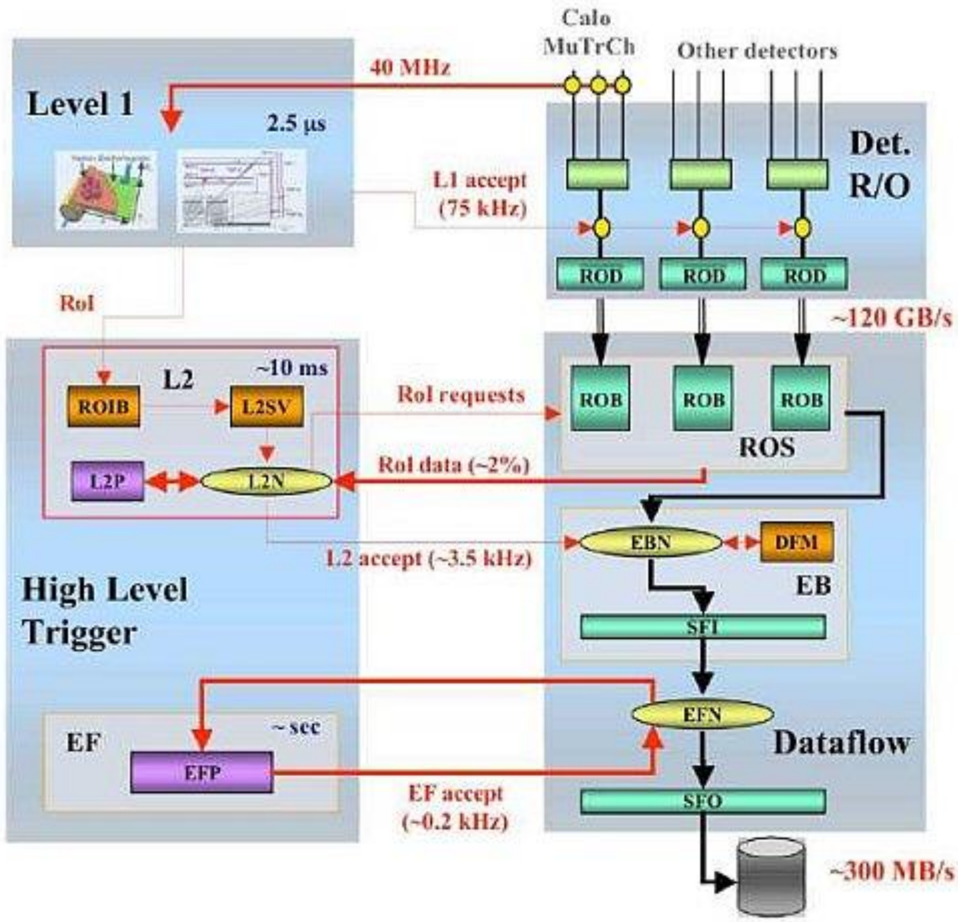

Figure 7: A visualization of ATLAS trigger and data acquisition software. From [21].

3.3.5.1 The Level-1 Trigger

The Level-1 trigger is a hardware-based, synchronous, pipelined system consisting of a Central Trigger Processor (CTP) which is fed by signals from the dedicated trigger hardware in the calorimeter and muon detectors. In the calorimeters, this signal takes the form of energy deposits, while in the muon detectors a coincidence of hits across multiple layers of the detector is sought. The output of this system is a single-bit Level-1 Accept signal, which communicates to the detector front-end readout systems, via the Trigger Timing and Control System, whether or not to read out the event information held in the pipelines of the front-end electronics. The readout of the accepted events is then passed to the High-Level Trigger. In order to avoid pipe overflow, the Level-1 trigger target latency is set at two microseconds, with a contingency of five hundred nanoseconds. Much of that time is spent transmitting signals between the on-detector electronics and electronics in the neighboring cavern, and as a consequence only about five hundred nanoseconds are available for processing the input signals and reaching a trigger decision.

The rate at which the Level-1 trigger selects events – the physical event rate, the rate at which beam bunches are delivered to LHC experiments – is 40 MHz; the Level-1 reduces this rate to less than 75 kHz, although future upgrades may increase this to 100 kHz. Most of the Level-1 trigger bandwidth is intended to be used for collision events, for which there are typically 1000-1500 filled bunch crossings per full orbit of the LHC beam in Run-1 data. Requiring that the bunch crossing is filled can reduce the rate by 50-75%, however the remaining rate reductions are accomplished by the trigger system identifying events of interest, by performing a fast analysis of the detector signals generated by the colliding bunches. The Level-1 trigger is loaded with a trigger menu, a list of up to 256 criteria for each data-taking period. These trigger items include configurable algorithms to trigger on electrons or photons, hadronically decaying tau leptons, muons, jets, and missing transverse energy. For higher luminosities, the algorithm's trigger rates increase with at least a linear dependence on the luminosity.

The calorimeter trigger, called L1Calo, is based on dedicated analog trigger signals provided by the calorimeters independently from that used by the offline reconstruction software. While the calorimeters measure energy deposited in small cells of various sizes, the smallest having a $\Delta\eta \times \Delta\varphi = 0.025 \times 0.025$, L1Calo instead uses information from analog sums in regions of granularity $\Delta\eta\times\Delta\varphi = 0.1\times0.1$ (central region) to $\Delta\eta\times\Delta\varphi = 0.4\times0.4$ (forward region). L1Calo takes data from both the EMC and the HC, digitizing the data before sending it to the Level-2 trigger. The muon trigger, L1Muon, searches instead for a coincidence of hits across multiple layers of trigger chambers, consistent with the combination of hits expected from muons originating from an interaction point at the origin. It uses two types of trigger chamber, Resistive-Plate Chambers in the barrel region and Thin-Gap Chambers in the endcaps. L1Muon triggers on muons above various threshold p_T's; when such a muon is detected, the data are saved and sent to the Level-2 trigger.

3.3.5.2 The Level-2 Trigger

As part of its function, the Level-1 trigger defines regions in the detector where the signal exceeds programmable thresholds. These regions are defined as "Regions of Interest" (RoIs), and are used as seeds for the Level-2 trigger. By focusing on these regions, it is possible to reduce the amount of data transferred into the Level-2 processors to less than two percent of the total event data while retaining efficient classification algorithms. The Level-2 trigger's selection algorithm typically requests data from one or two Regions of Interest. The Level-2 trigger reduces the data rate from ~75 kHz to ~2 kHz.

Selection in the Level-2 trigger is performed on Regions of Interest defined by the Level-1 trigger. RoI data from the Level-1 trigger are sent to the readout systems, while at the same time information on the location of RoIs identified by the Level-1 trigger is sent to the Level-2 system. Using the Level-1 result – the Region of Interest – as a guideline, specialized Level-2 algorithms request a subset of the event data from the readout systems in order to perform a selection. The algorithms then determine if the event generated by the collider contains characteristics classifying it as an event of interest through energy sums, particle shower containment, track-finding and track-fitting algorithms, etc. By selectively accessing, reformatting, and analyzing the detector data in only these regions, the processing time needed by the Level-2 trigger can be greatly reduced, and more data of interest can be recovered. The selection algorithms confirm and refine the Level-1 result using more finely-grained detector data and improved calibration constants. These algorithms are designed for timing performance, as at this point in the trigger system one of the major priorities is to reduce the amount of data-per-second to a more manageable level. For those events selected by the Level-2 trigger, details are sent to a pseudo-readout system (pROS) to be included in the event. The Level-2 trigger then forwards these data to the event builder, and from there on to the Event Filter. Events are not actually reconstructed in the Level-2 trigger, however; this occurs in the event builder, and is later refined in the Event Filter.

3.3.5.3 The Event Filter

The Event Filter is the last level of event selection before events are sent to mass storage. Unlike the Level-1 and -2 triggers, which use specialized algorithms with latencies of two microseconds and ten milliseconds respectively, the Event Filter uses offline physics object and event reconstruction with full event data and has a latency of a few seconds.

Unlike the lower-level triggers, the Event Filter has access to the complete event data and uses reconstruction and physics as directly as possible from the offline (as opposed to specialized algorithms). By minimizing the size of the accepted events, and by using some data compression techniques – such as the DEFLATE algorithm[22] and the zlib library[23] – it reduces the amount of data sent to mass storage by rejecting events which do not conform to the physics requirements.

Its access to complete event data puts the Event Filter in a position to perform global monitoring, calibration, and alignment functions online, which is not possible at the detector readout level. This is a vital element in the overall quality control of the experiment both for the physics quality and the detector optimization and performance. The quality of the detector calibration has a direct bearing on the quality of the Event Filter decision itself.

After the event passes through the Level-2 Trigger, all data are collected and passed to the Event Filter farm. This level analyzes the entirety of each event in order to reduce the rate to ~200 Hz and latency to ~1 second. Accepted events are then sent to the mass data storage facility at CERN. After LHC data pass through all the triggers, the data rate is reduced to 100 Mb/s, from an original 1 Pb/s.

3.3.6 The Computing System

The reconstruction and analysis of the signals saved by the Event Filter is implemented with Athena[24], ATLAS's native software framework. Reconstruction begins with the raw byte-stream data, outputted from the EF. Reconstruction algorithms manipulate these data into Event Summary Data (ESD), where physics objects like tracks and particles are built. Then Analysis Object Data (AOD) are created from the ESD, and these include all the information needed for most analyses. Additional analysis-specific decisions can be applied at this level, reducing the size of the file in the process. Finally, for most analyses, the AOD are transformed into an ntuple, which can be more easily read and analyzed than AOD.

A global collaboration of hundreds of computing centers in more than forty countries, along with the necessary communication infrastructure, composes the Worldwide LHC Computing Grid (WLCG, or "Grid"). The Grid has three Tiers which describe its structure: the Tier-0 computing center is the heart of the Grid located at CERN and keeps a copy of all data stored by the detector. After reconstruction, ESD and AOD are sent to national Tier-1 and regional Tier-2 centers, respectively, for storage and distribution. Finally, there is a Tier-3 in the form of personal work computers, where collaborators download data from other tiers for their own analyses.

3.4 References

1. Brüning, Oliver Sim, Collier, Paul, Lebrun, P, Myers, Stephen, Ostojic, Ranko, Poole, John, Proudlock, Paul (2004). LHC Design Report, Volumes 1, 2, and 3. CERN-2004-003-V-1, CERN-2004-003-V-2, CERN-2004-003-V-3.
2. Zhu, Hongbo, & ATLAS Collaboration (2013). ATLAS Upgrades Towards the High Luminosity LHC. Stockholm, Sweden: Proc. 2013 European Physical Society Conference on High Energy Physics, C13-07-18.
3. Alonso, Bejar, and Rossi, L. (2015). HiLumi LHC Technical Design Report. CERN-ACC-2015-0140.
4. ALICE Collaboration (2008). The ALICE experiment at the CERN LHC. JINST 3, S08002.
5. ATLAS Collaboration (2008). The ATLAS Experiment at the CERN Large Hadron Collider. JINST 3, S08003.

6. CMS Collaboration (2008). The CMS experiment at the CERN LHC. JINST 3, S08004.
7. LHCb Collaboration (2008). The LHCb Detector at the LHC. JINST 3, S08005.
8. http://blogs.discovermagazine.com/badastronomy/2008/07/22/how-cool-is-the-lhc/
9. ATLAS Collaboration (2012). Overview of the ATLAS Insertable B-Layer (IBL) Project. PoS RD13, 012.
10. Pequenao, Joao (2008). Computer generated image of the whole ATLAS detector. https://cds.cern.ch/record/1095924.
11. Pequenao, Joao (2008). Computer generated image of the ATLAS inner detector. http://cds.cern.ch/images/CERN-GE-0803014-01.
12. Benekos, N., et al. (2004). ATLAS Inner Detector Performance. ATL-INDET-2004-002.
13. Aad, G., & ATLAS Collaboration (2008). The ATLAS Experiment at the CERN Large Hadron Collider. JINST 3, S08003.
14. Langstaff, Roy (2003). Selection of images showing the assembly and installation of the ATLAS Hadronic endcap Liquid Argon Calorimeter, between 2002 and 2004 by Roy Langstaff. http://cds.cern.ch/images/CERN-GE-0312173-14.
15. Palestini, Sandro (2002). The Muon Spectrometer of the ATLAS Experiment. Nuclear Physics B (Proc. Suppl.) 125, 337-345.
16. ATLAS Collaboration (2010). Commissioning of the ATLAS Muon Spectrometer with Cosmic Rays. Eur. Phys. J. C70, 875-916.

17. ATLAS Collaboration (2014). Muon reconstruction efficiency and momentum resolution of the ATLAS experiment in proton-proton collisions at $\sqrt{s}$ = 7 TeV in 2010. Eur. Phys. J. C74, no.9, 3034.

18. ATLAS Collaboration (2009). Muon identification algorithms in ATLAS. ATL-PHYS-PROC-2009-113.

19. ATLAS Collaboration (2011). Study of the Performance of the ATLAS Muon Spectrometer. ATL-MUON-PROC-2011-008.

20. https://www.researchgate.net/figure/269698566_fig14_Figure-17-ATLAS-detector-magnet-system-Courtesy-of-CERN.

21. https://www.fsp103-atlas.de/e17619/e17626/.

22. https://tools.ietf.org/html/rfc1951

23. http://www.zlib.net/

24. http://atlas-computing.web.cern.ch/atlas-computing/packages/athenaCore/athenaCore.php

Chapter 4: The $B_s \to \mu^+\mu^-\mu^+\mu^-$ Decay as a Signature of New Physics

4.1 Introduction

The decay $B_s \to \mu^+\mu^-\mu^+\mu^-$ is a flavor-changing charge-neutral decay that is sensitive to new physics. In the Standard Model, this decay is rare, with a branching ratio in the resonant mode of $BR(B_s \to \varphi(\to \mu\mu)\, J/\psi\, (\to \mu\mu)) < 10^{-8}$[1], and an estimated branching ratio for the non-resonant mode between $BR(B_s \to 4\mu) < 10^{-10}$[2] and $< 10^{-11}$[3]. This decay is enhanced in certain Beyond the Standard Model physics scenarios, for example the supersymmetric mode $B_s \to P(\to \mu\mu)\, S(\to \mu\mu)$. There, the decay is mediated by scalar (S) and pseudoscalar (P) sgoldstino particles, which each decay into a dimuon. This section presents an overview of mediators in three of these models: Horizontal Gauge Bosons, Supersymmetry via sgoldstinos, and the Hidden Sector.

4.2 Mediators of $B_s \to \mu^+\mu^-\mu^+\mu^-$ Decays Beyond the Standard Model

4.2.1 Horizontal Gauge Bosons

Horizontal gauge bosons are described in several models[4,5,6,7], including the experimental signature that would result from the presence of such a field. The weak force acts as the intermediary in interactions between these bosons and Standard Model states. It is thought that the flavor-changing neutral current that horizontal gauge bosons require is suppressed at low energies, but that a high energy collider like the LHC may be able to produce an observable number of them.

Consider the flavor group[7] $SU_L^W(2) \otimes SU_R^H(2) \otimes U^Y(1)$, with the horizontal gauge bosons denoted by R. Normally singlets under $SU_L(2)$, the right-handed quarks and charged leptons are instead represented by a triplet state of the horizontal gauge group $SU_R^H(2)$. The quarks then have the quantum numbers (I_W, I_H, Y): $u_R = \left(0, 1, \frac{4}{3}\right)$, $d_R = \left(0, 1, -\frac{2}{3}\right)$, and $q_{L,I} = \left(\frac{1}{2}, 0, \frac{1}{3}\right)$, where $I \in \{1,2,3\}$ denotes the left-handed flavors. The leptons have a similar structure, with $e_R = (0, 1, -2)$. Left-handed leptons are singlets under the horizontal gauge group $SU_R^H(2)$.

An alternative formulation[6,8] involves an $Sp(6)_L \otimes U(1)_Y$ extension of the electroweak theory, where $Sp(6)_L$ is a compact symplectic group. This model predicts a set of horizontal gauge bosons that do not affect the fermion spectrum. The standard electroweak group $SU(2)_L$ is unified with the horizontal gauge group $SU(3)_H$ to form a simple, anomaly-free Lie group. It is a straightforward generalization of $SU(2)_L$ symmetry to $Sp(6)_L$, with the three doublets of $SU(2)_L$ condensing in a sextet of $Sp(6)_L$. $Sp(6)_L$ can then be broken into the combination $(SU(2))^3 = SU(2)_1 \otimes SU(2)_2 \otimes SU(2)_3$, where each element operates on a different fermion generation $i = 1, 2, 3$. The $SU(2)_L$ gauge bosons (Z and $W^{\pm}$) are given by $\mathbf{A} = \frac{1}{\sqrt{3}}(\mathbf{A_1} + \mathbf{A_2} + \mathbf{A_3})$, where $\mathbf{A_i}$ is the $SU(2)_i$ gauge boson. Of the orthogonal combinations of $\mathbf{A_i}$, $\mathbf{A}' = \frac{1}{\sqrt{6}}(\mathbf{A_1} + \mathbf{A_2} - 2\mathbf{A_3})$ exhibits universality among only the first two generations and can have a mass scale in the TeV range. The gauge bosons $\mathbf{A}'$ are the new horizontal gauge bosons, denoted as Z' and $W^{\pm\prime}$. Reference [6] calculates the expected yield of a horizontal gauge boson decaying into a dilepton state per year at 14 TeV collision energy, for a typical mass of the hypothetical horizontal gauge boson Z' between 1 and 2 TeV, and luminosity $L =$

$10^{34}\ \mathrm{cm^{-2}s^{-1}}$; this gives an integrated luminosity per 10^7 s (year) of ~10^5 $\mathrm{pb^{-1}}$. By comparison, ATLAS in Run-1 took 5.5 $\mathrm{fb^{-1}}$ of data, with a peak instantaneous luminosity of $\sim 4\times 10^{33}\ \mathrm{cm^{-2}\ s^{-1}}$. In 2015, during Run-2, ATLAS has taken 35.9 $\mathrm{fb^{-1}}$ at an instantaneous luminosity of $\sim 10^{34}\ \mathrm{cm^{-2}\ s^{-1}}$[9]. By the end of Run-2, this is expected to rise to $3-4\times 10^{34}\ \mathrm{cm^{-2}\ s^{-1}}$, and ATLAS is expected to take a total of 100 $\mathrm{fb^{-1}}$ during this 2015-2017 period[10]. The model of Reference [6] can be used to predict that there will be $\sim 2.1\times 10^4\ \mathrm{Z'}$ events decaying to a dimuon per year.

The nature of the decays of horizontal gauge bosons are not well-understood, nor are the lifetimes of these possible particles. If they have a non-zero lifetime, they would produce displaced tertiary vertices, where a dilepton decay follows B decay. This $\mathrm{B_s} \to 4\mu$ study seeks BSM physics by reconstructing dimuons from such displaced vertices, and as such the existence of horizontal gauge bosons would significantly affect the measured branching ratio for this process. Therefore, this model should be borne in mind when performing studies of the $\mathrm{B_s} \to 4\mu$ decay.

4.2.2 Supersymmetry and Sgoldstinos

The supersymmetric particle known as the sgoldstino has been suggested as a mediator in the decay $\Sigma^+ \to \mathrm{p}\mu^+\mu^-$, observed by the HyperCP experiment in 2005[11]. This decay had a measured branching ratio of $\left(8.6^{+6.6}_{-5.4}(\mathrm{stat.}) \pm 5.5(\mathrm{syst.})\right)\times 10^{-8}$, higher than most SM estimates[12]. One interpretation[13] calculated that the branching ratio $\mathrm{BR}(\Sigma^+ \to \mathrm{p}\mu^+\mu^-)$ of this decay in the SM should be in the range 1.6×10^{-8} to 9.0×10^{-8}, and the observed decay is in agreement with this. However, a feature of this observation was that the dimuon masses of all three events were equal to within the resolution of the detector, clustering at (214.3 ± 0.5) MeV; the SM expectation is that that region of dimuon invariant mass is flat. This decay can be interpreted as a flavor-changing neutral current interaction, or an internal conversion (Figure 1). This then implies that the dimuon decay was a result of the decay of the Σ^+ into a new neutral particle P^0 and a proton, i.e.

$$\Sigma^+ \to \mathrm{p}^+\mathrm{P}^0, \quad \mathrm{P}^0 \to \mu^+\mu^-.$$

This intermediate process was calculated to have a branching ratio of $\mathrm{BR}(\Sigma^+ \to \mathrm{p}^+\mathrm{P}^0,$ $\mathrm{P}^0 \to \mu^+\mu^-) = \left(3.1^{+2.4}_{-1.9}(\mathrm{stat.}) \pm 1.5(\mathrm{syst.})\right)\times 10^{-8}$. It was estimated[12] that the coincidental probability for this clustering of the three dimuon masses is 0.8%, using a form factor[11] distribution for SM expectations.

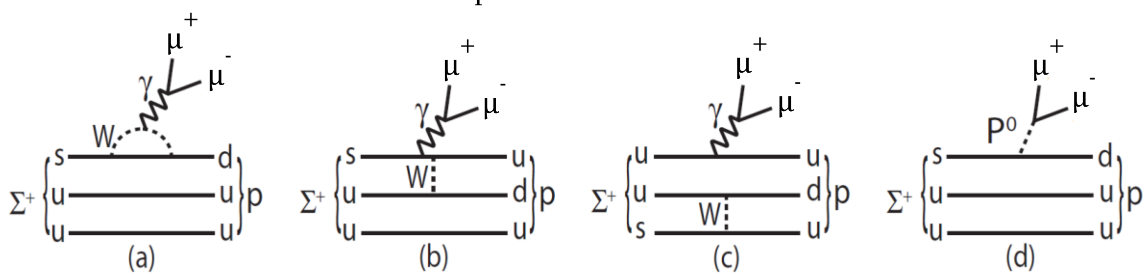

Figure 1: Feynman diagrams for the $\Sigma^+ \to p\mu^+\mu^-$ decay. Diagrams (a) – (c) are Standard Model decays, while (d) is the supersymmetric sgoldstino decay using P^0, a possible pseudoscalar sgoldstino. From [8].

There are two primary theories of sgoldstino coupling[13]: the type-I coupling, which involves a single sgoldstino field, and the type-II, which uses both scalar and pseudoscalar sgoldstinos that couple to two SM fermions in a four-prong vertex. The HyperCP Experiment's potential new particle would be a light pseudoscalar sgoldstino, one that does not interact strongly, decays only into a dielectron, dimuon, or diphoton state, has a $\Delta S = 1, \Delta I = 1/2$ coupling to strange and down quarks, and, like the J/ψ, is short-lived and narrow. Another reason for the pseudoscalar hypothesis, rather than the scalar, is the absence of evidence for it in two-body kaon decays. For example, the decay $K \rightarrow \pi\mu^+\mu^-$ proceeds via the same quark-level transition as the $\Sigma^+ \rightarrow p\mu^+\mu^-$ decay, i.e. a $s \rightarrow d\mu^+\mu^-$ transition, and three different experiments studying these modes (BNL865[14], HyperCP[15], and NA48[16]) have observed no peaks in the dimuon mass distribution in the relevant range.

An sgoldstino will couple to Minimal Supersymmetric Standard Model (MSSM) fields similarly to a goldstino[17,18,19]. Its coupling would be proportional to the ratios of MSSM soft terms, such as the squark and gaugino masses and trilinear couplings, to the supersymmetry-breaking parameter $\sqrt{F}$. Constraints on the sgoldstino coupling act as the limits on $\sqrt{F}$. Certain supersymmetric extensions[17] to the SM allow interactions of sgoldstinos with quarks and gluons that conserve parity but do not conserve quark flavor, and this parity conservation in quark and gluon interactions may not be accidental; for example, it is something that occurs in theories that involve spontaneously broken left-right symmetry, and may provide a solution to the strong-CP problem[20].

Another constraint occurs from the lack of sgoldstino states in the decay $B \rightarrow X_s l^+ l^-$ (where X_s is an arbitrary SM state with net strangeness), measured at Belle[21] and BaBar[22]. Their results have placed a bound on the branching ratio for the pseudoscalar decay of $\leq 8 \times 10^{-8}$ at 95% confidence level. It may be possible for the new state to be observed in the Σ decay while also being absent from the K decay[12]. Both flavor-violating and flavor-blind sgoldstino interactions are relevant to the mechanism of the $B_s \rightarrow 4\mu$ decay. The flavor-violating interactions are of particular relevance to the $B_s \rightarrow 4\mu$ process, as it permits sgoldstino coupling between s and b-quarks. The most likely process[13] for the B_s to produce sgoldstinos is by the decay $B_s \rightarrow SP$, where S and P are the scalar and pseudoscalar sgoldstinos.

4.2.3 The Hidden Sector

It has been suggested that there exists a set of light, sub-GeV states in a "hidden" sector[23], one that is neutral under the SM gauge group, and which can avoid precision flavor and electroweak constraints. These states may not interact via the strong and electromagnetic forces of the SM, but they may interact weakly with SM states, and thus are best probed via experiments at the energy frontier – such as ATLAS at the LHC. It is thought that certain rare SM decays, such as $B_s \rightarrow 4\mu$, will be very sensitive to these new sectors of physics. Understanding the way the hidden sector can be accessed from rare flavor-changing decays requires examination of so-called "portal" operators[23,24].

These operators constitute a systematic way to parameterize the permitted couplings of a generic neutral state in a hidden sector to an SM state. Of particular interest is a set of four of the lowest-dimension portals:

$$H^{\dagger}H(AS + \lambda S^2), \qquad \kappa F^{Y}_{\mu\nu}F'_{\mu\nu}, \qquad Y_N\bar{L}HN, \qquad \text{and} \qquad f_a^{-1}\bar{\psi}\gamma_\mu\gamma_5\psi\,\partial_\mu a,$$

corresponding to the Higgs portal of dimensions 3 and 4, the vector portal of dimension 4, the neutrino portal of dimension 4, and the axion portal of dimension 5, respectively. H is the SM Higgs, λ is a coupling constant, κ is a dimensionless coupling constant that characterizes the mixing of the new vector field with the electroweak field, $F'_{\mu\nu}$ is the field strength, $F^{Y}_{\mu\nu}$ is the hypercharge field strength, Y_N is a dimensionless Yukawa coupling, L is the left-handed weak lepton doublet, ψ is a generic SM fermion, f_a^{-1} is one over the axion decay constant, and N, A, a, and generic neutral state S represent fields associated with new light states[25].

There are two main models of hidden sector interactions with rare B decays: the first[24] is a minimal extension of the Standard Model by a scalar singlet interacting through the Higgs portal, and a pseudoscalar singlet coupled to the SM via the axion portal. The second[24] uses a combination of Higgs and vector portals enhancing rare B decay modes. Both of these models show that the hidden sector may be accessed through flavor-changing four lepton decays, such as the $B_s \rightarrow \mu^+\mu^-\mu^+\mu^-$.

4.3 Predictions of Yield from BSM Theories

The models presented here constitute known possible contributors to enhancement of the $B_s \rightarrow 4\mu$ decay beyond what is predicted by the Standard Model. However, this search will be model-blind. This is because the theories of horizontal gauge bosons and the hidden sector are not well-developed enough to make predictions, although the supersymmetric theory, involving the decay of B-mesons into sgoldstinos, is. Rather than looking for an enhancement from a given theory, we will be looking for any rate difference substantially above – or below – SM predictions. If a branching ratio is measured to be above SM predictions, it would imply that some BSM physics process is yielding additional $B_s \rightarrow 4\mu$ decays using a BSM mediator, such as sgoldstinos. Equally so, a branching ratio smaller than the SM predicts could indicate that some currently-invisible physics process is suppressing $B_s \rightarrow 4\mu$ decays from our ability to detect, itself an indicator of new physics. These scenarios assume that some number of events are detected, however; if no events are detected, then a new limit on the branching ratio of the BSM $B_s \rightarrow 4\mu$ decay can be set.

These limits, and the branching ratios that would result from various numbers of events from the $B_s \rightarrow 4\mu$ decay, can be estimated using the CL_s[26,27] method. Originally developed for Higgs searches at LEP, CL_s represents an approximate confidence in the signal-only hypothesis. The method enables one to calculate two estimators, confidence levels CL_{s+b} and CL_b, which give the level of compatibility with the signal-plus-background and background-only hypotheses. The signal confidence level $CL_s = CL_{s+b}/CL_b$ is used primarily in this analysis, however, as this protects against negative statistical fluctuations of the background. Using CL_{s+b} risks these fluctuations causing exclusion of the null hypothesis, in which only the background is present, or to signal exclusions without any experimental sensitivity.

CL_{s+b} and CL_b are defined as the probability for their respective hypotheses to have a value of Q less than or equal to that observed in the data:

$$CL_{s+b} = P_{s+b}(X_{s+b} \leq X_{obs}), \qquad CL_b = P_b(X_b \leq X_{obs}),$$

where X_{s+b} and X_b are test statistics which discriminate between signal-like outcomes and background-like outcomes:

$$X_{s+b} = \frac{e^{-(s+b)}(s+b)^d}{d!}.$$

Here, s is defined as the expected amount of signal, b is the expected number of background events, and d is the observed number of events. The value of s is varied to calculate the upper limit of the branching ratio; it is calculated in full in section 5.7. For the purposes of this estimate, we will assume negligible background b; b is taken to be 0, and so $s + b = s$. The observed number of events, d, is varied between 0, 6, and 60, representing no events detected, the SM expectation (calculated in section 5.2), and a significant enhancement from BSM physics respectively.

$1 - \mathrm{CL_b}$ can be used as a p-value to claim evidence or observation of new particles, with 3σ evidence at 95% (90%) confidence level corresponding to $1 - \mathrm{CL_b} = 2.7(1.35)\times10^{-3}$ and 5σ discovery at 95% (90%) confidence level corresponding to $1 - \mathrm{CL_b} = 5.73(2.87)\times10^{-7}$. $\mathrm{CL_s} = \mathrm{CL_{s+b}}/\mathrm{CL_b}$, meanwhile, can be used to set the upper limits on the branching fractions of the SM and BSM $\mathrm{B_s} \rightarrow 4\mu$ decay. Since the background b is taken to be 0, the probability $\mathrm{P_s}(\mathrm{X_s} \leq \mathrm{X_{obs}})$ can be directly calculated as:

$$\mathrm{CL_s} = \mathrm{P_s}(\mathrm{X} \leq \mathrm{X_{obs}}) = \int_0^{s'} \frac{e^{-s}(s)^d}{d!}\, ds,$$

where the test statistic is integrated over all possible final outcomes s' with test statistics less than or equal to the observed one. Table 1 shows the expected $\mathrm{BR}(\mathrm{B_s} \rightarrow 4\mu)$ at each of the number of events, and the upper limit at 95% and 90% confidence level.

We can also make an estimate of the upper limit of the branching ratio of the $\mathrm{B_s} \rightarrow \mathrm{SP}$ decay. A recent paper**[28]** from LHCb placed a limit on the $\mathrm{BR}(\mathrm{B_s} \rightarrow \mathrm{SP} \rightarrow 4\mu) < 2.2\times10^{-9}$. It should be noted that LHCb's measurement assumes that the sgoldstinos have zero lifetime; while our current analysis is designed for prompt S and P decays, the final search will assume that these SUSY particles have non-zero lifetime, and thus will exhibit tertiary displaced vertices. This means that the LHCb limit cannot be compared directly to our analysis, but we can approximate the $\mathrm{BR}(\mathrm{B_s} \rightarrow \mathrm{SP})$ using LHCb's measurement. It has been estimated that the $\mathrm{BR}(\mathrm{S} \rightarrow 2\mu)$ and $\mathrm{BR}(\mathrm{P} \rightarrow 2\mu)$ are approximately 0.33**[29]**, which gives us a limit of $\mathrm{BR}(\mathrm{B_s} \rightarrow \mathrm{SP}) < 2.0\times10^{-8}$.

Observed Events	0	6	60
Expected 90% CL Limit	$< 4.31\times10^{-11}$	$< 1.90\times10^{-10}$	$< 1.28\times10^{-9}$
Expected 95% CL Limit	$< 5.93\times10^{-11}$	$< 2.13\times10^{-10}$	$< 1.34\times10^{-9}$
$\mathrm{BR}(B_s \rightarrow 4\mu)$	N/A	1.08×10^{-10}	1.08×10^{-9}
$\mathrm{BSM\ BR}(B_s \rightarrow 4\mu)$	N/A	N/A	9.7×10^{-10}

Table 1: The expected branching fractions of the $B_s \rightarrow 4\mu$ decay if a given number of events are observed, and their associated upper limits at 90% and 95% CL. This also includes the BSM branching ratio, if more than 6 events (the SM expectation) are detected.

4.4 References

1. Aaij, R., & LHCb Collaboration (2013). Search for rare $B^0_{(s)} \rightarrow \mu^+\mu^-\mu^+\mu^-$ Decays. Phys. Rev. Lett. 110, 211801.

1. Melikhov, Dmitri, & Nikitin, Nikolai (2004). Rare radiative leptonic decays $B_{d,s} \rightarrow l^+l^-\gamma$. Phys. Rev. D 70, 114028.

2. Dincer, Yusuf, and Sehgal, L. M. (2003). Electroweak effects in the double Dalitz decay $B_s \rightarrow l^+l^-l^+l^-$. Physics Letters B 556, 169–176.

3. Wilczek, F., & Zee, A. (1979). Horizontal Interaction and Weak Mixing Angles. Phys. Rev. Lett. 42, 421.

4. Hou, Wei-Shu, & Soni, A. (1985). Experimental Consequences of a Horizontal Gauge Model for CP Nonconservation. Phys. Rev. Lett. 54, 2083.

5. Bagneid, Ali A. (2002). Identification of a horizontal gauge boson in hadronic collisions. Eur. Phys. J. C22, 743-747.

6. Bengtsson, Hans-Uno, Hou, Wei-Shu, Soni, A., & Stork, D. H. (1985). Signatures for Horizontal Gauge Bosons in Very Energetic Hadronic Collisions. Phys. Rev. Lett. 55, 2762.

7. Kuo, T. K., & Nakagawa, N. (1984). $S_{p_L}(6) \times U_{\gamma}(1)$ extension of the electroweak theory. Phys. Rev. D 30, 2011(R).

8. HyperCP Collaboration (2005). Evidence for the decay $\Sigma^+ \to p\mu^+\mu^-$. Phys. Rev. Lett. 94, 021801.

9. https://atlas.web.cern.ch/Atlas/GROUPS/DATAPREPARATION/DataSummary

10. ATLAS Collaboration (2016). ATLAS Run-2 status and performance. Nucl. Part. Phys. Proc. 270-272, 3-7.

11. He, Xiao-Gang, Tandean, Jusak, and Valencia, G. (2005). The Decay $\Sigma^+ \to pl^+l^-$ within the Standard Model. Phys. Rev. D72, 074003.

12. Valencia, G. (2008). $\Sigma^+ \to p\mu^+\mu^-$: Standard Model or New Particle? Presented at Rencontres de Moriond, QCD and High Energy Interactions. AIP Conf. Proc. 870, 283.

13. Demidov, S.V., & Gorbunov, D. S. (2012). Flavor violating processes with sgoldstino pair production. Phys. Rev. D85, 077701.

14. Ma, H., *et al.* (1999). A New Measurement of the Rare Decay $K^+ \to \pi^+\mu^+\mu^-$. Phys. Rev. Lett. 84, 2580-2583.

15. Park, H. K., *et al.* (2001). Observation of the Decay $K^- \to \pi^-\mu^+\mu^-$ and Measurements of the Branching Ratios for $K^\pm \to \pi^\pm\mu^+\mu^-$. Phys. Rev. Lett. 88, 111801.

16. Batley, J. R., *et al.* (2004). Observation of the rare decay $K_s \rightarrow \pi^0\mu^+\mu^-$. Phys. Lett. B599, 197-211.

17. Gorbunov, D. S., & Rubakov, V. A. (2005). On sgoldstino interpretation of HyperCP events. Phys. Rev. D73, 035002.

18. Bhattacharya, T., & Roy, P. (1988). High-energy equivalence theorems in spontaneously broken gauge theories. Phys. Lett. B206, 655.

19. Gorbunov, Dmitry S., & Semenov, Andrei V. (2001). CompHEP Package with Light Gravitino and Sgoldstinos. arXiv:hep-ph/0111291.

20. Mohapatra, Rabindra N., Rasin, Andrija, & Senjanovic, Goran (1997). C, P, and Strong CP in Left-Right Supersymmetric Models. Phys. Rev. Lett. 79, 4744.

21. Belle Collaboration (2005). Improved Measurement of the Electroweak Penguin Process $B \rightarrow X_s l^+ l^-$. Phys. Rev. D72, 092005.

22. BABAR Collaboration (2004). Measurement of the $B \rightarrow X_s l^+ l^-$ Branching Fraction with a Sum over Exclusive Modes. Phys. Rev. Lett. 93, 081802.

23. Batell, Brian, Pospelov, Maxim, & Ritz, Adam (2011). Multi-lepton Signatures of a Hidden Sector in Rare B Decays. Phys. Rev. D83, 054005.

24. Patt, Brian, & Wilczek, Frank (2006). Higgs-field Portal into Hidden Sectors. arXiv:hep-ph/0605188.

25. Alekhin, Sergey *et al.* (2015). A Facility to Search for Hidden Particles at the CERN SPS: the SHiP physics case. arXiv:1504.04855.

26. LHCb Collaboration (2016). Search for decays of neutral beauty mesons into four muons. LHCb-PAPER-2016-043.

27. Read, A. L. (2002). Presentation of search results: the CL_s technique. Nucl. Instrum. Meth. A434, 435.

28. Junk, Thomas (1999). Confidence Level Computation for Combining Searches with Small Statistics. Nucl. Instrum. Meth. A434, 435-443.

29. Gorbunov, D., and Rubakov, V. (2001). Kaon physics with light sgoldstinos and parity conservation. Phys. Rev. D64, 054008.

Chapter 5: Building a Foundation for the $B_s \to \mu^+\mu^-\mu^+\mu^-$ Search with ATLAS

5.1 Introduction

Presented here are preparations for a search for the $B_s \to 4\mu$ decay for those cases in which four muons have been reconstructed to a single vertex at pseudorapidities $|\eta|$ with magnitude less than 2.5, i.e. in both the barrel and endcap regions of the ATLAS detector. This analysis will search for $B_s \to 4\mu$ events mediated by Beyond the Standard Model interactions, in 100 fb^{-1} of 2015 Run-2 13 TeV data. LHCb set a limit on the rate of $B_s \to 4\mu$ in 2013[1], by considering only events in which the intermediate particle decay vertices are not significantly displaced from the B_s decay vertex. LHCb interpreted their result for the sgoldstino decay $B_s \to SP$, where S is the scalar sgoldstino and P is the pseudoscalar sgoldstino. The $B_s \to 4\mu$ decay is expected to have a lower combinatorial background than the $B_s \to 2\mu$ decay, one of the rarest processes ever observed[2] at the time of its measurement.

The ATLAS detector is expected to have comparable efficiency for detecting the $B_s \to 4\mu$ decay as the LHCb for the 2015-2017 run[3]. The efficiency can be estimated using the $B_s \to J/\psi\,(\mu^+\mu^-)\varphi(K^+K^-)$ decay as a reference channel; the relative efficiency can be assumed to be proportional to the reference channel due to similar kinematic decays. The efficiency of ATLAS relative to LHCb for the $B_s \to 4\mu$ decay for 2011 7 TeV data can be estimated as $\varepsilon = N^L_{ATLAS}(B_s \to 4\mu)/N^L_{LHCb}(B_s \to 4\mu)$, where $N^L_x(B_s \to 4\mu) = N_x(B_s \to 4\mu)/L_{int,x}$ is the number of events expected per unit integrated luminosity (fb^{-1}) in detector x. Here, ε is the relative efficiency, $N_x(B_s \to 4\mu)$ is the number of events expected in detector x, and $L_{\text{int,x}}$ is the integrated luminosity recorded by detector x during the run in question. To calculate the relative efficiency ε of the signal channel more precisely, it is necessary to factor in the relative hadronic efficiency:

$$\varepsilon = \frac{N_{ATLAS}\left(B_s \to J/\psi(\mu^+\mu^-)\varphi(K^+K^-)\right)}{N_{LHCb}\left(B_s \to J/\psi(\mu^+\mu^-)\varphi(K^+K^-)\right)} \times \frac{L_{\text{int,LHCb}}}{L_{\text{int,ATLAS}}} \times \varepsilon_h^2. \quad (1)$$

However, the relative hadronic efficiency ε_h can be estimated as the ratio of ATLAS's and LHCb's hadron efficiencies; this is expected to be ~1[3].

To calculate the relative efficiency, we use 2011 yields from ATLAS and LHCb: $N_{ATLAS}\left(B_s \to J/\psi\,(\mu^+\mu^-)\varphi(K^+K^-)\right) = 22{,}670$[4] from $L_{\text{int,ATLAS}} = 4.9$ fb^{-1} of 7 TeV data, and $N_{LHCb}\left(B_s \to J/\psi\,(\mu^+\mu^-)\varphi(K^+K^-)\right) = 21{,}200$[5] from $L_{\text{int,LHCb}} = 1.03$ fb^{-1} of 7 TeV data. This yields, for 2011, $\varepsilon = 0.225$. However, ATLAS took ~5 times more data in 2011, meaning that despite the efficiency difference, ATLAS was still competitive with LHCb in 2011 for the purposes of measuring B_s decays to muons.

The upgrades to ATLAS are expected to change these efficiencies: ATLAS's upgrades include additional prescaling (in which only a fraction of events are saved) on several triggers, to ensure that the ATLAS triggering system can handle the higher data rates of the Run-2 LHC. This means that ATLAS will detect fewer $B_s \to 4\mu$ per fb^{-1} in Run-2 than in Run-1. However, ATLAS expects to take 100 fb^{-1}[6] of data from the 2015-2017 run, while LHCb expects to take only 5 fb^{-1}, increasing the $L_{\text{int,ATLAS}}/L_{\text{int,LHCb}}$ ratio by a factor of 4. It is predicted, based on dimuon trigger studies[6], that the $B_s \to J/\psi\,(\mu^+\mu^-)\varphi(K^+K^-)$ yield at ATLAS in the 2015-2017 13 TeV data will be 327,900 events; these represent events that are both detected by the triggers and reconstructed offline. LHCb is predicted to acquire 212,000 events, if one assumes a linear increase from 2011: $2 * 5 * 21{,}200$, where the 5 comes from the increase in total integrated luminosity, and the 2 from the doubling of the production cross-section between 2011 and 2015[7]. All in all, this gives an $\varepsilon = 0.077$. Combined with the ~20x greater data ATLAS will be taking in 2011, this means that ATLAS will remain competitive over the whole dataset with LHCb in Run-2. This number is expected to have some minor but yet uncalculated uncertainties.

Thus, ATLAS is expected to have efficiency competitive with the LHCb. What is not estimated here is the level of background, which plays a critical role in the measurement as well. However, in a comparison of the ATLAS and LHCb $B_s \rightarrow 2\mu$[2,8] and $B_s \rightarrow J/\psi\ \varphi$[9,10] measurements, the precisions achieved (including backgrounds) by ATLAS and LHCb were similar. It is thus reasonable to expect competitive treatment of the background level, and consequently also competitive performance in the $B_s \rightarrow 4\mu$ channel. Moreover, ATLAS and LHCb search for these new physics process in very different ways – LHCb's search is focused on $B_s \rightarrow 4\mu$ decays where the intermediate BSM decay products have near-zero lifetime, while this search will eventually focus on decays where these lifetimes are high enough that tertiary displaced vertices can be detected.

5.2 Selection of Triggers for the Signal

In ATLAS, the raw data rate, generated by collisions that occur every 25 ns, is so high that recording all the data is both impossible and undesirable. Being able to select events based on what triggers they activate, in order to decrease the total amount of data and increase the amount of signal data recorded relative to the background, is necessary to performing an analysis. To identify which triggers are optimal for this analysis, a study of the efficiencies of the High-Level Triggers was performed. The relevant triggers are muon triggers, which activate when a specified number of muons are recorded above or at some specific transverse momenta. As an example, the trigger “2mu10” activates when the ATLAS detector detects at least two muons from the same crossing and both muons have a p_T greater than or equal to 10 GeV. Other examples are the “mu18” trigger, which activates when at least one muon has a p_T greater than 18 GeV, and “3mu4,” which will trigger when at least three muons from the same event are detected with p_T each greater than 4 GeV. There are further variants as well, such as the _bBmumu triggers, which select events where the tracks of a muon pair have been successfully fitted to a common vertex with an invariant mass between 4 and 8.5 GeV.

Many B-Physics analyses make use of triggers that look for two muons (the 2muX triggers). The reason for this is that many B-physics decays produce a J/ψ meson, which decays ~6% of the time to a dimuon. This creates a very strong and clean signal which can be easily detected by ATLAS. A part of this study was focused on finding which 2muX triggers were most efficient for the signal. ATLAS also has three-muon triggers. Given that our signal involves four muons, the 3muX triggers were studied as well, in order to determine their potential for contributions to the measurement. A set of 12 candidate triggers, listed in Table 1, were examined using $B_s \rightarrow 4\mu$ MC data.

To determine the quality of each of these triggers, the trigger efficiency $S_{trigger}/S_{total}$ is studied. This figure of merit is a measure of the fraction of the events that fire a particular trigger. An event is included in the dataset if it fires at least one of the twelve triggers being studied; S_{total} is the total number of events in the dataset. For each of the twelve triggers, $S_{trigger}$ is defined as the number of events that fire that particular trigger. This measurement relies on MC signal events from the non-resonant SM $B_s \rightarrow 4\mu$; this MC dataset includes cuts on the muon of $p_T > 3500$ MeV and $|\eta| < 2.6$. The result of this study can be found in Table 1; all of these triggers are being used in the analysis.

Trigger	$\mathbf{S_{trigger}/S_{total}}$	**Prescaled? (y/n)**
2mu4_bBmumu	0.039	Yes
2mu6_bBmumu	0.013	No
mu6_mu4_bBmumu	0.031	Yes
3mu6	0.002	No
3mu4	0.014	No
2mu10	0.011	No
2mu6	0.096	No
2mu4	0.369	Yes
mu10	0.144	Yes
mu11	0.107	Yes
mu14	0.047	Yes
mu18	0.017	Yes

Table 1: The efficiencies and prescaling of the triggers being used in this analysis, all from the SM $B_s \rightarrow 4\mu$ process; the SM and BSM MC are essentially identical for the purposes of these triggers.

From this table, it appears that 2mu4 is the primary contributor to our signal, followed by mu10, mu11, and 2mu6. However, the 2mu4, mu10, and mu11 triggers are heavily prescaled, meaning that only a fraction of events is kept, the fraction being different for each trigger. This is done because these triggers activate very frequently, and saving more than a fraction of the events would overload the computing system. For greatest sensitivity to the signal, the BSM $B_s \rightarrow 4\mu$, we need to keep as much data as possible. Consequentially 2mu6, which is not prescaled, is expected to be our primary trigger for the 2015-2017 data taking.

Using Equation 2, it is possible to estimate the upper limit of the number of $B_s \rightarrow 4\mu$ events we anticipate in the 100 fb^{-1} of data this project will be analyzing. We compute:

$$\# \text{ events} = L_{int} \cdot \sigma(B_s)_{ATLAS} \cdot BR(\text{decay}) \cdot (\text{2mu6 trigger efficiency}), \qquad (2)$$

where "# events", BR(decay) correspond to the B_s decay of interest, $\sigma(B_s)$ the approximate production cross-section of the B_s from 13 TeV pp collisions in ATLAS (estimated in section 5.4), and "2mu6 trigger efficiency" is 0.096, from Table 1. For 100 fb^{-1}, without taking cuts into account, we can place an upper limit of ~1002 events of the resonant decay, ~6 of the non-resonant decay, and between ~2 and ~7 events for the BSM $BR(B_s \rightarrow 4\mu) = [3.5\times10^{-11}, \ 1.3\times10^{-10}]$. Beginning in section 5.4, strategies are explored to reduce the backgrounds for this decay.

5.3 Truth-Level Studies of the L1Topo Trigger Efficiency

In an effort to make the ATLAS data rate more manageable between the 2011 run and 2015's, a new element was added to the Level-1 trigger scheme, called the Topological Processer (L1Topo)[12]. If 2011's trigger rates are to be maintained without unduly raising thresholds or prescaling, which may reduce useful data from channels of interest, the new trigger system had to be based on topological information on jet or muon direction in space, or combinations of the object properties such as invariant mass, opening angle, etc. Many decays of interest to ATLAS have specific topologies that can be used to identify them, and using only the E_T and p_T thresholds of the L1Calo and L1Muon triggers would make them harder to identify at this heightened luminosity. An investigation was made regarding the usefulness of the L1Topo trigger for the $B_s \rightarrow 4\mu$

decay search. Fully simulated MC samples including the L1Topo trigger were not available, thus to answer this, a study on the truth-level trigger efficiencies was necessary, to determine if the modern LHC would necessitate special triggers making use of L1Topo information.

A study was performed on a 20k event $B_s \rightarrow 4\mu$ Monte Carlo dataset, in order to determine the truth trigger efficiencies of the dominant triggers in Table 1. In general, the trigger efficiency is the number of events remaining after a dataset has been passed through the trigger, divided by the original number of events. The truth trigger efficiency is a simplified version of the trigger efficiency. Only the generated events are used, i.e. data prior to simulation, reconstruction, etc., and triggers – which are normally added during the simulation/reconstruction phase – are emulated with corresponding p_T, pseudorapidity, etc. cuts. The truth trigger efficiency tends to be higher than the trigger efficiency, due to the truth efficiency's not including the geometrical inefficiencies of the detector and the inefficiencies of reconstruction. It was studied prior to large datasets being generated, simulated, and reconstructed, in order to determine the number of events that need to be generated for the analysis.

Two different versions of the 20k event signal dataset were used:

- A dataset with no cuts applied other than those usually used in ATLAS generation; this is called the "Raw Dataset." Note that this includes a $|\eta| < 2.5$ cut on the B_s.
- A dataset where the cuts $p_T > 8$ GeV and $|\eta| < 2.5$ were applied to the B_s; a similar cut was placed on the anti-b-quark during generation; this is called

the "Modified Dataset." These sorts of cuts are often applied to large-scale data generation to stop the generation program before it begins hadronization, which is very CPU-time-consuming. Applying these cuts allows large datasets, such as the five million event backgrounds being used in this analysis, to be generated in a reasonable time frame.

This latter dataset uses the same fiducial volume as is used to evaluate acceptance and efficiency for the Run-1 $B_s \rightarrow \mu^+\mu^-$ analysis[8], which did not require any new triggers in L1Topo. The concern is that the L1Topo selection used for other decay channels may be inefficient for the $B_s \rightarrow 4\mu$ decay. Ideally, this is tested on the Raw Dataset, as this gives the clearest idea of what effect the topological triggers have. However, for effective and timely production, large-scale Monte Carlo data uses similar preselection as in the Modified Dataset. As such, a similar test needs to be performed on the Modified Dataset.

For each dataset, two different sets of selection criteria were studied:

- Several p_T cuts, meant to simulate the effects of p_T thresholds at the trigger and offline analysis levels on the signal yield:
    - $p_T(4\mu) > 4$ GeV (each of the four muons must have a $p_T > 4$ GeV)
    - $p_T(2\mu) > 4$ GeV, $p_T(2\mu) > 6$ GeV (two muons must have $p_T > 4$ GeV, the other two with $p_T > 6$ GeV)
    - $p_T(4\mu) > 1$ GeV
    - $p_T(2\mu) > 1$ GeV, $p_T(2\mu) > 4$ GeV

- $p_T(1\mu) > 1$ GeV, $p_T(3\mu) > 4$ GeV

- Two mass-window cuts, meant to both evaluate the efficiency of a realistic dimuon trigger cut, as well as some of the mass-based L1Topo triggers:
  - Invariant mass of at least one (opposite-signed) muon pair between 3 and 8 GeV
  - Invariant mass of at least one (opposite-signed) muon pair between 4 and 8 GeV

These two mass windows correspond to L1Topo dimuon triggers. The invariant mass M can be calculated by:

$$M = \sqrt{(E_1 + E_2)^2 - \left(p_{x,1} + p_{x,2}\right)^2 - \left(p_{y,1} + p_{y,2}\right)^2 - \left(p_{z,1} + p_{z,2}\right)^2}, \qquad (3)$$

where E is the total particle energy, and $p_{x/y/z}$ are the momenta. The results can be found in Table 2.

Cut Applied (GeV)	**# of Events (Raw)**	**Trigger Efficiency (Raw)**	**# of Events (Modified)**	**Trigger Efficiency (Modified)**
None (Uncut)	21,863	N/A	17,814	N/A
p_T (4μ) > 4	21	0.1%	84	0.47%
p_T (2μ) > 4, p_T (2μ) > 6	17	0.08%	60	0.34%
p_T (4μ) > 1	2559	11.7%	5681	31.9%
p_T (2μ) > 1, p_T (2μ) > 4	486	2.22%	1849	10.4%
p_T (1μ) > 1, p_T (3μ) > 4	117	0.54%	477	2.68%
3 < Mass (2μ) < 8	11482	52.5%	9903	55.6%
4 < Mass (2μ) < 8	1634	7.47%	1408	7.90%

Table 2: Predicted efficiencies for seven triggers used in this analysis. Note that the number of initial events was 17,814, not 20,000, in this case.

It is clear from the last two rows that a significant amount of the dimuon invariant mass spectrum lies between 3 and 4 GeV. Consequently, any selection criteria based on mass would need to include the range < 4 GeV, while the existing L1Topo selection does not include these low-mass regions and thus should not be used. This study confirmed that the 2mu6 trigger (discussed in section 5.2) will be the primary trigger made use of in this analysis for the 2015-2017 data.

Following this, official generation of five million events was carried out for the SM $B_s \to 4\mu$ decay. All the backgrounds for the project (detailed in the next section) also had five million events generated, except for the $B_d \to (K^* \to K\pi)\mu\mu$ decay, for which fifteen million events were generated. This larger number is due to the $B_s \to 4\mu$ project sharing this dataset with the $B_d \to K^*\mu\mu$ project, which has different selection requirements. The generations of these backgrounds made use of cuts on both muons of $|\eta| < 2.6$ and $p_T > 3500$ MeV, and cuts on the final hadrons of $|\eta| < 2.6$ and $p_T >$ 500 MeV. The $B_s \to J/\psi\, \varphi$ is the exception, as it had no final hadrons, and had cuts on all four muons of $|\eta| < 2.6$ and $p_T > 3500$ MeV.

5.4 The Backgrounds

With the trigger studies out of the way, in this section we begin discussion of offline analysis. There are seven decay channels that could provide a false signal, or background. These are shown in Table 3 along with the Monte Carlo sample sizes studied. For five of these backgrounds – $B_s \to \varphi(\to KK)\mu\mu$, $B_d \to \omega(\to \pi\pi)\mu\mu$, $B_d \to \rho^0(\to \pi\pi)\mu\mu$, $B_s \to \psi(2S)(\to \mu\mu)K^*(\to K^+\pi^-)$, and $B_d \to K^*(\to K^+\pi^-)\mu\mu$ – it is possible for the pion or kaon final states to be misidentified as muons at a rate of 0.4% (kaon) or 0.2% (pion)[8]; combined with the dimuon final states, these misidentifications

Decays	Total Events Simulated	Scaling Factor
$B_s \to 4\mu$ (SM)	4,953,000	5.58×10^{-3}
$B_s \to \varphi(\to KK)\mu\mu$	4,900,400	3.40×10^{-4}
$B_d \to \omega(\to \pi\pi)\mu\mu$	4,949,400	2.35×10^{-4}
$B_d \to \rho^0(\to \pi\pi)\mu\mu$	4,957,800	1.72×10^{-5}
$B_s \to \psi(2S)(\to \mu\mu)K^*(\to K^+\pi^-)$	4,963,800	1.16×10^{-4}
$B_s \to J/\psi\,(\to \mu\mu)\varphi(\to \mu\mu)$	4,971,300	1
$B_d \to K^*(\to K^+\pi^-)\mu\mu$	4,896,500	1.23×10^{-3}

Table 3: A listing of the total number of events per background Monte Carlo dataset. Note that luminosity and similar features were not considered during generation; these are lump sums of events which can be scaled to any branching ratio or luminosity, and are used primarily to study pion and kaon misidentification rates. The scaling factors include misidentification rates (where applicable), the relative total branching ratio to the $B_s \to J/\psi\,\varphi$ decay, and a factor accounting for the different B_d and B_s production rates (where applicable); when the factors are applied to the other samples, they scale those samples' integrated luminosity to that of the $B_s \to J/\psi\,\varphi$ decay.

could produce fake signals. The $B_d \to K^*\mu\mu$ sample was generated under slightly different conditions, in which the same p_T selection criteria normally applied to the muons were also applied to the hadrons, because it is shared between this and another analysis. The SM non-resonant $B_s \to 4\mu$ decay and the resonant $B_s \to J/\psi\,(\to \mu\mu)\varphi(\to \mu\mu)$ decay have final states identical (up to kinematics) to the BSM $B_s \to 4\mu$ decay, and are thus a significant contributor to the background for the $B_s \to 4\mu$ BSM decay. However, if the number of signal events measured is in excess of what we expect from the Standard Model backgrounds, then it can be assumed to come from BSM physics. Studying these Monte Carlo datasets allows us to predict the absolute level to which these channels would contribute to the background.

The integrated luminosity L_{int} that these Monte Carlo datasets represent, after the application of the associated scale factors, can be estimated from Equation 2 using the resonant decay as a reference point by:

$$L_{int} = {}^{\#\ \text{resonant events}}\!\Big/_{\sigma(B_s) * BR(B_s \rightarrow J/\psi\,(\rightarrow \mu\mu)\varphi(\rightarrow \mu\mu))}. \quad (4)$$

Here, "# resonant events" is the number of events in the reference resonant dataset (4,971,300 events), $BR(B_s \rightarrow J/\psi\,(\rightarrow \mu\mu)\varphi(\rightarrow \mu\mu)) = 1.8\times10^{-8}$, and $\sigma(B_s)$ is the production cross-section of the B_s from 13 TeV pp collisions in ATLAS. The ATLAS $\sigma(B_s)$ has not yet been measured for 13 TeV, but can be estimated from 7 TeV data from ATLAS and LHCb. For ATLAS B^+ data, the $\sigma(B^+)$ was measured in 2013[13] to be ~10.6 μb. In 2013, LHCb measured[14] the 7 TeV production cross-section of both the B^+ and B_s to be ~38.9 μb and ~10.5 μb, respectively. The difference in the production cross-sections recorded by LHCb and ATLAS is substantial because they were performed in different rapidity regions: ATLAS is a transverse detector and measured the $\sigma(B^+)$ in the $|y| \leq 2.5$[13] region, while LHCb is a forward detector and measured the $\sigma(B^+)$ and $\sigma(B_s)$ in the $2.0 \leq y \leq 4.5$[14] region. However, the relative cross-sections of B_s to B^+ will be approximately the same: the production mechanism of B_s is dominated by the bonding of the s-quark to the b-quark from the quark sea during the interaction, identically to the light u-quark case[3]. We calculate $\sigma(B_s)_{ATLAS} \approx \sigma(B^+)_{ATLAS} \cdot \frac{\sigma(B_s)_{LHCb}}{\sigma(B^+)_{LHCb}} = 2.9$ μb for 7 TeV data. To estimate the cross-section for 13 TeV, we multiply this by 2[15], for $\sigma(B_s)_{ATLAS} \approx 5.8$ μb. This gives an L_{int} for the Monte Carlo dataset of ~48,000 fb^{-1}.

This represents an amount of data greater than ATLAS will ever take; however, datasets of this size are commonly used because of the rarity of these decays, and the need to study them to understand their effect on the background of our signal. These backgrounds constitute "peaking" backgrounds, backgrounds that create an invariant mass peak in the four-muon mass reconstruction that could overwhelm the peak of the signal. For the analysis to proceed, these backgrounds must be studied, to reduce them to the point where they no longer overwhelm the signal. The first step to studying them is to simulate these decays in ATLAS's geometry using Monte Carlo.

5.5 Simulating the Backgrounds for the ATLAS Geometry

All ATLAS analyses that make use of Monte Carlo datasets are required to have those datasets officially generated, created by code that has been vetted by experts and generated using specific, standardized techniques. To perform this analysis, the backgrounds were simulated in the ATLAS geometry for the 13 TeV run conditions. Creation of a Monte Carlo dataset has several steps: generation (where the initial pp collision events are created), simulation (simulating passage of the generated particles through the ATLAS detector material), digitization (simulating detector electronic response to the particles' energy losses in the detector material; the output is then similar in form to data coming out of the real detector), reconstruction (where the digitized data are reconstructed into tracks and energy deposits), and production of AOD (where the reconstructed data are converted into a form more easily analyzed).

The generation of events is driven by specific Python code. Creating this code involves describing the decay in the Python file itself, and identifying the correct decay models to use. These decays are expressed in the generation code, called "Job Options"

(JO). It also involves applying selection requirements, or cuts. As an example, take the $B_s \rightarrow \psi(2S)(\rightarrow \mu\mu)K^*(\rightarrow K^+\pi^-)$ decay. In this case of the decay of the B_s, the model used is SVV_HELAMP[16], which describes the decay of a scalar meson into two vector mesons, with the decay amplitude specified by the helicity amplitudes, which are themselves specified as magnitude and phase. The K^* is decayed to a kaon and a pion using the VSS (Vector to Scalar, Scalar) model. The $\psi(2S)$ is decayed to two muons using the VLL (Vector to Lepton, Lepton) model. Four additional models are used in other decays, including: PHSP[16] (Generic phase space to n-bodies), a model in which all spins are averaged; SVS[16] (Scalar to Vector, Scalar); PVV_CPLH[16] (Pseudoscalar into Vector, Vector), allowing for CP violating time asymmetries including different mass eigenstates; and BTOSLLBALL[16] (b-quark to s-quark transition with emitted lepton pair). Once the code is assembled, some events can be generated, which must then be validated before official generation can occur.

In general, validation requires several things to be checked:

- If the JO has any exclusive decay modes (which all of our MC does), then the MC must be checked to ensure that that mode is present in all events. So, for example, the $B_d \rightarrow \rho\ \mu\mu$ must have a B_d decaying to a ρ and a dimuon in every event.
- If certain, specific states are being produced for study, such as excited quarkonium, then every event must be checked to ensure that they all contain this state, and that the state has the correct mass and width.
- If cuts are applied to final state kinematic variables (for example, p_T and pseudorapidity cuts on muons), then the MC must be checked to ensure that those

cuts are applied. This is done by plotting the relevant variables of the particle, and checking to ensure that they fit the criteria.

- The MC must also be checked for inconsistencies between modelling systems. For example, if the PHOTOS[17] model is being used, unstable particle decays must be checked for soft photon generation, made to account for radiative corrections. Other issues must also be checked, such as different particle masses between the PYTHIA[18] and EvtGen[19] generation models, in case of inconsistency of particle data between the two generators.
- Other variables of interest – those being directly used by the analysis – must be checked for consistency. This involves checking plots of variables like the kinematic terms, the mass, geometric variables, fitting quality, etc. to ensure they match what is physically expected. If, for example, a p_T plot does not have a power-law shape, or if the pseudorapidity has anomalies in its shape (such as a majority of events in the higher values of $|\eta|$), then there is a problem with the Job Options or generators that must be resolved prior to official generation. For this analysis, the mass, p_T, pseudorapidity, and azimuthal angle are the primary data of interest; due to the need to reconstruct the mass of higher-level particles, p_x, p_y, p_z, and the energy E are also relevant.
- As a final consistency check, the mass of parent particles should be reconstructed from ones further down the decay chain, and checked. For example, in the $B_s \rightarrow J/\psi(\rightarrow \mu\mu)\varphi(\rightarrow \mu\mu)$ decay, the J/ψ and φ masses should be extracted from the Truth data and data reconstructed from the kinematics of the muons; the B_s mass

should then be reconstructed, both from the Truth data of the J/ψ and φ and from the data from the muons.

The number of photons can be checked by using a ROOT[20] macro designed to find the number of particles with a Particle Data Group[21] Identification Number (PDG ID; a standardized number scheme created by the PDG for Monte Carlo, to facilitate interfacing between different MC event generators, detector simulators, and analysis packages) of 22; the result of this check can be found in Figure 1. While there are no daughter photons in the $B_s \rightarrow J/\psi\varphi$ decay, this is not necessarily the case for other decays. Examining the mass plots of all the particles is sufficient to determine if there are inconsistencies in the masses of the particles between decay models; as the peaks of all the particles in question are consistent with their PDG values, it can be concluded that there was no inconsistency between PYTHIA8b (the ATLAS interface to PYTHIA8 dedicated to B-physics) and EvtGen.

Photons per Event

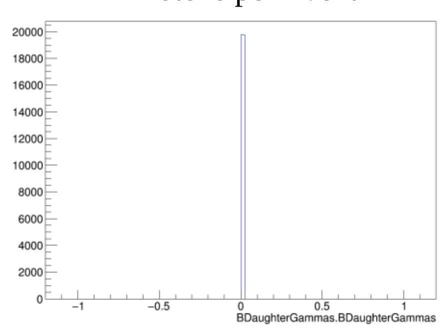

Figure 1: A plot showing the number of photons in the decay. Note that the x-axis is the number of photons in a given event; if a data point is at $x = 0$, that means that there were no photons radiated from the signal decay particles.

The data important to the analysis the MC is meant for must also be checked for consistency with known physics processes, for example anomalous bumps in the p_T spectrum far outside the main bulk of the data, which would indicate a problem in the generation. Most importantly – at least for this analysis – the mass must also be checked to ensure it peaks at its PDG value, and that the mass distribution itself follows the expected curve, which prior to simulation is a very narrow. An example is given in Figure 2, in which the four terms of a single muon from the Standard Model non-resonant dataset are shown. As can be seen, they are consistent with what we expect.

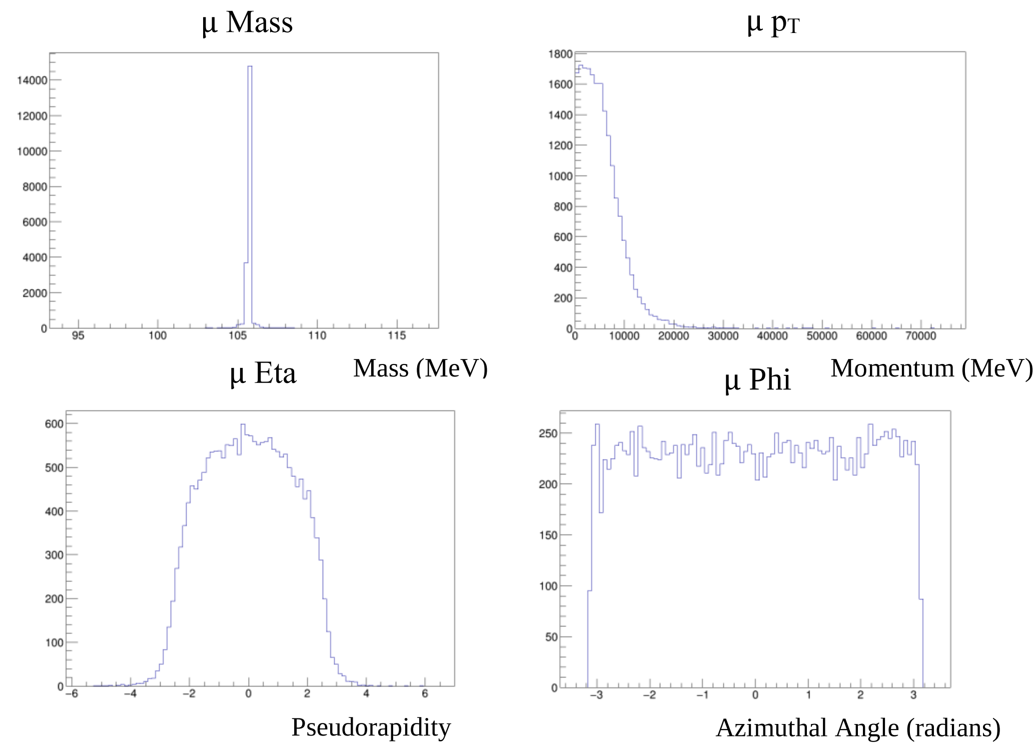

Figure 2: Truth information of simulated muon data: mass (upper left), transverse momentum (upper right), pseudorapidity (lower left), and azimuthal angle (lower right).

In collision data, unstable particles (such as B_s, J/ψ, and φ) must be reconstructed from their daughters, to ensure consistency. After validation, this reconstruction is performed using data from the simulated ATLAS detector, reconstructing masses from the momentum terms and energy deposited in the calorimeters. In a validation, it is necessary to extract these terms from the Truth, as the validation dataset has not gone through the simulation stage of Monte Carlo generation. For the purposes of this validation, the J/ψ and φ masses are reconstructed from the Truth kinematics and energy of their component muons, while the B_s mass is reconstructed from the reconstructed kinematics of the J/ψ and φ. The reconstructed mass can be calculated using the relativistic invariant mass formula, Equation 3. The reconstructed masses of J/ψ, φ, and B_s can be found in Figure 3. The narrow width of these distributions, a Breit-Wigner distribution corresponding to the particles' lifetime, is a consequence of the lack of detector simulation of the file, which results in little uncertainty in the mass. The position of the peak is the datum that is checked, and these are consistent with expectations.

Twenty thousand events of each background were generated, and then validated using the methods earlier described; example plots for the validation of the signal can be seen in Figure 4.

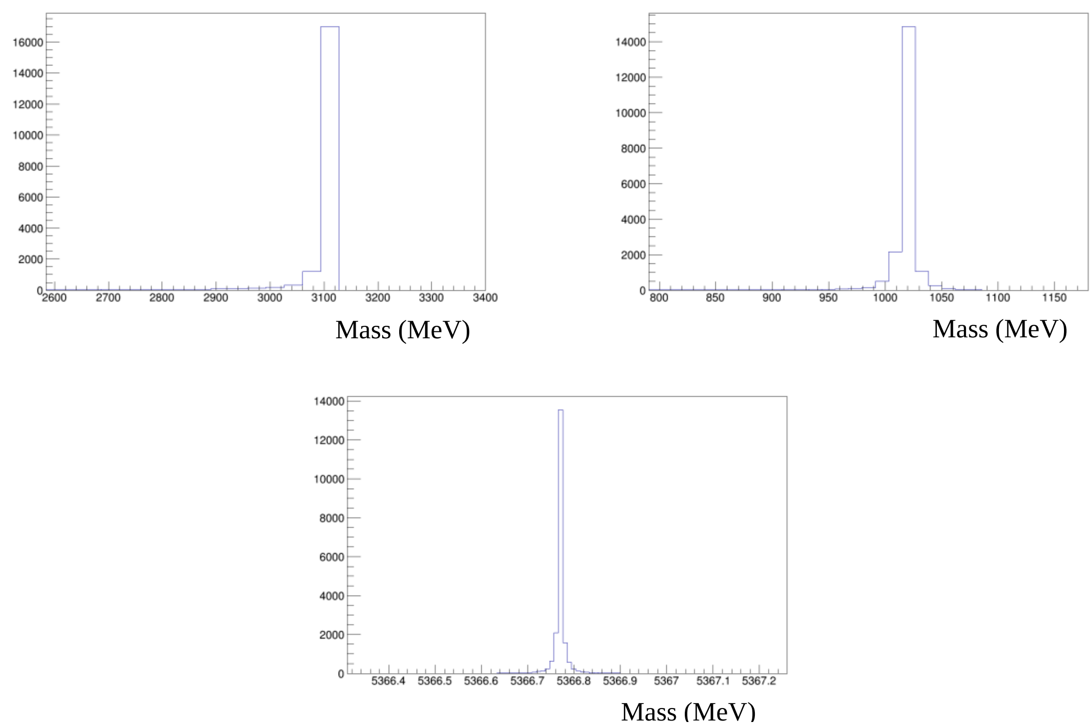

Figure 3: Reconstructed masses of the J/ψ (upper left), φ (upper right), and B_s (bottom) from their Truth daughter particles, from the $B_s \rightarrow J/\psi\varphi$ decay.

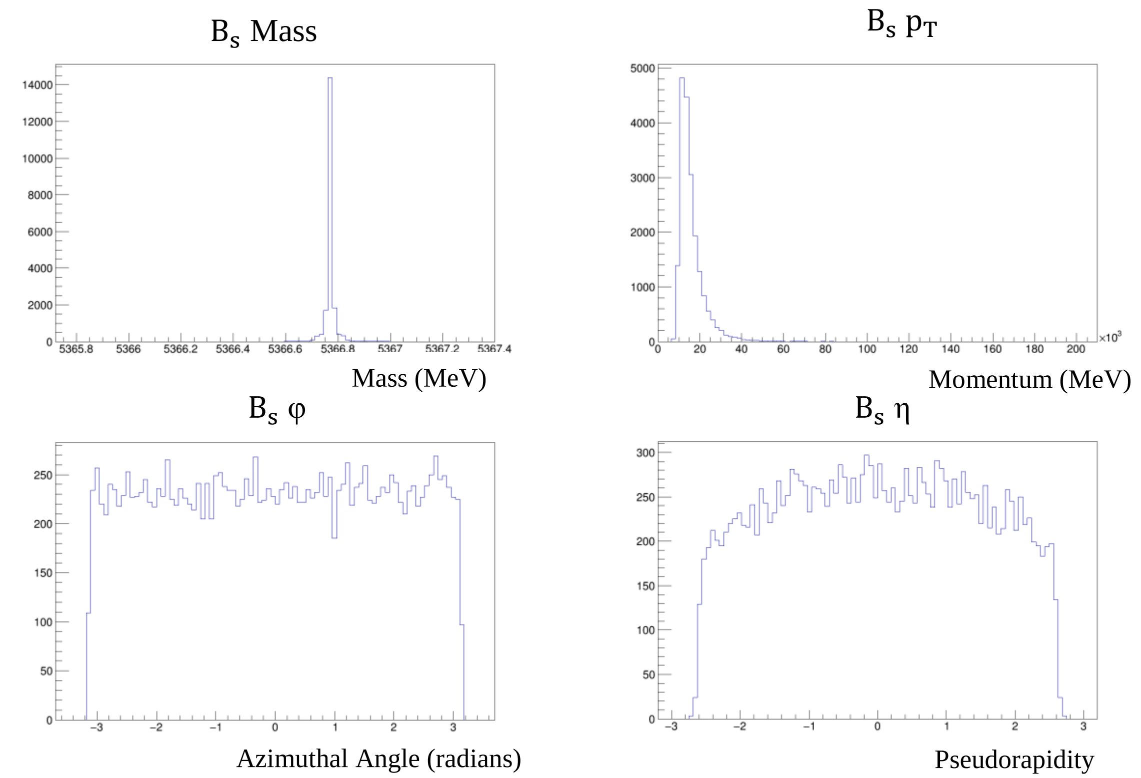

Figure 4: Generator-level validation plots for the Monte Carlo decay in the non-supersymmetric $B_s \rightarrow 4\mu$ channel, including the B_s mass (upper left), the B_s transverse momentum (upper right), the B_s azimuthal angle (lower left), and the B_s pseudorapidity (lower right).

5.6 Studying the Backgrounds

With the background samples simulated as described above, the next step is to determine how the backgrounds may be distinguished from the signal, and then reduced to the point that they are no longer a significant false contributor to the signal. To do this, the MC signal and backgrounds need to be compared on a single plot, where all the decays have been scaled to some reference channel. The resulting plot gives one a better idea of the effect of the peaking backgrounds on the signal. As suggested in section 5.4, the backgrounds and signal are scaled to the number of events in the reference MC file (the $B_s \rightarrow J/\psi\, \varphi$), given the branching ratios of each decay, and where applicable, the pion and kaon misidentification rate. Theory indicates that the branching ratio for the non-resonant SM $B_s \rightarrow 4\mu$ process lies between 1.3×10^{-10}[22] and 3.5×10^{-11}[23]. The full scaling factor F is:

$$F = \frac{(\#\ \text{reference events}) * \text{BR(decay)} * (\text{MisID})}{(\#\ \text{decay events}) * \text{BR(reference)}},$$

where "reference" refers to the $B_s \rightarrow J/\psi\,\varphi$ decay, and the MisID are the misidentification rates for pions and kaons, which are applied only for those backgrounds that have them. In the case of the B_d decays, the scaling factor is multiplied by an additional 3.9[24], to account for the fact that the LHC produces ~3.9 times more B_d than B_s. This scaling process was performed twice, at both extremes of the range $BR(B_s \rightarrow 4\mu) \in [3.5\times10^{-11}, 1.3\times10^{-10}]$. The result of this process can be found in Figure 5. The Monte Carlo used here is post-simulation and reconstruction. Note that each of these decays is a reconstructed four-daughter invariant mass; the muon mass was used for all four tracks in the invariant mass calculation, in order to properly simulate the misidentification of kaons and pions in the collider data.

From Figure 5, only two decays contribute significantly to the background, the $B_s \rightarrow J/\psi\,(\rightarrow \mu\mu)\varphi(\rightarrow \mu\mu)$ decay and the $B_d \rightarrow K^*(\rightarrow K^+\pi^-)\mu\mu$ decay. Of these two, the $B_s \rightarrow J/\psi\,\varphi$ is by far the greatest contributor of background events, nearly three orders of magnitude greater than the signal. The non-resonant $B_d \rightarrow K^+\pi^-\mu\mu$ and $B_s \rightarrow KK\mu\mu$ have not yet been studied, but may contribute significantly to the background. However, when the full analysis is done, a fit will be performed to the four-muon mass peak; it is expected that these backgrounds will not be peaking, and will thus be rejected at that stage.

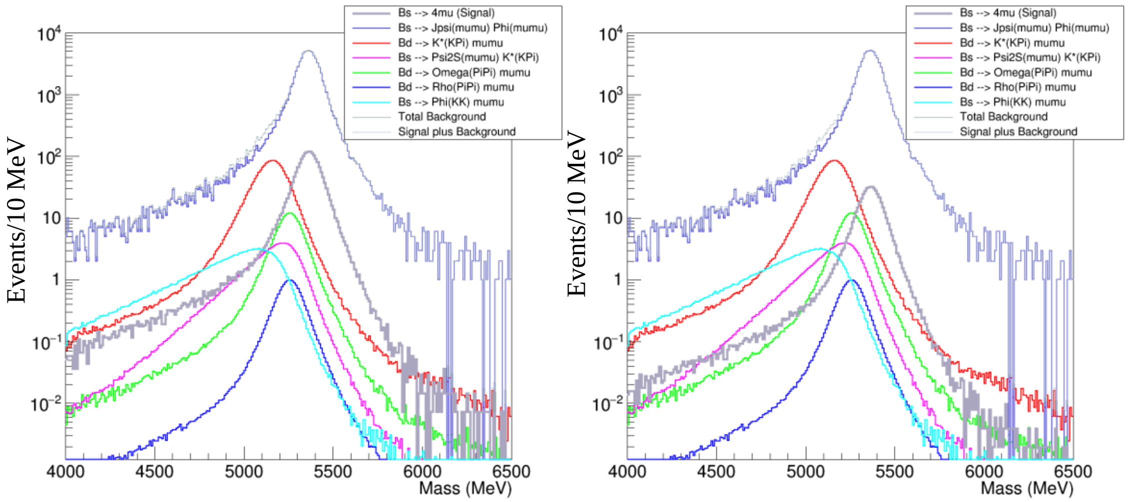

Figure 5: A logarithmic plot of the invariant mass of all the backgrounds and signal, scaled to the L_{int} of the $B_s \to J/\psi\, \varphi$ by th scaling factor in Table 3, for two predictions of the $B_s \to 4\mu$ branching ratio. The left is $BR(B_s \to 4\mu) = 1.3\times10^{-10}$, while the right is $BR(B_s \to 4\mu) = 3.5\times10^{-11}$. The $B_s \to J/\psi\,(\to \mu\mu)\ \varphi(\to \mu\mu)$ completely dominates, and is the primary contributor to both the "Total Background" (the sum of all the backgrounds) and "Signal plus Background" (Total Background plus the signal) lines. The long radiative tails are a consequence of the reconstruction of four-particle decays. No selection cuts have yet been applied other than the requirement that there are four muons, two of each charge.

The next step is to apply mass window cuts to the dimuon invariant mass centered around the PDG masses of the J/ψ and φ to reduce the $B_s \to J/\psi\, \varphi$ background. The size of the mass window here was 5σ, where σ is the standard deviation of a Gaussian function fitted to the mass spectrum of the meson. A 5σ window provides a suppression factor of $\sim 10^{-6}$, sufficient to remove it from the list of contributing backgrounds. The sigma for the J/ψ is 62.5 ± 1.02 MeV, while the sigma for the φ is 24.3 ± 0.217 MeV. Thus, 5σ covers ±312 and ±121.5 MeV, respectively. The mass window cuts around these values were applied to the daughters of the B_s, excluding any events whose reconstructed decay products were within the 5σ mass window. The result of this can be seen in Figure 6; the $B_s \to J/\psi\, \varphi$ background is effectively suppressed.

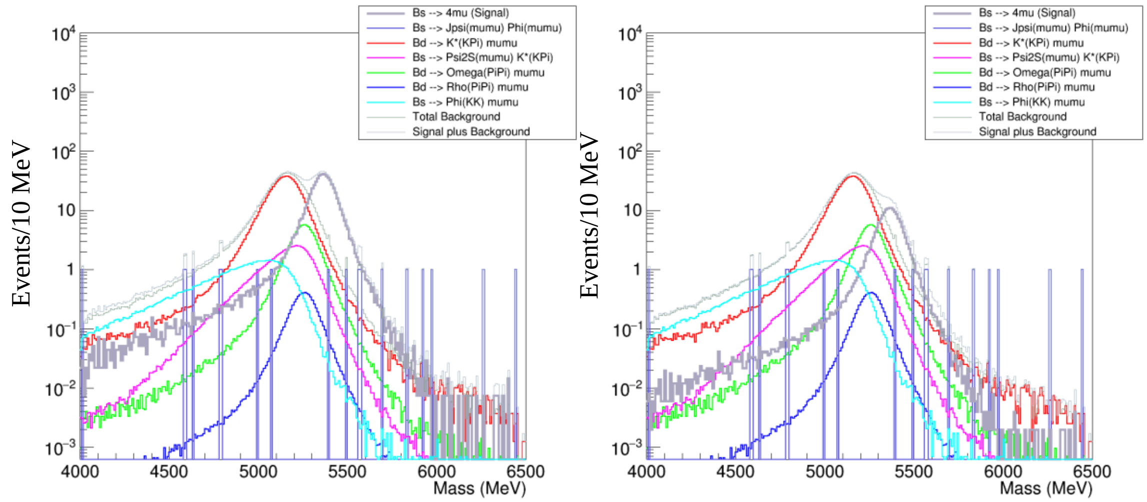

Figure 6: The same plots as in Figure 5, but with the J/ψ and φ mass window cuts applied. Note that the $B_s \to J/\psi\,\varphi$ decay has nearly vanished; the $B_d \to K^*\mu\mu$ decay is now the dominant background.

The next step is to reduce the background contribution from the $\mathrm{B_d} \to \mathrm{K}^*\mu\mu$, which from Figure 6 is now the greatest contributor to background. One way to reduce this background uses a mass window cut around the mass of the K^*. The fitted mass of the MC K^* events can be found in Figure 7. The fit made use of a probability distribution function (p.d.f.) made from the sum of a Gaussian and a Landau function. The characteristic function of the Landau distribution is:

$$L_c(\mathrm{x};\mu,\mathrm{c}) = \exp\left(\mathrm{i}\mathrm{x}\mu - |\mathrm{ct}|\left(1 + \frac{2\mathrm{i}}{\pi}\ln(|\mathrm{x}|)\right)\right),$$

where μ is the location parameter ("LocParam" in Figure 7), corresponding approximately to the curve's most probable value, and c is a scale parameter ("ScaleParam"), taking the place of the standard deviation. The p.d.f. of the Landau function, L(x), is given by the Fourier transform of its characteristic function $L_c(\mathrm{x};\mu,\mathrm{c})$. These two probability density functions are added together,

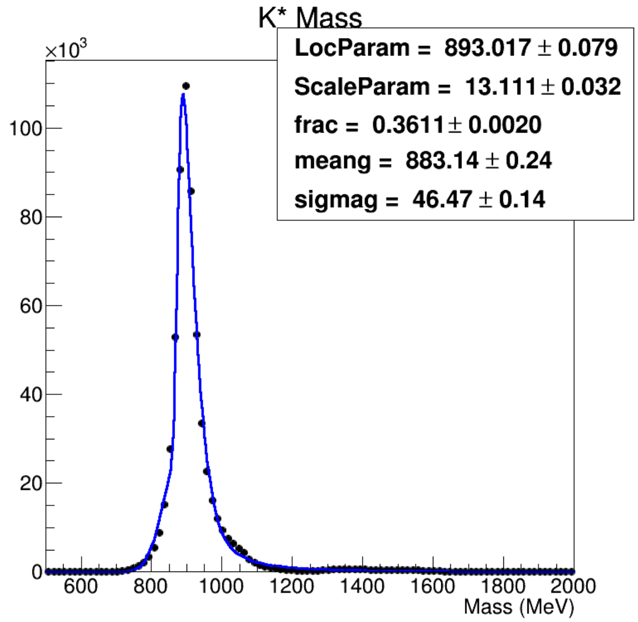

Figure 7: The fit of the K^* mass, drawing on events from the entire $B_d \to K^*\mu\mu$ Monte Carlo dataset. This fit uses a Gaussian plus a Landau function. The high-mass tail is thought to be caused by higher excited K^* states.

$$f(x) = (1 - K) \cdot G(x) + K \cdot L(x),$$

where G(x) is the Gaussian p.d.f., K is the scaling fraction (called "frac" in the legend of Figure 7), and x is the mass. The standard deviation σ here is the Gaussian σ, 46.47 ± 0.14 MeV, while 5σ is ±232.35 MeV. The contribution of the Landau is not large, as demonstrated by the relatively small value of K, and thus we can use the Gaussian mass window to define the rejection. The parameters of the fit can be found in Appendix A, Table 1. Applying this mass window cut resulted in a substantial reduction in the background, and a considerably smaller reduction in the signal. This 5σ K^* mass window cut preserved 58% of the signal, while only 3% of the background remained. The new comparison of the backgrounds can be found in Figure 8. This technique will not work for the non-resonant $B_d \to K^+\pi^-\mu\mu$ background; however, as discussed above this background will likely need to be reduced using a fit to the four-muon invariant mass.

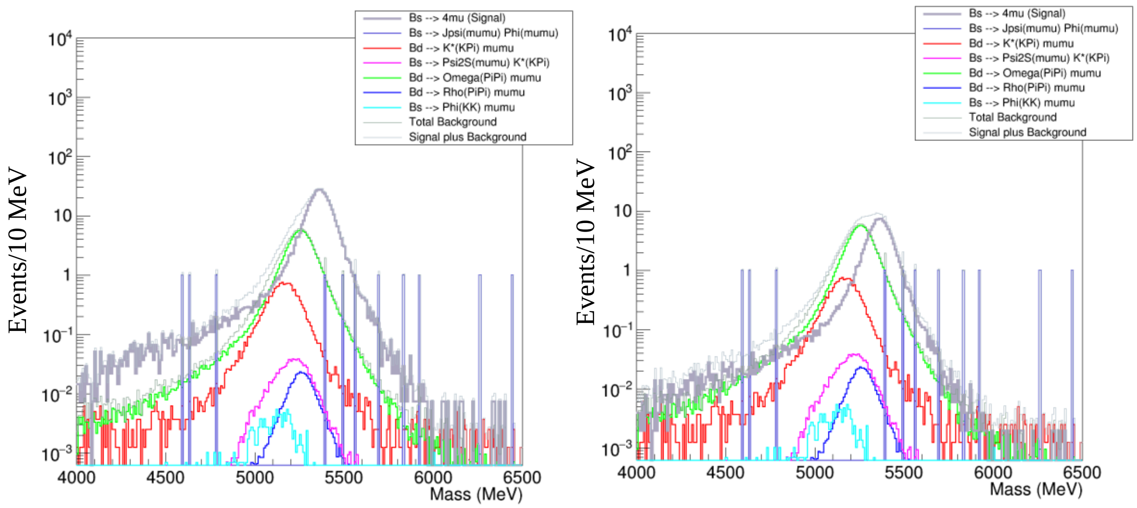

Figure 8: The same plots as in Figure 6, but with the K^* mass window cut applied. The $B_d \rightarrow K^*\mu\mu$ decay has been reduced significantly, to the point where it is no longer a significant contributor to the background.

Another way to reduce the background that doesn't involve applying selection criteria was explored. It involves finding the shape and the amplitude of the background (in this case $B_d \rightarrow K^*\mu\mu$) and the signal (the $B_s \rightarrow 4\mu$) in the Monte Carlo, and using this information to identify these particles' mass distributions in the collision data; once this is done, the background can be subtracted, leaving the signal. This is performed using reconstructed mass plots of the parent particles. By fitting the shapes of the mass curves of the B_s and B_d in the MC data, it is possible to estimate the background from the reconstructed mass plot of the collision data by applying those same fitting models to collision data. It is first necessary to reconstruct both signals from their final products, which in the case of the B_d decay is two muons, a kaon, and a pion, but with the kaon and pion misidentified as muons. The reconstructed mass of the B_d can be found in Figure 9, and the mass of the B_s in Figure 10. Both distributions were reconstructed from the

Monte Carlo datasets. We fit the mass curves using RooFit[25], ROOT's native curve-fitting code.

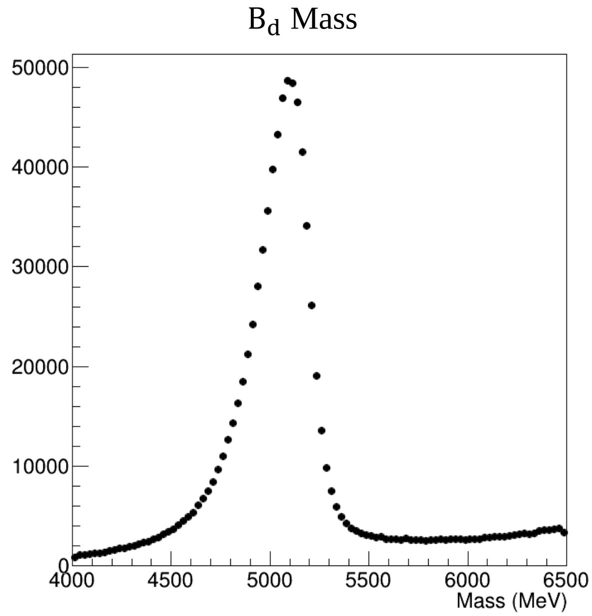

Figure 9: The mass of the B_d from the $B_d \rightarrow K^* \mu\mu$ decay. Note the Gaussian elbow on the right and the exponential decay on the left; this is characteristic of the Crystal Ball distribution. This was reconstructed using the four-muon track-mass hypothesis, which is the cause of the distortion of the B_d peak as opposed to the B_s in Figure 10. The rising tail on the right is a consequence of random combinatorics replacing other tracks in the event.

The shapes of both curves prevent a single function, such as a Gaussian or a Landau, from being fitted to them. To achieve a fit that converges, the range of each was split into three parts, the peak, and the left and right sidebands. The B_d mass range was split into the ranges 4000-4825 MeV, 4775-5325 MeV, and 5275-6500 MeV, and a separate fit was applied to each of these. The 50 MeV common range is to ensure the separate fits have a common point and a common slope at that point; reducing the ranges to 4000-4800 MeV, 4800-5300 MeV, and 5300-6500 MeV makes no difference in the quality of the fit. The B_d peak was fit using a sum of a Crystal Ball[26] function and a Gaussian (Figure 11). The former was used due to the Gaussian right side and power law

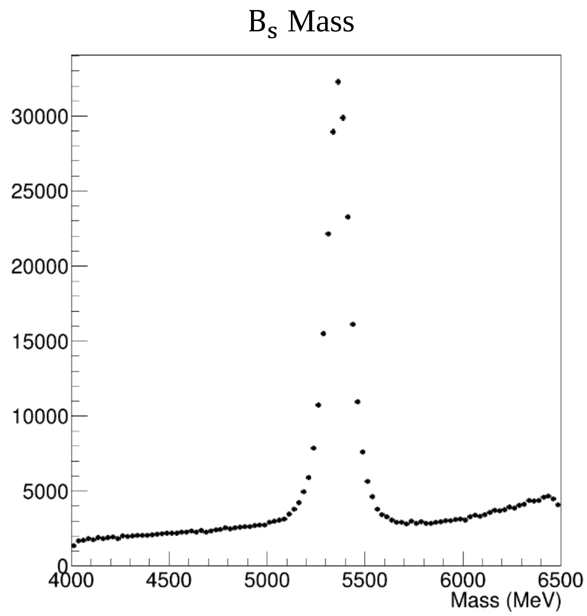

Figure 10: The mass of the B_s from the $B_s \rightarrow 4\mu$ signal decay.

left side of the peak; this function is usually used to describe the effect of radiative energy loss on invariant masses. The Crystal Ball function is defined as:

$$\mathrm{CB}(x) = \left.\frac{\left(\frac{n}{|a|}\right)^n e^{-\frac{1}{2}a^2}}{\left(\frac{n}{|a|} - |a| - x\right)^n}\right|_{x<-|a|}, \qquad \left. e^{\left(-\frac{1}{2}\left(\frac{x-m}{\sigma}\right)^2\right)}\right|_{x>-|a|},$$

where m (Gaussian mean), σ (Gaussian sigma), a, and n (values describing parameters of the power law) are free values for RooFit to range over when it tries to find a fit, and x is the input data (the mass of the particle). The PDFs for the peak are added together,

$$f(x) = \left(1 - P_{B_d}\right) \cdot \mathrm{CB}(x) + P_{B_d} \cdot G(x),$$

where CB(x) is the Crystal Ball function, G(x) is the Gaussian, and P_{B_d} is the scaling fraction. This fit has a χ^2/NDF of 1.97.

The left sideband was fit with three exponential functions added together,

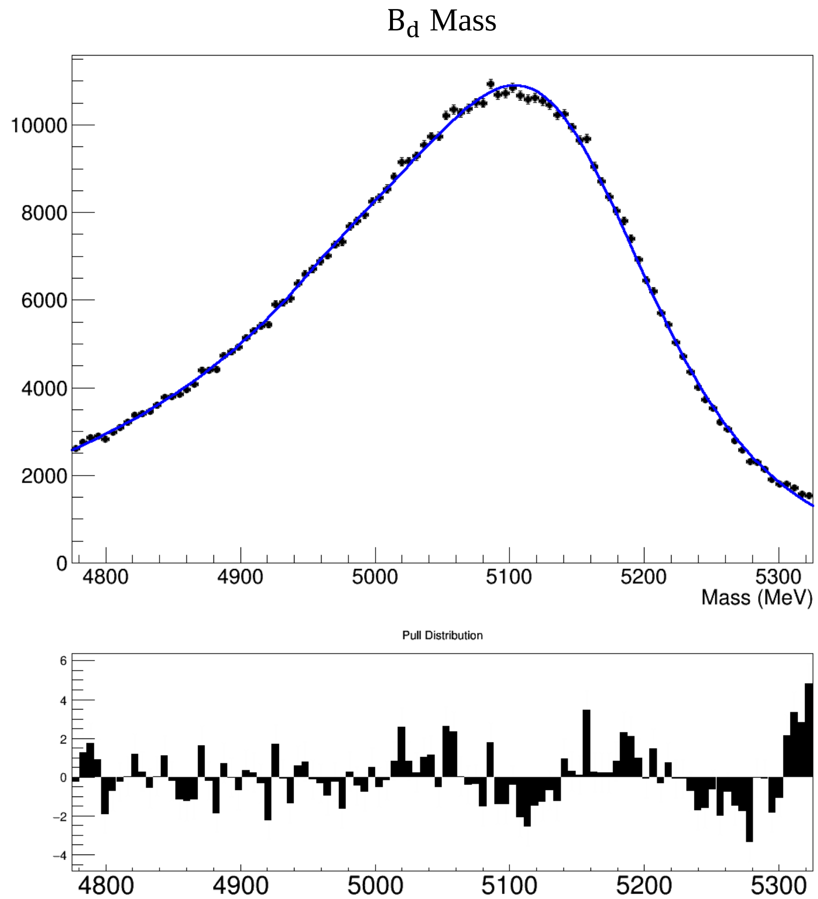

Figure 11: The peak of the mass curve of the B_d from the $B_d \rightarrow K^{*}\mu\mu$ decay. The bottom plot is a pull distribution, the deviation divided by the data bin's statistical uncertainty, which shows the degree to which the fit deviates from the data in standard deviations.

$$f(x) = \left(1 - L_{B_d,1}\right) \cdot E(ax) + L_{B_d,1} \cdot \left(\left(1 - L_{B_d,2}\right) \cdot E(bx) + L_{B_d,2} \cdot E(cx)\right),$$

where $L_{B_d,1}$ and $L_{B_d,2}$ are the scaling fractions, a, b, and c are the exponential coefficients, and E(nx) is the exponential function. The left sideband's fit has a χ^2/NDF of 0.862; this can be seen on Figure 12. The right sideband (Figure 13) was fit with a Gaussian and a third order polynomial added together, with a χ^2/NDF of 0.739:

$$f(x) = \left(1 - R_{B_d}\right) \cdot G(x) + R_{B_d} \cdot \mathrm{Pol}_2(x, a_1, a_2, a_3),$$

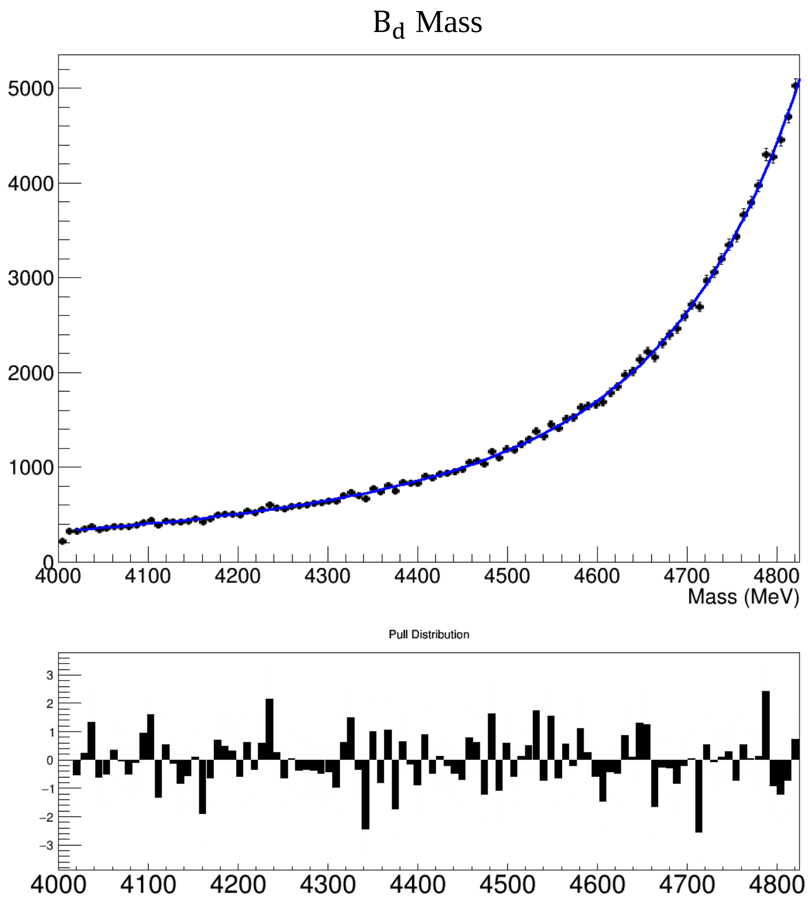

Figure 12: The left sideband of the mass curve of the B_d from the $B_d \rightarrow K^*\mu\mu$ decay.

where G(x) is the Gaussian, $\text{Pol}_2(x, a_1, a_2, a_3)$ is a second-order polynomial, a_3, a_2, and a_1 are the polynomial coefficients, and R_{B_d} is the scaling fraction. Then, these three fits were applied simultaneously to the full range, although the individual models were limited to their own respective ranges. This full fit can be found in Figure 14.

The same fitting process was applied to the B_s. The three ranges the fitting process was split into were 4000-5275 MeV, 5225-5500 MeV, and 5450-6500 MeV. The peak was fit with a Gaussian and a Breit-Wigner function (also known as the Cauchy-Lorentz distribution when in its non-relativistic form), added together. The Breit-Wigner distribution used by RooFit is defined as:

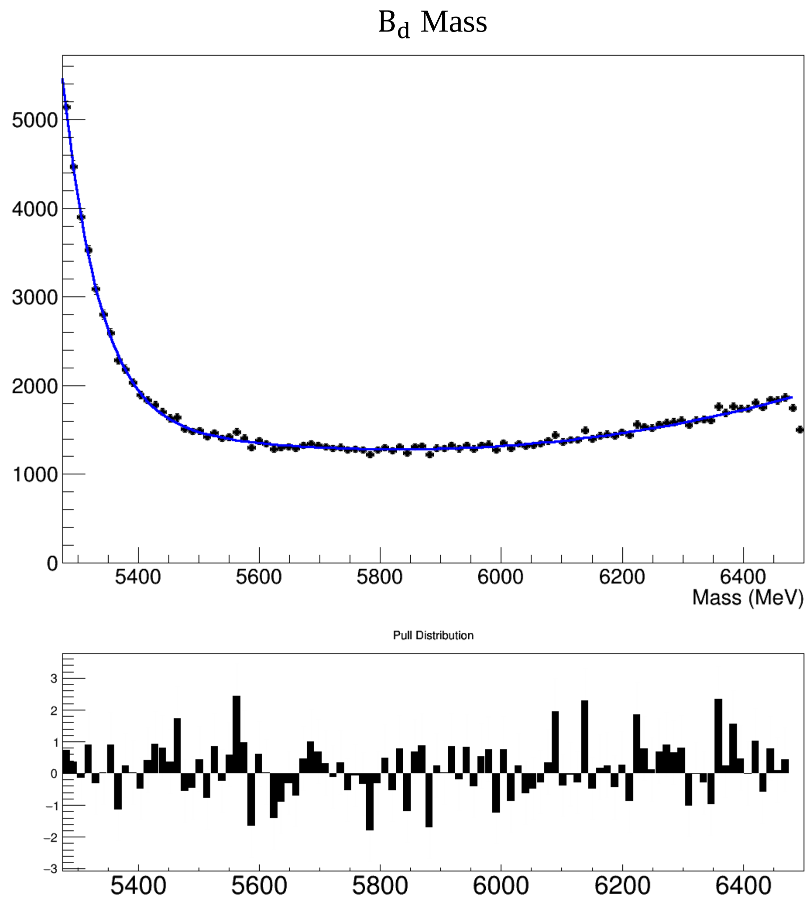

Figure 13: The right sideband of the mass curve of the B_d from the $B_d \to K^*\mu\mu$ decay.

$$\mathrm{BW(x)} = \frac{1}{(\mathrm{x}-\mathrm{m})^2 + \frac{1}{4}\mathrm{g}^2},$$

where m (Gaussian mean) and g (the half-width of the peak, related to the lifetime of the particle) are terms RooFit ranges over, and x is the input data. The two PDFs are added together,

$$\mathrm{f(x)} = \left(1 - \mathrm{P}_{\mathrm{B_s}}\right) \cdot \mathrm{BW(x)} + \mathrm{P}_{\mathrm{B_s}} \cdot \mathrm{G(x)},$$

where BW(x) is the Breit-Wigner function, G(x) is the Gaussian, and $\mathrm{P}_{\mathrm{B_s}}$ is the scaling fraction. The data fit the function with a χ^2/NDF of 1.19 (Figure 15). The left sideband

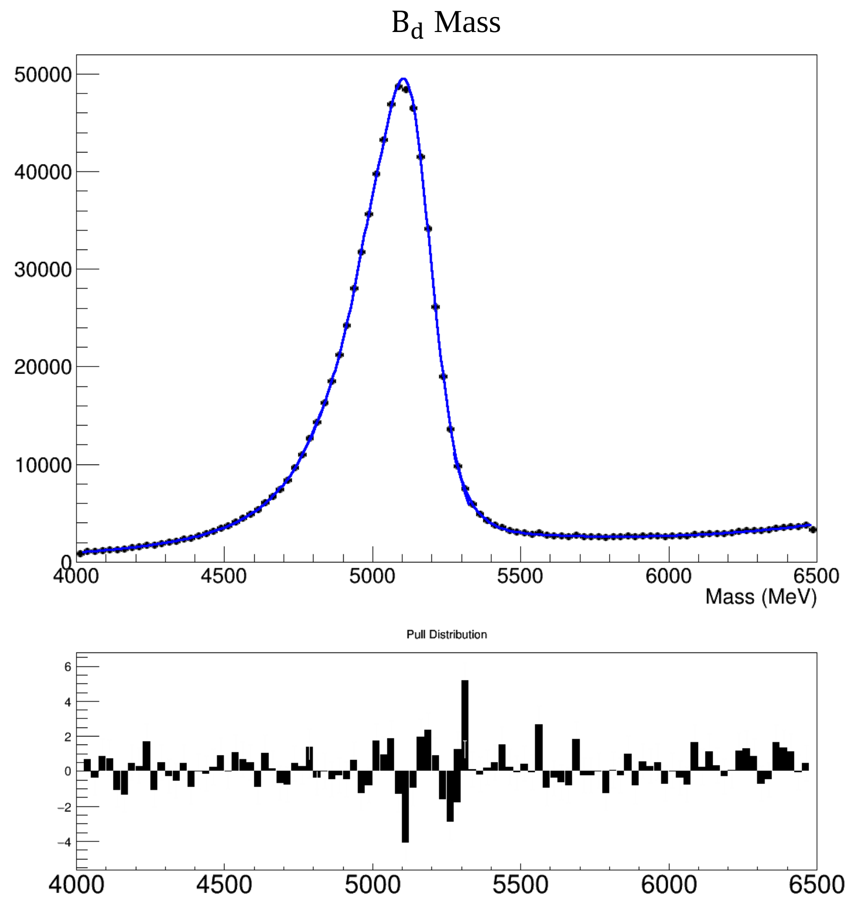

Figure 14: The full fit of the mass curve of the B_d from the $B_d \to K^*\mu\mu$ decay.

was fitted with a Gaussian added to a third order polynomial (Figure 16), and had a χ^2/NDF of 1.12:

$$f(x) = \left(1 - L_{B_s}\right) \cdot G(x) + L_{B_s} \cdot Pol_2(x, b_1, b_2, b_3),$$

where G(x) is the Gaussian, b_3, b_2, and b_1 are the polynomial coefficients, and L_{B_s} is the scaling fraction. The right sideband used a sum of a Gaussian, an exponential, and a third order polynomial,

$$f(x) = \left(1 - R_{B_s,1}\right) \cdot G(x) + R_{B_s,1} \cdot \left(\left(1 - R_{B_s,2}\right) \cdot E(dx) + R_{B_s,2} \cdot Pol_2(x, c_1, c_2, c_3)\right),$$

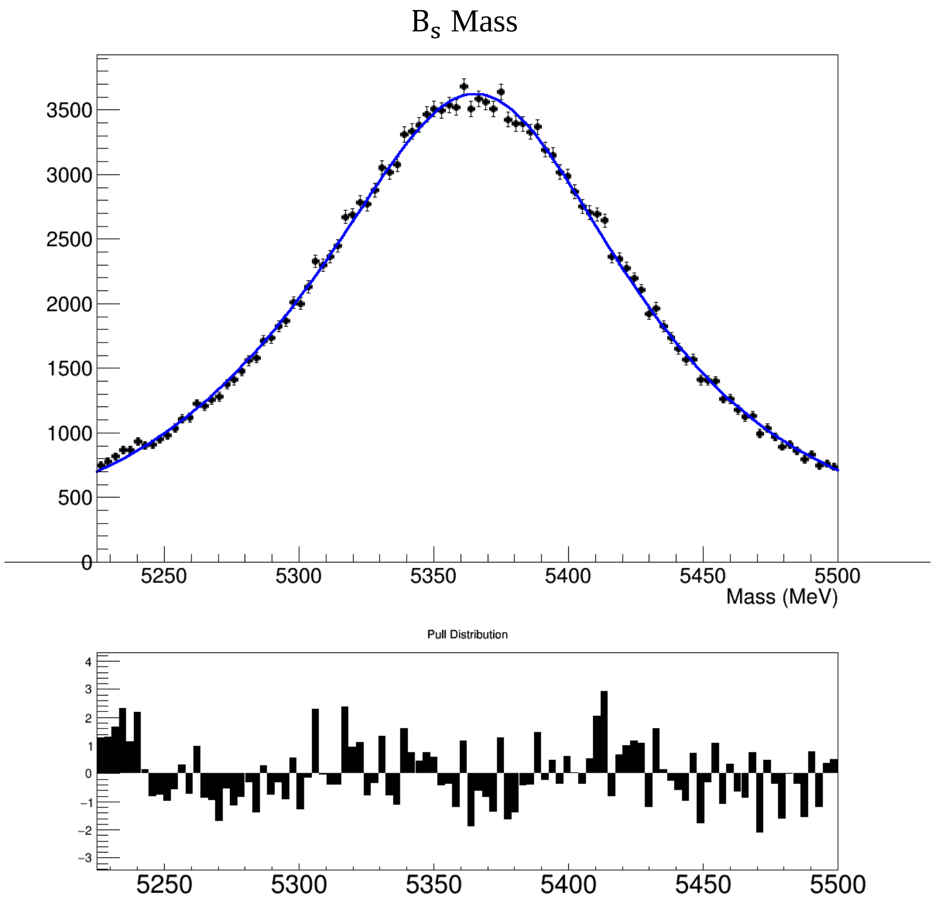

Figure 15: The fit of the peak of the mass curve of the B_s from the SM $B_s \rightarrow 4\mu$ decay.

where G(x) is the Gaussian PDF, d is the exponential coefficient, c_3, c_2, and c_1 are the polynomial coefficients and $R_{B_s,1}$ and $R_{B_s,2}$ are the scaling fractions. For this fit, $\chi^2/\mathrm{NDF} = 1.02$ (Figure 17). These three fits were then applied to the full range, as before with the three fit models constrained to their respective ranges (Figure 18). The detailed results of the fits to the data in Figures 11, 12, 13, 15, 16, and 17 can be found in Appendix A, Tables 2-7.

Once the fits have been applied, the $B_d \rightarrow K^*\mu\mu$ background can be subtracted from the data. These fits will also be used as part of the blinded analysis, when the signal region is obscured and the sidebands are studied. The sideband fits of the signal will be

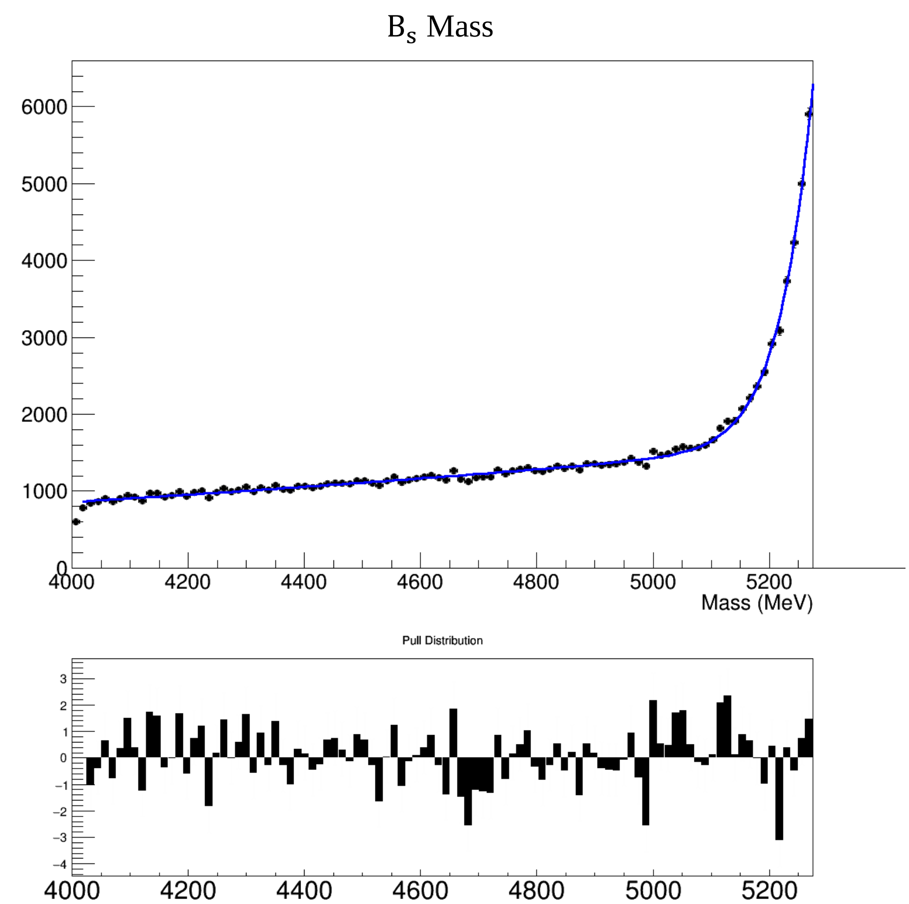

Figure 16: The fit of the left sideband of the mass curve of the B_s from the SM $B_s \rightarrow 4\mu$ decay.

used to model the signal in the collision data, and similarly the fit of the B_d will be used as a baseline model to identify and eliminate B_d background. This can be performed in RooFit, by applying different weights to the different datasets. Using this technique may save the 42% of signal that would be cut by the K^* mass cut.

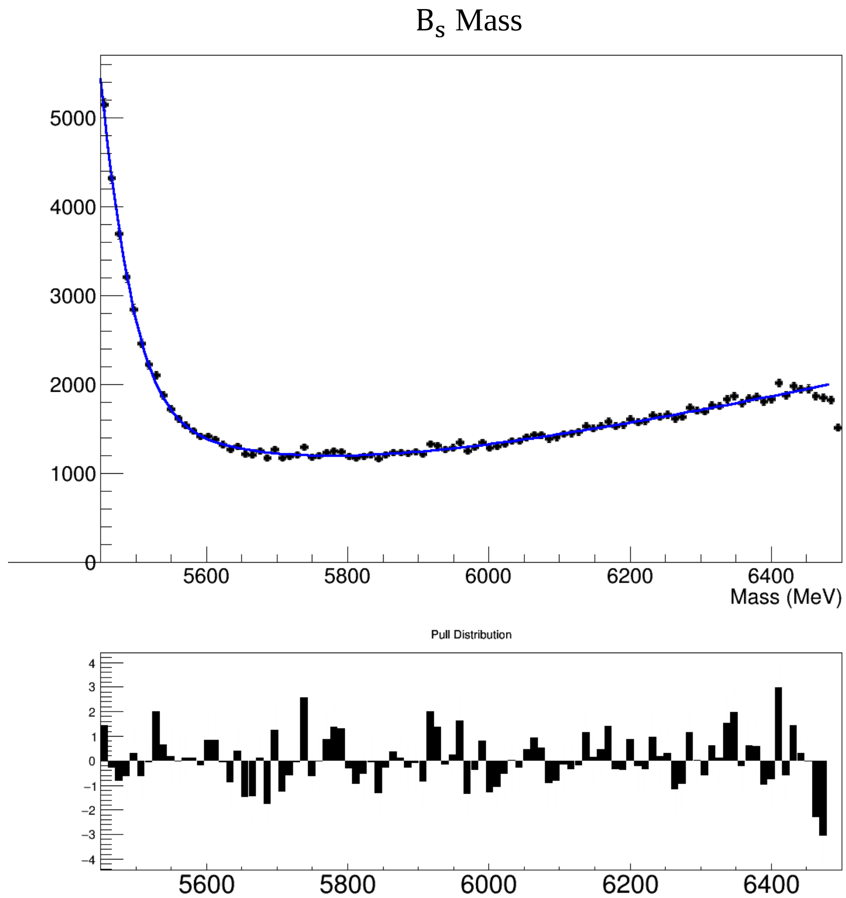

Figure 17: The fit of the right sideband of the mass curve of the B_s from the SM $B_s \rightarrow 4\mu$ decay.

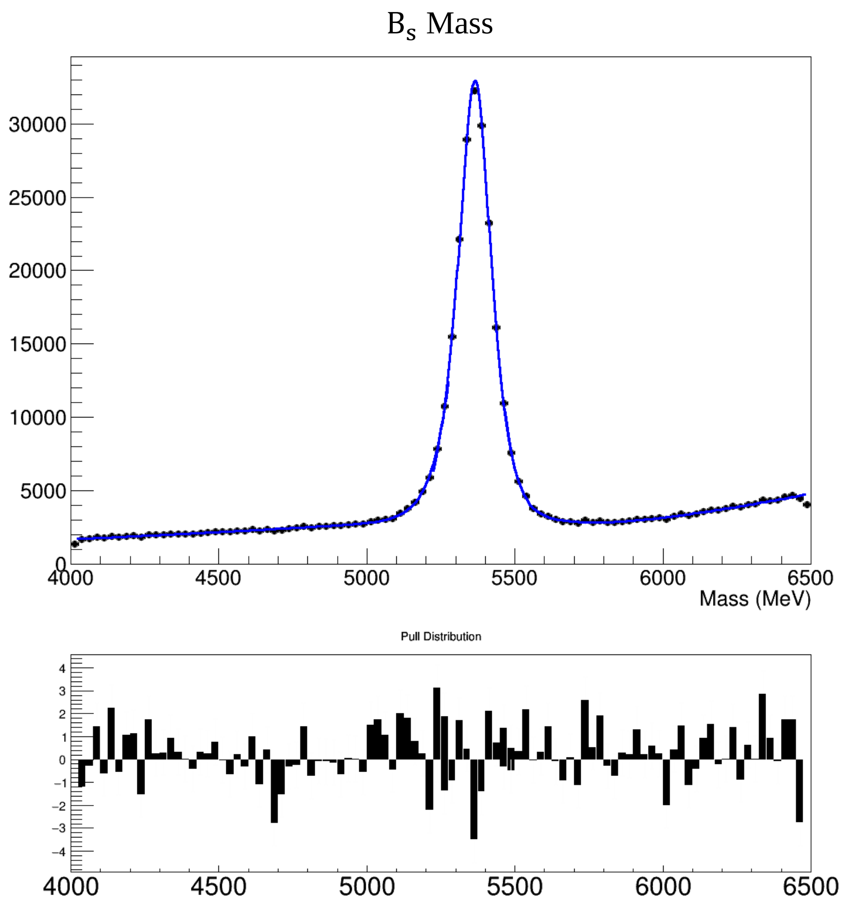

Figure 18: The full fit of the mass curve of the SM B_s from the $B_s \rightarrow 4\mu$ decay.

5.7 Conclusion and Outlook

The foundations for the study of the $B_s \rightarrow \mu^+\mu^-\mu^+\mu^-$ decay to seek physics beyond the Standard Model have been presented. Several triggers have been studied and selected for the analysis. The Monte Carlo event sample of most of the backgrounds have been generated. These backgrounds have been compared to the signal. The two dominant backgrounds, the resonant $B_s \rightarrow J/\psi\,(\rightarrow \mu\mu)\varphi(\rightarrow \mu\mu)$ decay and the $B_d \rightarrow K^*(\rightarrow K^+\pi^-)\mu\mu$, have been reduced. The first was suppressed by a factor of ~10^6 by applying mass window cuts to the dimuon signal around the invariant mass of the J/ψ and φ, removing any events with an intermediate particle within those mass ranges. The second was suppressed in a similar way, by a factor of ~100, by applying a mass window cut to the dihadron around the K^*'s invariant mass. A second technique, involving fitting the invariant masses of the B_s and B_d, was also presented. These fits will also be used to analyze the sidebands of the collision data during the blinded analysis. Together, these cuts have substantially reduced the presented backgrounds as false contributors to the signal by a factor of ~1000.

Several steps remain to be taken before analysis of collision data can begin. If it is to be used in the analysis of the collision data, the fitting procedure should be performed on a version of the B_d mass peak where the misidentification of the pion and kaon has been considered, as this may change the shape of the invariant mass peak and by extension change its fit. The non-resonant $B_d \rightarrow K^+\pi^-\mu\mu$ and $B_s \rightarrow KK\mu\mu$ decays will contribute to the background similarly to the $B_d \rightarrow K^*\mu\mu$ decay, but they are not well-measured and thus are not included in this study; the full analysis will need to measure them. Analysis of combinatorics should be explored in the MC; it is possible, in the ATLAS detector, for muons, pions, or kaons from other simultaneous proton-proton collisions ("pile-up") to accidentally create a fake $B_s \rightarrow 4\mu$ signal. Background from non-b-decays producing daughters that mimic the signal, such as $J/\psi \rightarrow \mu\mu$, should similarly be explored. MC will need to be studied to quantify these as backgrounds. The final series of selection criteria for the analysis will be developed by a boosted decision tree neural network algorithm, which should also serve to reduce the $B_d \rightarrow \omega\ \mu\mu$ background. Once this is done, the analysis on collision data may begin.

5.8 References

1. Aaij, R. (LHCb Collaboration) (2013). Search for rare $B^0_{(s)} \rightarrow \mu^+\mu^-\mu^+\mu^-$ Decays. Phys. Rev. Lett. 110, 211801.
2. CMS and LHCb Collaborations (2015). Observation of the rare $B_s \rightarrow \mu^+\mu^+$ decay from the combined analysis of CMS and LHCb data. Nature 522, 68-72.
3. Provided by Konstantin Toms. Private communication, 2016.
4. ATLAS Collaboration (2013). Flavor tagged time dependent angular analysis of the $B_s \rightarrow J/\psi\varphi$ decay and extraction of $\Delta\Gamma$ and the weak phase φ_s in ATLAS. ATLAS-CONF-2013-039.
5. LHCb Collaboration (2012). Tagged time-dependent angular analysis of $B_s \rightarrow J/\psi\varphi$ decays at LHCb. LHCb-CONF-2012-002.
6. ATLAS Collaboration (2013). ATLAS B-physics studies at increased LHC luminosity, potential for CP-violation measurement in the $B_s \rightarrow J/\psi\varphi$ decay. ATL-PHYS-PUB-2013-010.
7. LHCb Collaboration (2013). Production of J/psi and Upsilon mesons in pp collisions at $\sqrt{s} = 8$ TeV. LHCb-PAPER-2013-016.
8. ATLAS Collaboration (2016). Study of the rare decays of B^0_s and B^0 into muon pairs from data collected during the LHC Run 1 with the ATLAS detector. Eur. Phys. J. C76, 513.
9. ATLAS Collaboration (2016). Measurement of the CP-violating phase ϕ_s and the B^0_s meson decay width difference with $B^0_s \rightarrow J/\psi\ \phi$ decays in ATLAS. JHEP 1608, 147.

10. LHCb Collaboration (2014). Precision measurement of *CP* violation in $B_s^0 \to J/\psi K^+ K^-$ decays. Phys. Rev. Lett. 114 no.4, 041801.

11. Bityukov, S. I. (1998). Towards the observation of signal over background in future experiments. INR-0945A-98.

12. Simioni, Edward, et al. (2014). The Topological Processor for the future ATLAS Level-1 Trigger: from design to commissioning. arXiv:1406.4316.

13. ATLAS Collaboration (2013). Measurement of the differential cross-section of B^+ meson production in pp collisions at $\sqrt{s}$ = 7 TeV at ATLAS. JHEP 1310, 042.

14. LHCb Collaboration (2013). Measurement of B meson production cross-sections in proton-proton collisions at $\sqrt{s}$ = 7 TeV. JHEP 1308, 117.

15. LHCb Collaboration (2013). Production of J/psi and Upsilon mesons in pp collisions at $\sqrt{s} = 8$ TeV. JHEP 1306, 064.

16. Ryd, Anders, et al (2005). EvtGen: A Monte Carlo Generator for B-Physics. EVTGEN-V00-11-07.

17. Davidson, N., Przedzinski, T., and Was, Z. (2010). PHOTOS Interface in C++; Technical and Physics Documentation. Comput. Phys. Commun. 199, 86-101.

18. Sjöstrand, T., Mrenna, S., and Skands, P. (2008). A Brief Introduction to PYTHIA 8.1. Comput. Phys. Comm. 178, 852-867.

19. Lange, D. J. (2001). The EvtGen particle decay simulation package. Nucl. Instrum. Meth. A462, 152-155.

20. Brun, R., and Rademakers, F. (1997). ROOT: An object oriented data analysis framework. Nucl. Instrum. Meth. A389, 81-86.

21. http://www-pdg.lbl.gov/

22. Melikhov, Dmitri, and Nikitin, Nikolai (2004). Rare radiative leptonic decays $B_{d,s} \to l^+l^-\gamma$. PRD 70, 114028.

23. Dincer, Yusuf, and Sehgal, L. M. (2003). Electroweak effects in the double Dalitz decay $B_s \to l^+l^-l^+l^-$. Physics Letters B 556, 169–176.

24. http://www.slac.stanford.edu/xorg/hfag/osc/summer_2016/#FRAC

25. Verkerke, Wouter, and Kirkby, David (2003). The RooFit toolkit for data modeling. CHEP-2003-MOLT007.

26. Skwarnicki, T. (1986). A Study of the Radiative Cascade Transitions Between the Upsilon-Prime and Upsilon Resonances. Ph.D. Thesis, Institute of Nuclear Physics, Krakow, Poland.

Chapter 6: Development of Triggers for Future New Physics Searches

6.1 Introduction

In 2012, the ATLAS experiment generated about 25 Mb of data per collision, or about a petabyte per second, although only a fraction of this was stored. The ATLAS experiment collects data through its numerous triggers, hardware and software systems designed to use various criteria to rapidly select events for the detector to record. These triggers are meant to pass events of interest, while rejecting unwanted data. In the 2012 LHC, after data had passed through all triggers, the data rate was reduced from ~1 Pb/sec to ~100 Mb/sec. The center-of-mass energy of the LHC was increased from 8 TeV to 13 TeV in 2015, which resulted in a substantially increased the pile-up. In total, the instantaneous luminosity increased from $\sim 4\times 10^{33}$ cm^{-2} s^{-1} to 10^{34} cm^{-2} s^{-1}, and later upgrades will increase it further. Upgrades will also increase the number of interactions per event crossing (the pileup). This will increase the data generated by ATLAS significantly, and so steps must be taken to increase the efficiency for which desired data are accepted, and unwanted rejected.

A sub-trigger of the ATLAS high-level triggering system is the B-Physics Trigger, or B-Trigger. About 1% of collisions in the LHC produce a $b\bar{b}$ pair[1]. As a consequence, for the analysis of B-physics, a trigger can be used that is especially selective for b-quark production. There are two strategies[2] used for triggering on B-decays:

- Region of Interest (RoI) guided: The Level-1 trigger detects a muon and creates RoI's (regions in the Calorimeter and Muon Spectrometer where track and energy deposition patterns indicate possible objects of interest) to be passed to Level-2; the Level-2 trigger validates the muon, and the L2 and EF triggers reconstruct tracks in jet and EM RoI's, selecting J/ψ and B-mesons for storage.
- Full scan: The Level-1 trigger detects a muon and creates RoI's to be passed to Level-2; the Level-2 trigger validates the muon, and then reconstructs the tracks with the full acceptance of the SCT and Pixel Detector, selecting B-mesons in the process (the J/ψ reconstruction requires additional resources for the Transition Radiation Tracker scan); finally, the EF performs a full scan or uses L2 tracks to form the RoI.

In ATLAS, many individual triggers make up the overall B-Trigger. Many of the B-Triggers fire primarily on dimuon events, such as those from $B \rightarrow \mu^+\mu^-$, $\Upsilon \rightarrow \mu^+\mu^-$, and especially $J/\psi \rightarrow \mu^+\mu^-$. This triggering begins when two muons are detected in the Level-1 trigger, creating an RoI that is then passed up to the High-Level Trigger. In the HLT, the muon and vertex fits are confirmed; selection is then based on vertex quality and invariant mass criteria in the HLT. There are additionally more complicated triggers used in B-physics, such as those selecting hadronic tracks, as in the decay $B_d \rightarrow J/\psi\,(\mu^+\mu^-)\,K^*(K^+\pi^-)$.

A project was undertaken to optimize the set of B-Triggers utilizing a $J/\psi \rightarrow \mu\mu$ decay, to increase the fraction of events of interest passed to the computing system. One of the possible ways to do this involves tightening selection on the dimuon vertex quality. However, the tracking and vertexing quality at the HLT is inferior to that in the offline analysis, a fact that needs be considered to avoid biasing the offline analyses. This project is presented here.

6.2 J/ψ Decay Vertex-Fit Quality Optimization Studies

Events involving a heavy quark frequently produce a J/ψ meson in their decay. In ~10% of J/ψ decays, the meson decays into a muon pair[3], which produces a clean signal for the trigger. The decay $J/\psi \rightarrow \mu^{+}\mu^{-}$ is reconstructed from two oppositely charged muon tracks, fitted to a common vertex, with high efficiency. The quality of the reconstruction is characterized by a χ^2 figure of merit. In ATLAS, the χ^2 of the decay vertex for a particle reconstructed from its daughters is defined as

$$\chi^2 = \sum_i \Delta\mathbf{q}_i^T W_i \Delta\mathbf{q}_i = \sum_{i=1}^{N_{tracks}} \left(\mathbf{q}_i - \mathbf{T}(\vec{V}, \vec{p}_i)\right)^T W_i \left(\mathbf{q}_i - \mathbf{T}(\vec{V}, \vec{p}_i)\right).$$

Here $\Delta\mathbf{q}_i$ are the trajectory parameters, functions of the vertex position and the track momenta: $\mathbf{q}_i$ is a particle perigee trajectory parameterization for a 3D curved track in a magnetic field, and $\mathbf{q}_i' = \mathbf{T}(\vec{V}, \vec{p}_i)$ is the trajectory parameter given the value $\vec{V}$ of the particle origin vertex and the $\vec{p}_i$ of the particle momentum at this vertex. The vertex $\vec{V}$ is that found to be the most likely point of origin of the N tracks. No mass constraint was applied when the vertex $\vec{V}$ was determined. W_i is the weight matrix associated with the measurement uncertainties of track i. See [4], [5], and [6] for more details on this equation.

A part of refining the High-Level Trigger involves optimizing the J/ψ vertex χ^2 selection criteria. More specifically, the variable examined is χ^2/NDF; the number of degrees of freedom (NDF) is related to the number of tracks that are being vertex-fitted.

For the dimuon, the number of degrees of freedom in the reconstruction of the χ^2 is one. Events in the datasets used for the physics analysis of this dissertation are accepted or rejected on the basis of a selection requirement placed on the value of the χ^2. This cut occurs in the High-Level Trigger, where all events with a J/ψ χ^2 above 20 are rejected. Reducing the data stored, using both this cut and others, is necessary to the efficient storage of ATLAS data as instantaneous luminosity and event rate increase.

6.3 Optimizing the High-Level Trigger for Selection of Events Involving a B-Meson and Two Muons

B-physics makes use of several triggers that activate on different dimuon decays; these include triggers for the decay modes $B \rightarrow \mu^+\mu^-$, $B \rightarrow \mu^+\mu^-$ X, and $B \rightarrow J/\psi(\mu^+\mu^-)$ X, for some decay product X. This optimization focuses on the vertex fit (the χ^2) of a high-level B-trigger called 2mu4_Jpsimumu, a trigger designed to detect and analyze decays involving a B-meson decaying to a J/ψ, itself decaying to a dimuon. The "2muX" part of the trigger's name indicates that it can trigger on a dimuon where each muon has a p_T of X or higher. High-level triggers in ATLAS have access to momentum, position, pseudorapidity, and azimuthal angle for the muon and hadron tracks; they combine muon candidates from the Muon Spectrometer with tracks from the Inner Detector, determine whether or not they come from a vertex in the ID (using the vertex selection criterion, the χ^2 cut), and then check if the reconstructed pair's invariant mass is in the mass window of the J/ψ (2500 – 4300 MeV). If it is, and if the vertex is of sufficient quality – if the χ^2 value is below the selection criterion for that particle – the event is stored. Because in B-physics events, the majority of muon pairs come from $B \rightarrow J/\psi$ $(\mu^+\mu^-)$ X, this study focuses primarily on the figure of merit for the reconstruction of a vertex, i.e. the χ^2 of the J/ψ vertex, with a lesser focus on the χ^2 of the vertex of B-meson decays. The optimization process made use of both High-Level Trigger and offline-reconstructed data. Matching between muons reconstructed at the HLT stage and during the offline reconstruction was performed using a minimum ΔR technique, where $\Delta R \equiv \sqrt{(\varphi_{HLT} - \varphi_{offline})^2 + (\eta_{HLT} - \eta_{offline})^2}$, to ensure the same muon was analyzed.

This optimization analysis was performed twice, on two different sets of data. Run-1 signal Monte Carlo data were used to establish the basic method. This first analysis used Run-1 Monte Carlo data and ATLAS Offline software ("code"). The second, full analysis of signal versus background was then applied to Run-2 events. This used Run-2 Monte Carlo data and code. There were significant differences in the paradigms of Run-1 and Run-2, both in the form of the code they used and the structure of their datasets, and as a consequence separate analysis programs had to be written for both. While there were some differences in both the process of the analysis and in what was analyzed, the core of the optimization process remains the same. The optimizations for Run-1 and Run-2 used different Monte Carlo event types for their analysis. The Run-1 analysis made use of a $B_s \rightarrow J/\psi\ (\mu\mu)\varphi$ dataset, while the Run-2 analysis made use of both a $b\bar{b} \rightarrow J/\psi\ (\mu\mu)X$ dataset for the signal, and a $b\bar{b} \rightarrow \mu^+\mu^- X$ dataset for the background. These two datasets were used because most B-trigger-reliant analyses make use of the $J/\psi \rightarrow \mu^+\mu^-$ signal for identification. A background dataset was not used for the Run-1 data.

Optimizing the vertex fit χ^2 selection criteria involves a study of Monte Carlo data, and has three parts. The first part involves creating two-dimensional correlation plots between the J/ψ χ^2 and the other reconstructed properties of the J/ψ (the momentum terms p_x, p_y, p_z, the transverse momentum $p_T \equiv \sqrt{p_x^2 + p_y^2}$, the mass, the pseudorapidity η, the azimuthal angle φ, the number of degrees of freedom of the fit, the mean transverse decay length L_{xy}, and the vertex positions x, y, and z) for the EF and L2 triggers. This is in order to study the relationship between the vertexing and data such as the momenta. If correlation had been discovered, it would have required performing offline analyses to determine the consequences of applying the new cut before applying new selection criteria to the χ^2. Correlation studies also may reveal bugs in the reconstruction and vertexing. The second part requires the study of EF and L2 χ^2 plots, to examine the effects of new selection criteria upon the number of events, both for the signal dataset and the background. The final part is the creation of signal efficiency plots, background rejection plots, and Receiver Operating Characteristic (ROC) plots, which are plots of signal efficiency vs. background rejection. The Run-1 analysis did not apply the final two steps; only the signal efficiency was studied for Run-1.

In addition to the absolute J/ψ χ^2, correlations are examined between the χ^2 difference and all the other terms. The χ^2 difference is defined as $\chi^2_{HLT} - \chi^2_{Offline}$, between the J/ψ χ^2 as determined by the High-Level Triggers and by the offline reconstruction. The HLT tracking and offline tracking are slightly different, with the HLT tracking being of lower quality, admitting poorer vertex fits. The difference was thus examined in part to check for significant irregularities between the HLT and offline vertexing data, but primarily to see if the ordinary differences between the HLT and offline vertexing were correlated with other aspects of the data. The normalized J/ψ χ^2 is also compared with all other J/ψ characteristics, along with the normalized χ^2 difference.

These normalized plots are created when each χ^2 "slice" in the 2D plot is normalized to a common maximum, which is the highest value of χ^2 in the slice. These are created for the same reason as comparing the unnormalized χ^2, as some structures are more visible in a normalized plot than an unnormalized one. The sort of correlation we look for are structures like a high density (~2 times the number of events compared to the surrounding region) of events clustered around a diagonal line in a linear graph; uncorrelated event density clusters on these 2D plots are horizontal or vertical, depending on the particular data type. Another type of correlation is apparent as a "bump," a region of a distribution of much higher density (~3 times the surrounding region). These spots can imply some unusual dependence at a threshold value, or a bug in the code. Some correlation between χ^2 and p_z was observed in the form of a small peak at EF $p_z = 0$ (Figure 1) in both Run-1 and Run-2 data, but this correlation was not sufficiently large to motivate any new cuts or studies. No other significant correlations were found.

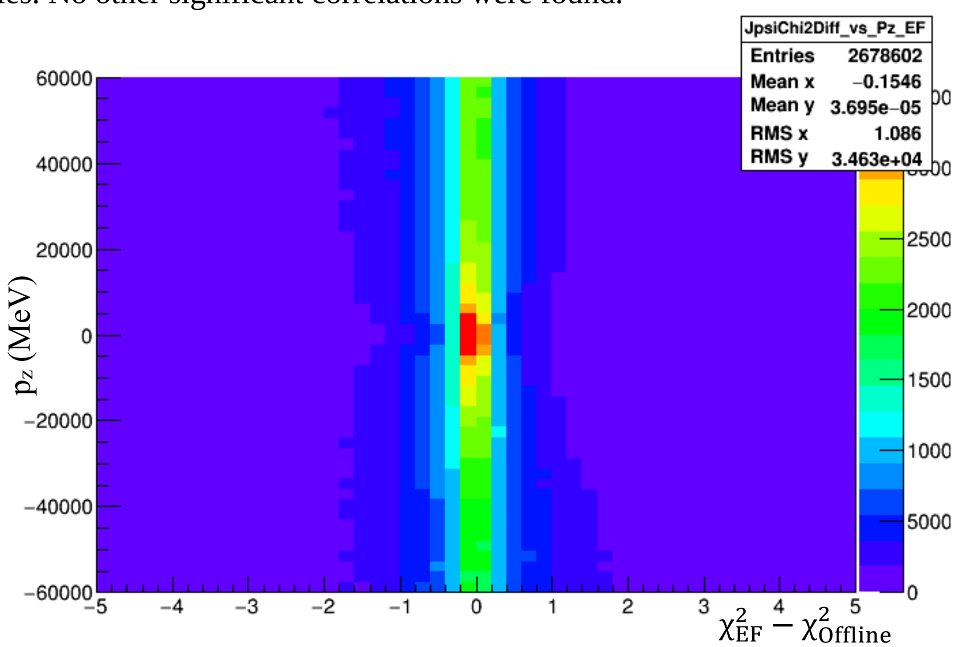

Figure 1: The correlation between the normalized J/ψ χ^2difference and the J/ψ p_z, prominent around $p_z = 0$, for Run-1 MC $B_s \rightarrow J/\psi\ (\mu\mu)\varphi$ events. The plot shows the number of events found in each region of p_z and the normalized J/ψ χ^2difference.

The type of EF vs. L2 χ^2 plots presented in Figures 2, 3, and 4 are a type of two-dimensional correlation plot designed to examine the number of events left after a new χ^2 selection criterion is applied. The EF and L2 triggers perform tracking differently, resulting in different vertex quality; the purpose of these plots is to examine the impact of a wide range of new χ^2 selection criteria on the data from the EF and L2 triggers, to give an idea of how many events are kept by each trigger at the new criteria, and to compare these two vertex qualities graphically. These plots are created using a pair of nested FOR loops, themselves inside of a FOR loop that runs over all of a Monte Carlo dataset's events. The outer FOR loop is designed to run over the L2 χ^2, from 0.25 to 20.5 in increments of 0.25, while the inner FOR loop is designed to do the same for EF. During each iteration of the nested FOR loops, the code looks at the EF and L2 χ^2 of the candidate, and compares it to the current respective increment of the FOR loop – the cut. If the χ^2 value of either the EF or L2 are above the current cut, nothing happens. However, if the χ^2 value of both the EF and L2 are below the current cut, a data point is saved at the location (current EF cut, current L2 cut) on the xy-plane.

As an example, take an event with an EF χ^2 of 3.3 and a L2 χ^2 of 4.6. The outer L2 FOR loop and the inner EF FOR loop both begin at 0.25; as the χ^2 for both triggers is greater than 0.25, no data are saved. The inner EF loop's cut increments to 0.5; again, both χ^2 values are greater than this, so nothing happens. This continues until the EF loop increases to 3.5. In this case, the EF χ^2 is less than the EF cut, but the L2 χ^2 is still larger than its current cut, 0.25. Once the EF loop reaches 20.5, the L2 loop's cut increments to 0.5, and the EF loop begins again. This continues until the L2 loop's cut is 4.75, and the EF loop's is 3.5. At this point, the EF and L2 χ^2 values are both less than their respective cuts. As a consequence, a data point is saved at (3.5, 4.75) on the two-dimensional plot. The EF loop then increments its cut to 3.75, another data point is saved at (3.75, 4.75), and so on for every event in the dataset.

This particular analysis was performed for both Run-1 and Run-2 data. The result of this analysis for Run-1 can be seen in Figure 2. As we wanted to retain the high efficiency of the original $J/\psi\ \chi^2 < 20$ cut, any new cut needed to be based on a point where at least 95% of the events were retained. From Figure 2, this point appears to be < 7 for the EF trigger and < 10 for the L2 trigger. Based on this, the $J/\psi\ \chi^2$ selection criterion was reduced from < 20 to < 10. While a smaller, more precise cut would allow a greater reduction in background, the switch from Run-1 to Run-2 made a simpler selection preferable; a more precise cut would instead be created for Run-2 using Run-2 data and software. This criterion has been installed in the ATLAS High-Level Trigger in

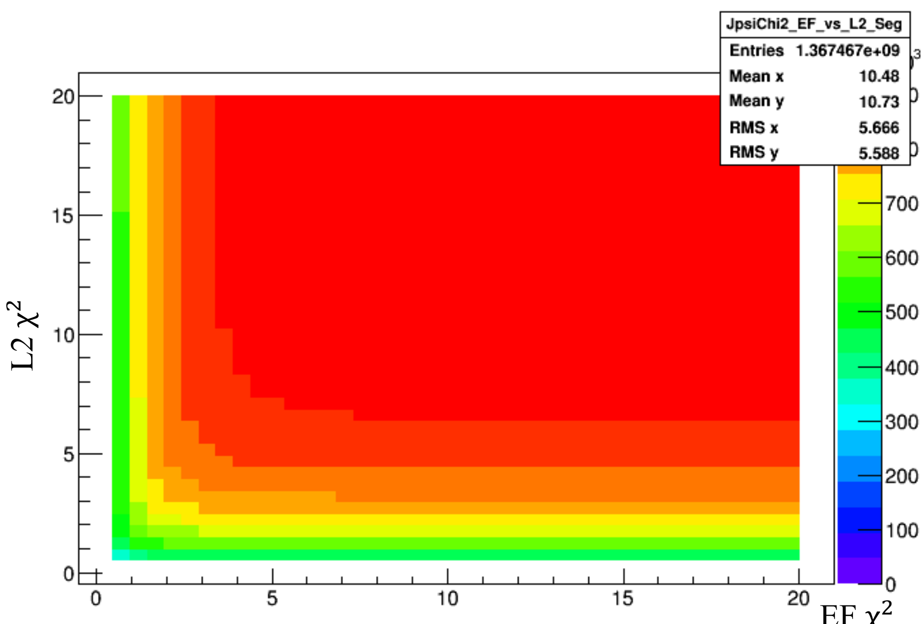

Figure 2: The EF vs. L2 χ^2 correlation for Run-1 MC $B_s \rightarrow J/\psi\,(\mu\mu)\varphi$ data. The z-axis is the number of events. ~95% of events are contained in the dark red block. From the plot, it is seen that χ^2 cuts of ~7 for EF and ~10 for L2 retain the entire dark red block. This is the motivation for the χ^2 < 10 selection criterion.

parallel with the original < 20 cut, to test its acceptance. While tightening the selection criteria reduces the high-level trigger rate, the background was not studied, and as such we cannot say how much the rate was reduced. However, these tightened criteria do ensure that a higher fraction of the data that trigger the HLT and are saved are data of interest.

Further analysis was done on Run-1's efficiency correlation plot by applying selection criteria to the offline reconstructed χ^2 of both the J/ψ and the B (both of which are constructed similarly, as described in section 6.2), and examining the effect this had on the EF vs. L2 χ^2 plot. To see if there is a space for further tightening of the χ^2 cut, six additional plots were made (Figure 3) from the $B_s \rightarrow J/\psi\ \varphi$ dataset, where data points were created if the offline reconstructed J/ψ vertex fit χ^2 was less than 200 (Figure 3a) or less than 10 (3b), and if the offline reconstructed B vertex fit χ^2 was less than 10 (3c), 5 (3d), 3 (3e), or 2 (3f), respectively. For the offline reconstructed J/ψ χ^2, the cut of 200 was chosen due to its being the maximum χ^2 allowed in offline reconstruction, while 10 was the value I recommended for the HLT cut for the J/ψ. The values of 10, 3, and 2 for the offline reconstructed B χ^2 were chosen because they are used in particular physics analyses, while 5 was chosen as an intermediate point; B $\chi^2 < 10$[7,8] represents the preselection of events for $B_s \rightarrow J/\psi\varphi$ and selection for J/ψ vertices, the B $\chi^2 < 3$[7] cut represents the final selection of events for $B_s \rightarrow J/\psi\varphi$-oriented analyses, and the B $\chi^2 <$ 2[8] is the cut used in the final selection for the $B_s \rightarrow J/\psi\varphi$ lifetime analysis. This analysis was performed in order to determine if the restriction of the offline χ^2 had a significant effect on the trigger efficiency. As can be seen in Figure 3, there is not a significant difference in the number of events per colored block.

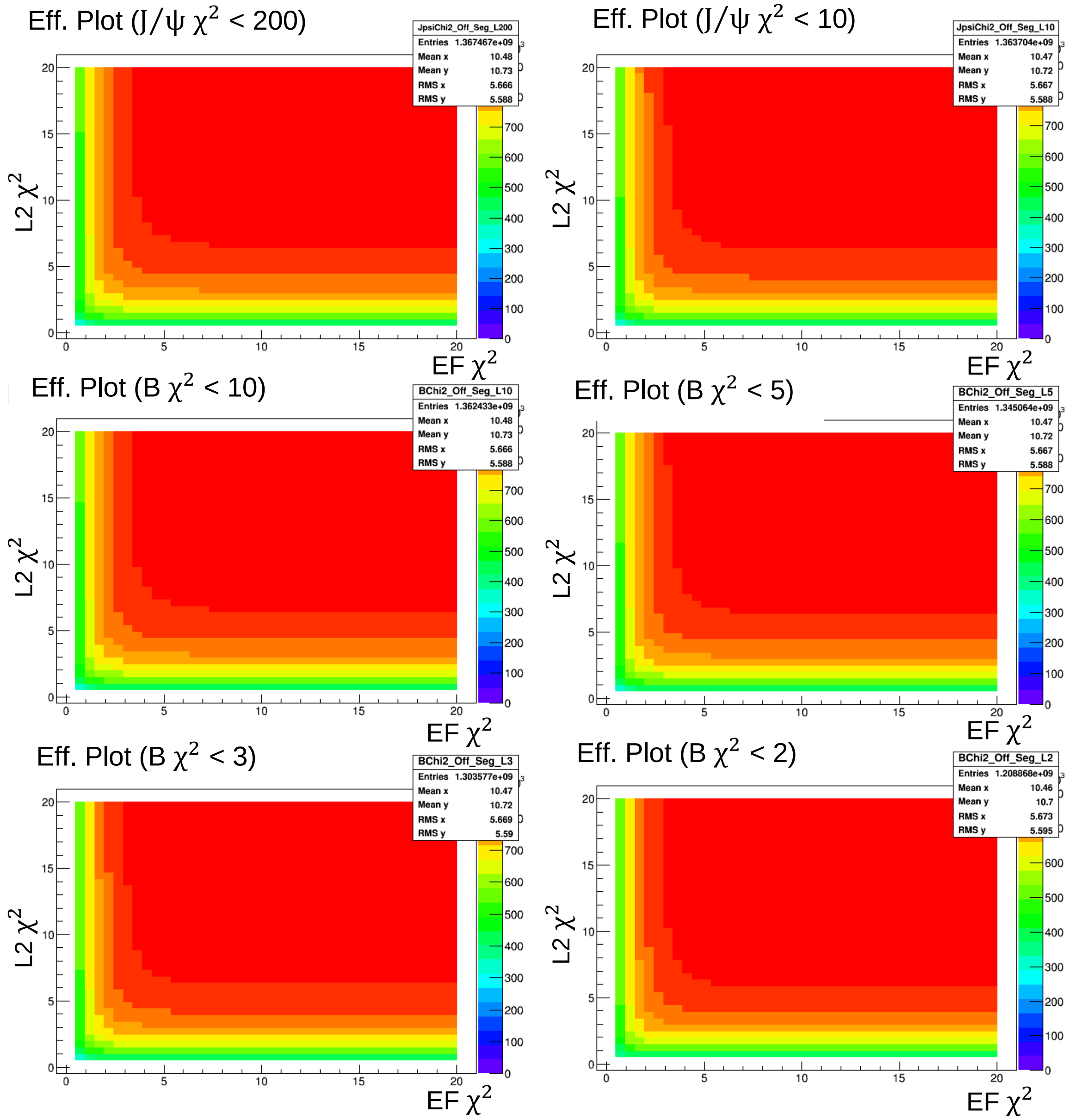

Figure 3a, b, c, d, e, and f: Correlation plots of EF vs. L2 χ^2 with various cuts applied to the offline reconstructed χ^2 Run-1 MC $B_s \rightarrow J/\psi\,(\mu\mu)\varphi$ events. The z-axis is the number of events. Those cuts are: $J/\psi\ \chi^2 < 200$ (top left), $J/\psi\ \chi^2 < 10$ (top right), B $\chi^2 < 10$ (middle left), B $\chi^2 < 5$ (middle right), B $\chi^2 < 3$ (bottom left), and B $\chi^2 < 2$ (bottom right). Note the minimal difference relative to Figure 2; the boundaries of the high χ^2 region have not significantly changed.

Run-2 signal and background Monte Carlo events were also analyzed. Their correlated EF vs. L2 plots can be seen in Figure 4. Note the differences between the $b\bar{b} \rightarrow J/\psi\,X$ signal and the $b\bar{b} \rightarrow \mu^+\mu^- X$ background; this is because in the $b\bar{b} \rightarrow \mu^+\mu^- X$ background, the two muons do not necessarily originate from the same vertex, and

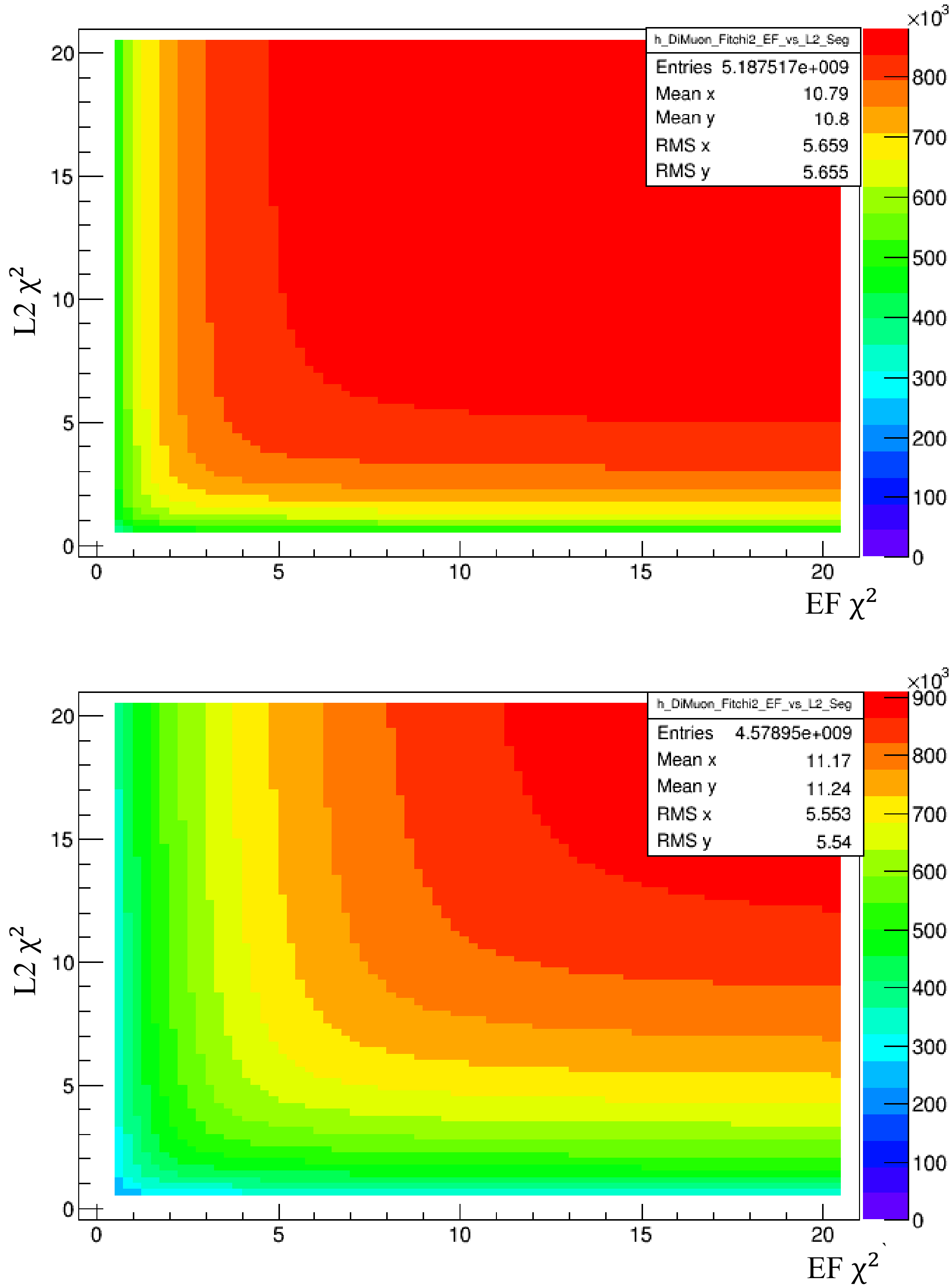

Figure 4: The signal (upper) and background (lower) EF vs. L2 correlation plots for Run-2 MC $b\bar{b} \rightarrow J/\psi X$ and $b\bar{b} \rightarrow \mu^{+}\mu^{-}X$ events. The z-axis is the number of events.

consequently the candidates that pass the vertex fit are either other types of B-decays or are combinatorial background, which has a naturally worse vertex quality. The upper plot in Figure 4 confirms the result of the study on Run-1, recommending a tightening of the

J/ψ χ^2 cut to < 10, and implies that it can be tightened further without significant loss of data of interest. The bottom plot shows how much of the background is removed by similar cuts.

The final part of the analysis involved creating signal efficiency, background rejection, and ROC plots. Run-2 MC events were used to refine the trigger for future runs. The signal efficiency plot in Figure 5 uses the Run-2 MC $b\bar{b} \rightarrow J/\psi\, X$ dataset. The HLT dimuon vertex χ^2 is graphed versus the signal efficiency, to determine how many events will be left for each value of the cut applied on χ^2. For example, in Figure 5a, if a χ^2 < 5 cut were applied, the dataset would retain ~90% of its events. A background rejection plot is similar to the signal efficiency, save that it shows the $b\bar{b} \rightarrow \mu\mu$ background, and rejection = 1 – efficiency. As an example, in Figure 5b, if the same χ^2 < 5 cut were to be applied, ~30% of the background events would be removed. Finally, the ROC plot (Figure 5c) compares the signal efficiency to the background rejection over a range of χ^2 cuts. These three plots are the official result of the study, and will be used by the ATLAS B-Trigger group in creating new vertexing selection criteria for the 2mu4_Jpsimumu trigger in the future.

Any new cut applied will have an impact on the rate by which the 2mu4_Jpsimumu trigger is activated. In general, this trigger will activate on any dimuon at or above a certain transverse momentum that can be reconstructed as a J/ψ. As such, the change to the trigger rate because of new J/ψ χ^2 cuts can be studied using the $b\bar{b} \rightarrow \mu\mu$ background dataset, which is comprised of ~4.5% $J/\psi \rightarrow \mu\mu$ decays. A histogram showing the impact on the trigger rate can be seen in Figure 6. If the above χ^2 < 4 cut were to be applied, the 2mu4_Jpsimumu trigger would activate at ~70% of the current rate, while the Run-1 $\chi^2 < 10$ cut would result in it activating at ~90% of the current rate for Run-2 data.

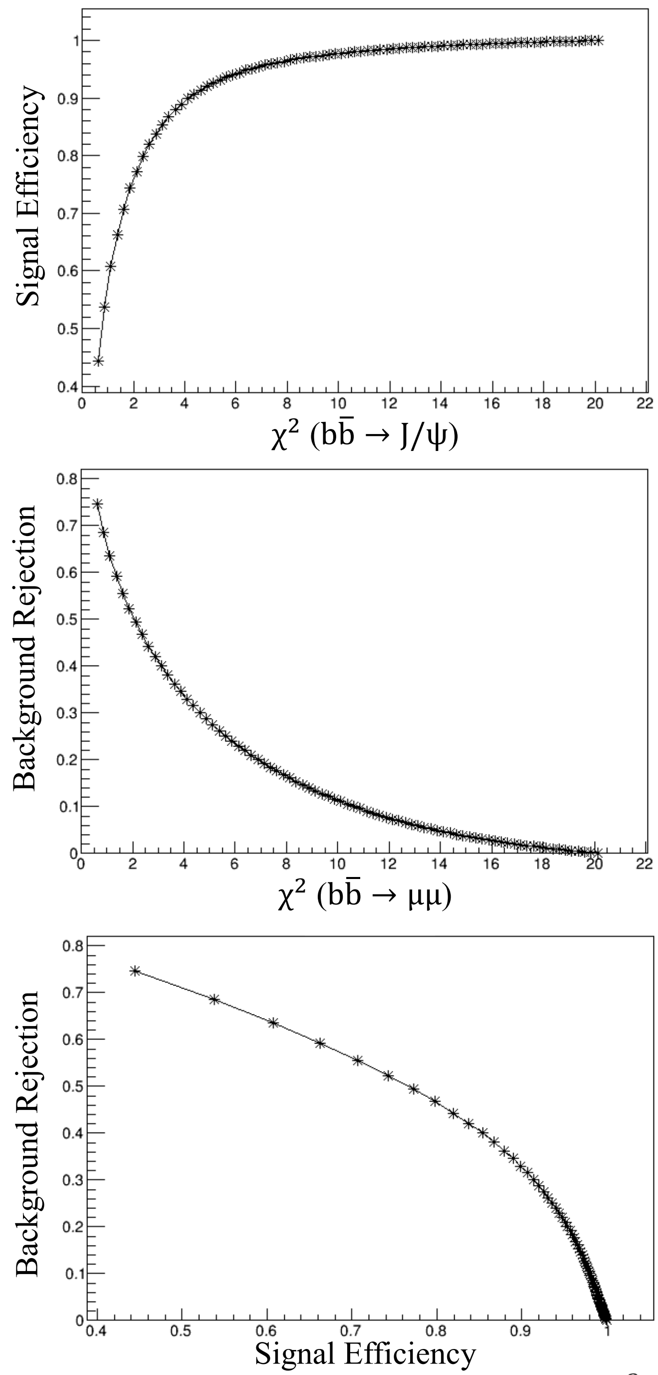

Figure 5a, b, and c: The signal efficiency versus χ^2 (upper), background rejection versus χ^2 (middle), and background rejection vs. signal efficiency (lower) of Run-2 Monte Carlo $b\bar{b} \to J/\psi\, X$ and $b\bar{b} \to \mu\mu X$ events subjected to various selection criteria described in the main text.

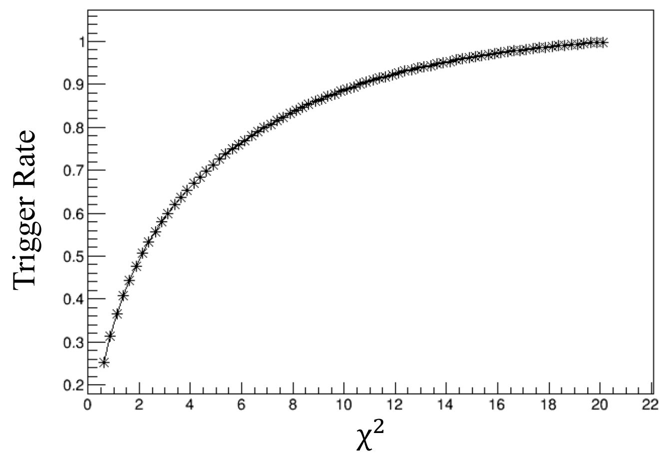

Figure 6: The trigger rate as a function of J/ψ χ^2 cut, as a fraction of the trigger rate for the original χ^2 < 20 cut.

6.4 Study of the Effect of the ATLAS Insertable B-Layer on the J/ψ Decay Vertex Fit Quality Selection Efficiencies

The Insertable B-Layer (IBL)[9] is an ATLAS subsystem designed to add a pixel layer close to the beam pipe. This improved track reconstruction infrastructure can enhance searches for processes that produce bottom quarks, and will extend the lifetime of the ID in the high-luminosity environment of the Run-2 LHC. This section describes a study performed to ensure the that IBL does not change the conclusions reached in the study described in section 6.3.

The IBL was installed into ATLAS in 2014-15 and operated during 2015 and 2016. During Period H, ATLAS's period of data-taking that corresponds to the interval October 6 – 12, 2015, there were intervals when the IBL was off. This study compares data taken when the IBL was both on and off, to study the effect of the IBL on the trigger rate.

While the IBL substantially improves secondary vertex reconstruction resolution, the effect on the vertex quality in terms of the χ^2/NDF is different: χ^2 describes the ratio between the summed track parameters' absolute difference from the mean (with and without vertex constraint) to the track parameter errors. In the ideal case, the χ^2 of the signal decays should remain the same, as the vertex resolution scales with the track parameter errors. A slight difference can be observed if the track parameters are not precise (e.g. due to an imperfect description of the detector geometry). For background events, trying to force tracks that did not originate from the same point into a common vertex should result in a higher χ^2 than without the use of the IBL, as the inconsistency is seen with better precision. It is thus expected that the χ^2 values will be slightly higher when the IBL is on.

The data studied were accumulated with the 2mu4_Jpsimumu and 2mu6_Jpsimumu triggers, which are dominated by $J/\psi \rightarrow \mu\mu$ events. Note that the 2mu4_Jpsimumu trigger is heavily prescaled, and as such the 2mu6_Jpsimumu trigger is not a subset of it. There were two steps to this analysis: creating correlated EF vs. L2 plots of the Period H data taken when the IBL was on and when it was off; and directly examining the trigger data retention rate under a specific χ^2 cut. A significant change in the retention (> 10%) would necessitate re-examination of the Period H data and possibly reconsideration of the trigger selection criteria.

The correlation plots, of the type discussed in section 6.3, can be seen in Figure 7. Plots are shown for cases in which the IBL is on and off. The main feature of note is that the boundaries of the different (colored) sections of the EF and L2 χ^2, corresponding to bins described by the number of events, transition at higher χ^2 values when the IBL is on

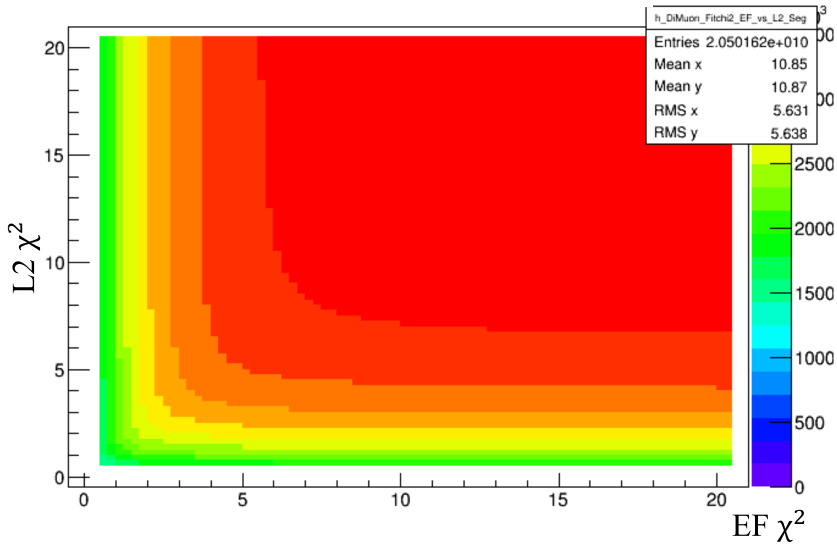

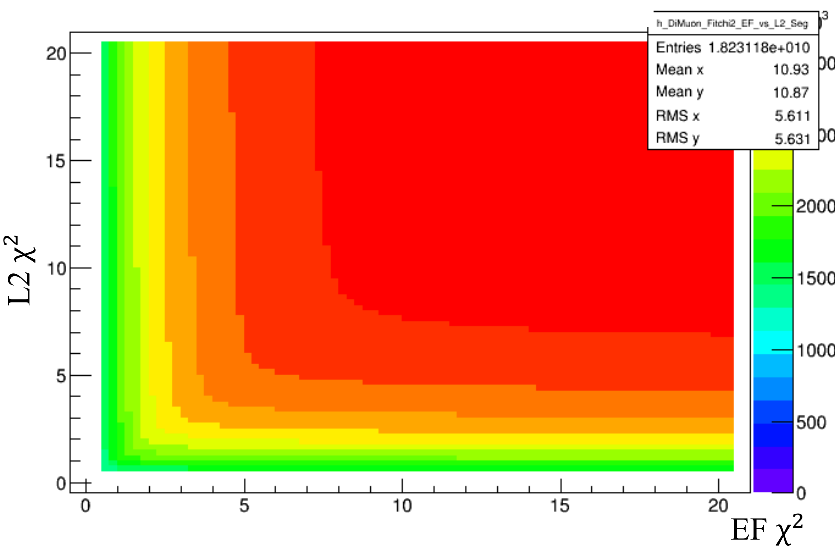

Figure 7: The EF χ^2 vs. L2 χ^2 correlation plots when the IBL was on (top) and off (bottom). The z-axis is the number of events.

than when the IBL is off. This difference has a value of ~2 in EF χ^2 and < 2 in L2 χ^2 for the rejected high χ^2 events (the dark red block), representing the part of the histogram with the highest number of events.

Determining the retention resulting from a χ^2 cut is a matter of applying the cut and finding the ratio of how many events are left divided by how many there were originally. For example, a value $\chi^2 < 5$ for EF and L2 triggers preserves a signal retention of ~90%, and a background rejection of ~30%, in the analysis of section 6.3. This study makes use of the requirement $\chi^2 < 5$ to evaluate the change in the trigger rate. However, in this study, since we are using data rather than Monte Carlo, we can't directly estimate the signal efficiency and background rejection. Instead we look at the decrease in the rate of data retained by the trigger as a function of the χ^2 cut to get a sense of whether or not the IBL makes a significant difference. There are four retention factors to be examined, for the EF and L2 triggers, when the IBL was on and off. The result can be seen in Table 1. The difference between retention factors for the EF is expected from the correlation plots. Note that the retention is slightly lower when the IBL is on compared to when it is off, as expected.

Item	**Original # of Events**	**# After Cuts**	**Retention**
EF, IBL On	3282604	2973358	0.908
EF, IBL Off	3654751	3409691	0.933
L2, IBL On	3200413	2920054	0.912
L2, IBL Off	3548599	3241947	0.914

Table 1: Number of events recorded by the EF and L2 triggers after application of a cut at J/ψ vertex $\chi^2 < 5$, and the associated calculated retention, for conditions with and without the IBL.

Additionally, Figure 7 shows no distortions – such as significantly (on the order of 10%) different χ^2 quality or bumps – between when the IBL was on and off. Based on the data from these figures and table, it does not appear as if the IBL influences the χ^2 cut retention and the shape of the χ^2 distributions significantly enough to need to reconsider the trigger selection.

6.5 Conclusions

A trigger study using Run-1 and Run-2 Monte Carlo data has been completed. Based on Run-1, a $\chi^2 < 10$ cut is recommended to optimize the trigger. This selection criterion was installed in the 2015 B-trigger, in parallel with the original $\chi^2 < 20$ cut. For Run-2, both the EF vs. L2 correlation plots as well as the signal efficiency, background rejection, and signal efficiency vs. background rejection (ROC) plots have been created. These last three plots will guide trigger decisions for new vertexing selection criteria in the future. Correlation plots between the HLT χ^2 and the other data from the HLT were also studied, but no significant correlation was found. These decisions will be based on the best working point for existing and proposed analyses, ensuring that the minimal necessary signal is preserved while rejecting the maximum amount of background. The new selection criterion based on this study will likely become the default criterion for the trigger, starting after 2016 data-taking finishes. The analysis of the IBL data in Period H demonstrated little dependence in the rate of retention of data resulting from the new χ^2 cuts.

6.6 References

1. Kirk, J. (2007). B-Triggers at ATLAS and CMS. Nuclear Physics B (Proc. Suppl.) 170, 292–297.
2. ATLAS High Level Trigger Group Collaboration (2003). Architecture of the ATLAS high level trigger event selection software. Nucl. Instrum. Meth. A518, 537-541.
3. Particle Data Group (2014). $c\bar{c}$ Mesons. Chin. Phys. C, 38, 090001.

4. Kostioukhine, V. (2003). VKalVrt - package for vertex reconstruction in ATLAS. ATL-PHYS-2003-031.

5. ATLAS Collaboration (2009). Vertex Reconstruction in the ATLAS Experiment at the LHC. ATL-INDET-PUB-2009-001.

6. Billoir, P. and Qian, S. (1992). Fast vertex fitting with a local parametrization of tracks. Nucl. Instrum. Meth. A311, 139-150.

7. Aad, G., et al. (2014). Flavor tagged time-dependent angular analysis of the $B_s \rightarrow J/\psi\ \phi$ decay and extraction of $\Delta\Gamma_s$ and the weak phase ϕ_s in ATLAS. Phys. Rev. D 90, 052007.

8. ATLAS Collaboration (2010). The ATLAS Pixel Insertable B-Layer (IBL). Nucl. Instrum. Meth. Section A, Vol. 650, Issue 1, p. 45-49.

9. ATLAS Collaboration (2012). Overview of the ATLAS Insertable B-Layer (IBL) Project. PoS RD13, 012.

Chapter 7: Radiation Tolerance Studies of Devices for Future Collider Experiments

7.1 Introduction

Detectors and other devices being developed for use in high-energy colliders, such as the HL-LHC, require testing in radiation environments comparable to those anticipated in situ. During exposure to a high-radiation environment, electronics and sensors degrade in performance due to the energy deposited by charged particles causing ionization and lattice displacement of the electronic medium. Mechanical structures experience accelerated aging and degradation of their integrity. Sensors and electronics in the Inner Detector of ATLAS, from which much of the data used in B-physics are drawn, experience the highest radiation, and as such experience the greatest damage and degradation. To understand this degradation, devices are irradiated at the Los Alamos Neutron Science Center (LANSCE) proton beam facility.

Two different radiation damage projects are presented here. The first is a method of monitoring the fluence and profile of a radiation beam, such as the one at LANSCE, in real time by measuring the forward voltage drop across an array of diodes. The second project is the creation of a custom printed circuit board (PCB), for application to the measurement of charge collection under irradiation, and for the biasing of double-sided devices during irradiation.

7.2 Proton Irradiations

LANSCE provides an 800 MeV proton beam with an 80 nA current, in macro-bunches of 5×10^{11} protons per pulse. The beam can be focused down to about 2 cm in diameter. The section of the LANSCE irradiation facility used by these projects has two parts, the Experimenters' Control Room and the Irradiation Hall (Blue Room).

The Experimenters' Control Room contains equipment for remote monitoring of the beam, as well as workshop facilities for setup and alteration of experimental devices and equipment. The hallway between the Control Room and the Blue Room provides a location for electronics that control equipment in the Blue Room.

The Blue Room is where the proton beam emerges. The UNM experimental team places freezers near its entrance, along a baffled hallway, where irradiated devices are stored post-exposure, to inhibit the annealing of silicon. The Blue Room proper contains the beam pipe, the beam stop, an elevated table on which experimental devices can be placed, patch panels, and a laser for aligning samples with the beam.

Devices under test are attached with kapton tape to G-10 cards which are positioned sequentially in a slotted box in the path of the beam. The beam is applied, and at certain pre-determined intervals of incident fluence the beam is stopped, and specific devices are removed. A typical exposure applies fluence between 10^{12} and 10^{16} 1 MeV neutron equivalent per cm^2 (neq/cm^2). 1 MeV neutron equivalence is the standard way to report fluence for the purpose of hadronic radiation damage studies, representing the damage caused by 1 MeV neutrons. The fluence from the 800 MeV protons provided at LANSCE can be converted to 1 MeV neq/cm^2 by multiplying it by 0.71[1]. The LANSCE test beam can achieve a fluence of 10^{15} neq/cm^2 in about 3 hours. In order to perform these experiments, it is necessary to know both the beam's profile and its fluence; being able to measure it in real time is important for precision. This motivated the first project presented here, the Diode Array.

7.3 The Diode Array

7.3.1 Motivation

Existing techniques used to measure charged beam profile and fluence, such as aluminum foil activation[2], flying wire[3], radiographic image analysis[4], and Faraday cups[5], have disadvantages. Some of them cannot be read out while the beam is running, have large uncertainties, or have a lower sensitivity than aluminum foil. In order to examine the properties of the beam in real time, we developed a diode array[6] that can be placed in the path of the beam as a direct monitoring device. Software has been developed to operate this device. Advantages of this array include easy readout, high spatial resolution, a wide range in which the forward voltage response is linear with fluence (between $\sim 2\times 10^{12}$ and $\sim 5\times 10^{14}$ neq/cm^2), measurements independent of the array's orientation, dose-rate independence, and low cost of construction. However, this response is temperature dependent, a factor minimized by limiting its current, as described below.

7.3.2 Description of the Diode Array

The diode array[6] is a 7x7 grid of OSRAM BPW34F[7] p-i-n diodes soldered back to back on a metalized G10 board (Figure 1). Four columns are attached to the front, and three to the back, interleaved in such a way as to produce a non-overlapping diode matrix. The voltage drop across the diodes depends linearly on the fluence; thus, a voltmeter reading the voltage drop across the diode can measure the fluence. By comparing the forward voltages of all the diodes on an array at a given time, it is possible to measure a beam's profile as well.

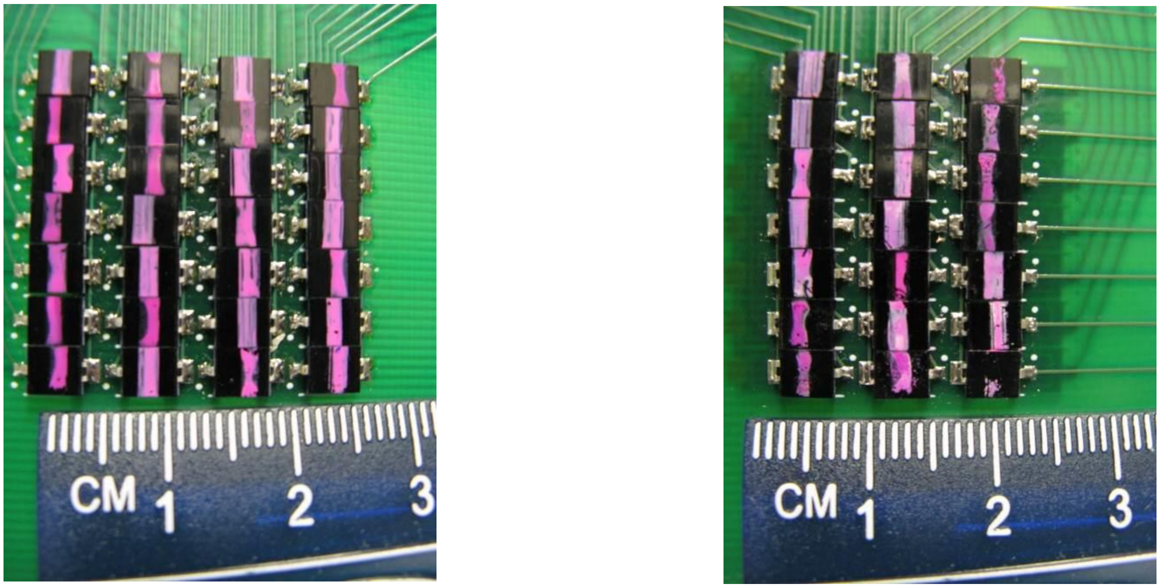

Figure 1: The front (left) and back (right) of the diode array.

The forward voltage across the diode increases linearly with the fluence under a constant forward current, as can be seen in Figure 2. This graph shows the diode's response under exposure to 23 GeV protons and 0.8 MeV neutrons, converted to 1 MeV neq. Above $\sim 5\times10^{14}$ 1 MeV neq/cm^2, the diodes reach saturation. These diodes are not linear below 2×10^{12}; in this region, a higher-sensitivity diode from CMRP would be more effective[8]. The threshold for these forward biased diodes is 0.6 V.

Each diode acts as a single point of measurement, in the xy-plane, of fluence; as a result, the resolution of the beam profile depends on the density of diodes in the array. The array collects data from discrete points, and as such the resolution is given by $\mathrm{p}/\sqrt{12}$, where p is the pitch between diodes. In the case of this array, the pitch is 3.8 mm in both x and y, giving a resolution of 1.1 mm. The sensitive area of the diode chip is 2.65 mm x 2.65 mm, and the dimensions of the overall chip are 4.0 mm x 6.7 mm.

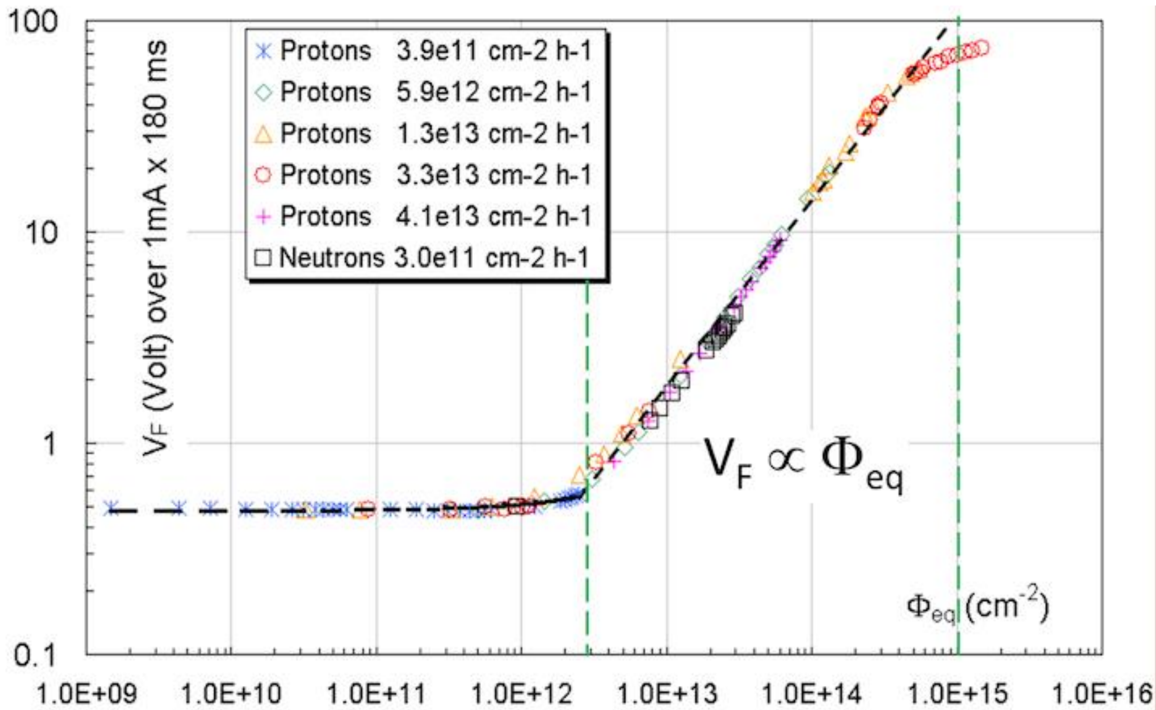

Figure 2: Forward voltage versus the fluence for OSRAM BPW34F p-i-n diodes. This graph shows the diode's response under exposure to 23 GeV protons and 0.8 MeV neutrons, converted to 1 MeV neq. From [6].

Interleaving these diodes on the PCB layout allows us to achieve a pitch of 3.8 mm of the sensitive area.

The diode array system makes use of a Keithley 2410 SourceMeter[9] (for biasing and readout) and a Keithley 706 Scanner[10] (for switching between the 49 diode channels); it also includes a computer with custom LabVIEW[11] software, and a 30m cable, necessary to separate the data acquisition equipment from the array in the high-radiation environment. The LabVIEW program controls all the instruments.

Calibration of the array involves using aluminum foil activation, with a 2x2 cm^2, ~99.5% pure sheet of aluminum foil attached directly to the diode array, placed in the path of the 800 MeV proton beam. The relationship between fluence and aluminum foil activation is very well understood[12,13], and consequently aluminum foil activation is a common way to calibrate new technologies for irradiation. Four sets of foils were used, along with two arrays, upstream and downstream of the beam (to image both the initial beam and the beam after it has been spread out by intervening samples). The diode arrays were read out when the fluences were estimated to be 4×10^{13}, 2×10^{14}, 3.2×10^{14}, 7.2×10^{14}, and 8.2×10^{14} neq/cm^2. After each measurement an aluminum foil was removed. Later, each foil was segmented into sixteen squares, and its activation measured in a gamma spectrometer[14]; the fluence this represented was then compared to the voltage drop in the diodes, to calibrate the system. The result of this analysis can be found in Figure 3. As all the diodes are identical, and have the same response, there is no position-dependence in how different parts of the diode array respond to fluence. This is what allows us to perform beam profile measurements in real time. From the fitted line on Figure 3, we obtain a linearity coefficient of $c = (9.558 \pm 1.536)\times10^{-14}\ \mathrm{V/cm^2}$ for 1 MeV neutron equivalence[6]; this fit has a $\chi^2 = 4.43$ for three degrees of freedom. This

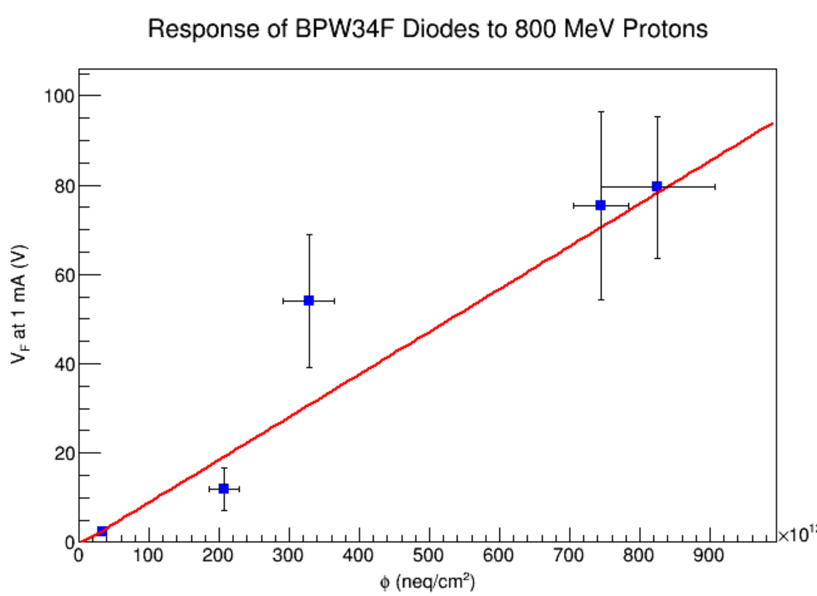

Figure 3: Calibration plot showing the response of the forward voltage of the diode array at 1 mA as a function of proton fluence.

calibration coefficient could be applied to any diode array using the same OSRAM BPW34F p-i-n diodes in the same geometry.

7.3.3 LabVIEW Software

Custom LabVIEW software was written to scan all 49 channels of the diode array in under a minute, an approach to control temperature effects on noise. The LabVIEW program controls the Source Meter and Scanner, regulating the voltage, pulse rate, and channel-switching for the setup. The LabVIEW program includes a hierarchy of a top-level control VI (Virtual Instrument) and 24 sub-VIs, including drivers for the readout equipment. In addition to scanning the diodes, this program also reads temperature at channel #50, heat being a major source of systematic uncertainty[14] in resistivity measurements of this type of diode.

The program performs the following steps:

1. Initialize scanner: The Keithley 706 Scanner is activated and readied for monitoring current input and output.
    a. Close circuit: The circuit between the scanner, sourcemeter, and the first diode is closed, opening a path for current to flow.
    b. Open new file: Readies a new file to write data to.
2. Initialize Sourcemeter: The Keithley 2410 SourceMeter is activated and readied for supplying current.
    a. Set compliance and output: The voltage compliance and total current output (1 mA) is set.
    b. Activate Sourcemeter, send first current burst: Current is supplied, in 10 ms bursts of 1 mA.

    c. Take sample: The forward voltage is measured while the current is being supplied.
    d. Repeat steps b and c nine times with a 3 ms delay, taking a total of ten samples and averaging them; the total measurement time per diode is about 130 ms.
    e. Write data to file.
3. Close current circuit: To prevent current flowing during the switch between diode channels.
4. Wait a time set in the program, usually ~800 ms.
5. Open next circuit to access the next diode channel.
6. Repeat steps 2-5 across all 50 circuits (49 diodes and a temperature sensor).
7. Close Sourcemeter and Scanner sessions, calculate standard deviation, save and close file.

Once all the channels have been scanned, the data are written to a file, averages and standard deviations are calculated, and the data are graphed. Using this graph, and monitoring the forward voltage drop as fluence increases, it is possible to determine both the beam profile and fluence (Figure 4). The voltage drop can be converted to fluence by finding the linearity coefficient in the plot of forward voltage drop to fluence (shown on Figure 2), and then multiplying the drop by that value; see [6] for more details. This experiment was successful, and the diode array will be used in all future UNM LANSCE irradiation runs.

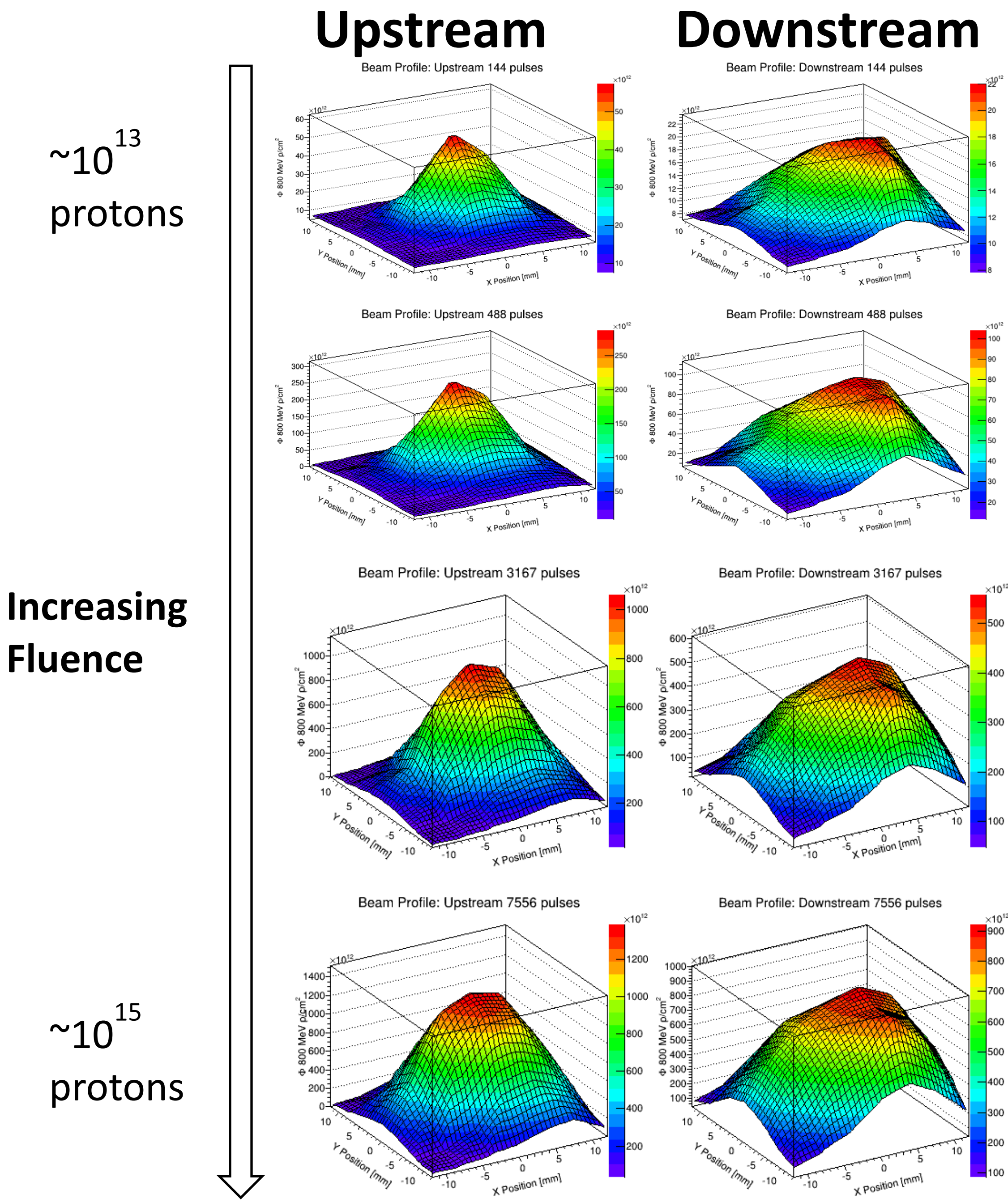

Figure 4: A series of graphs from two different diode arrays, showing the increasing fluence over time and beam profile. The "downstream" array was downstream of a number of experimental devices, which caused the beam to broaden before it got to that array.

7.4 A New Printed Circuit Board for Noise Reduction and Power Distribution

7.4.1 Motivation

In the process of developing new sensor technologies for high-radiation environments (like that of the LHC), it is necessary to determine how these sensors' efficiency for collecting charge changes due to radiation. The Upgraded Characterization Station (UCS)[15] (Figure 5) is an instrument designed to perform these measurements, by reading out an active sensor while it is positioned directly below a collimated Strontium-90 (beta) source. This stimulus has in the past been applied primarily to silicon sensors.

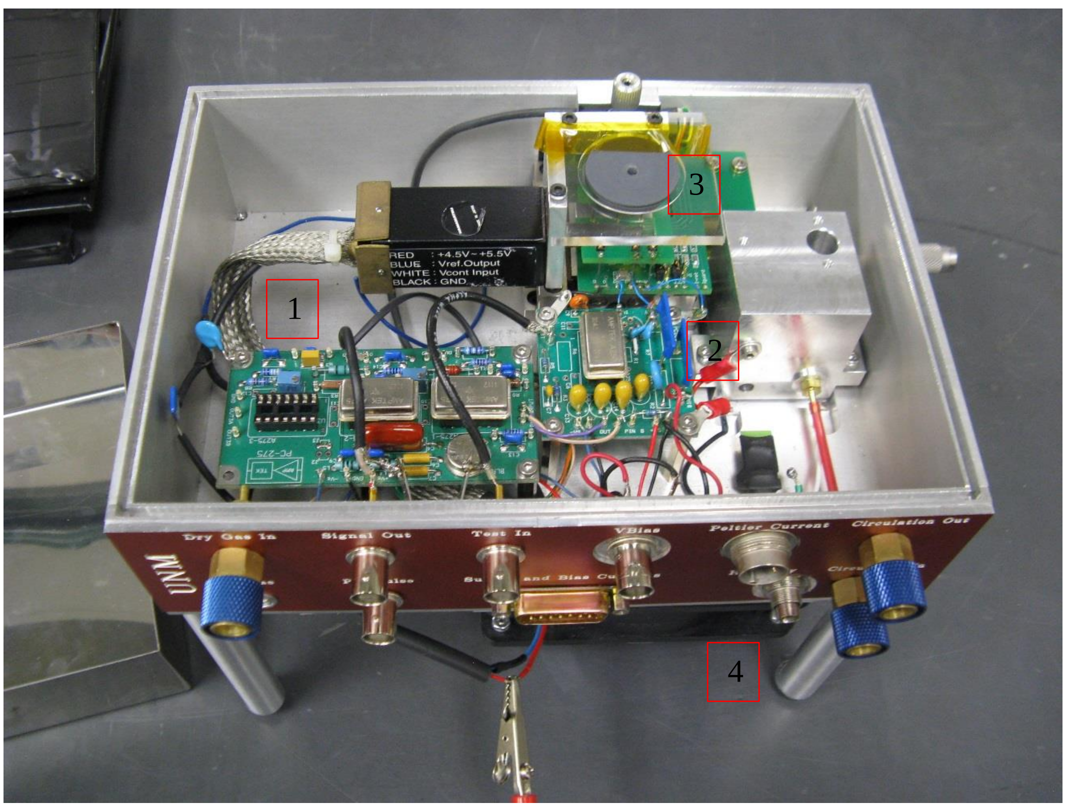

Figure 5: The Upgraded Characterization Station. The metal cover on the left normally goes on top of the UCS, to exclude external sources of radiative noise and light. The components include the noise filtering board (1), the preamplification section (2), the collimator, pole-wires, and board/sensor assembly (3), and the fan (4).

Our goal is to reduce the system noise so that it may be applied to devices with smaller signals, such as diamond sensors and very highly irradiated silicon sensors, as well. Normally, signal is identified by coincidence between hits on the sensor and hits on the scintillator material connected to a photomultiplier tube. The typical sensor signal is ~20,000 electrons[15]. Noise occurs when the sensor records a hit when no beta particle has passed through. Electronic noise – from, for example, radio frequency pickup, bias current fluctuation, and Johnson noise – can cause equivalent charges, mimicking a signal hit when there wasn't one. Limitations of the design of the readout system can also worsen noise. For low-signal sensors like diamond, this noise could overwhelm the signal. To this end, several experiments were performed, with the aim of reducing the readout system noise, including the creation of a new PCB to hold and power the sensor while bypassing some components of the UCS. This board was designed to be able to apply bias on top and bottom of a sensor or diode; it was used during the Los Alamos irradiation campaign, to bias 3D diodes under test.

7.4.2 Upgraded Characterization Station

The Upgraded Characterization Station has six major components: the PCB to which the sensor is attached, the station's preamplification section, the Data Acquisition (DAQ) control box, a DAQ board, a power supply for bias voltage, and the computer with the LabVIEW program that controls the system. This study only makes use of the equipment and code that analyzes the noise from the station, and as such explanations will be restricted to those items that have a direct bearing on the noise analysis. Additional information can be found in [16].

The LabVIEW control panel for this study can be seen in Figure 6. This user interface allows one to set parameters for the noise analysis, as well as acquire wave forms directly from the sensor amplifier system. The important parameters are the scan rate, the number of events, the time limit, the maximum and minimum voltage, and the step. The scan rate is the rate at which noise readings are taken; it was set to 75 Hz. The number of events is the total number of scans taken during a single activation of the LabVIEW code; this was set to be 20,000 events, to ensure sufficient statistics for comparison. The time limit is associated with the scan rate and number of events, as it needs to be large enough that the chosen number of events is consistent with the chosen scan rate. The maximum and minimum voltage determine the maximum gain of the preamplifier, and are also used as the range of the histogram; the values used in each histogram were chosen to span the noise range of the system for that particular

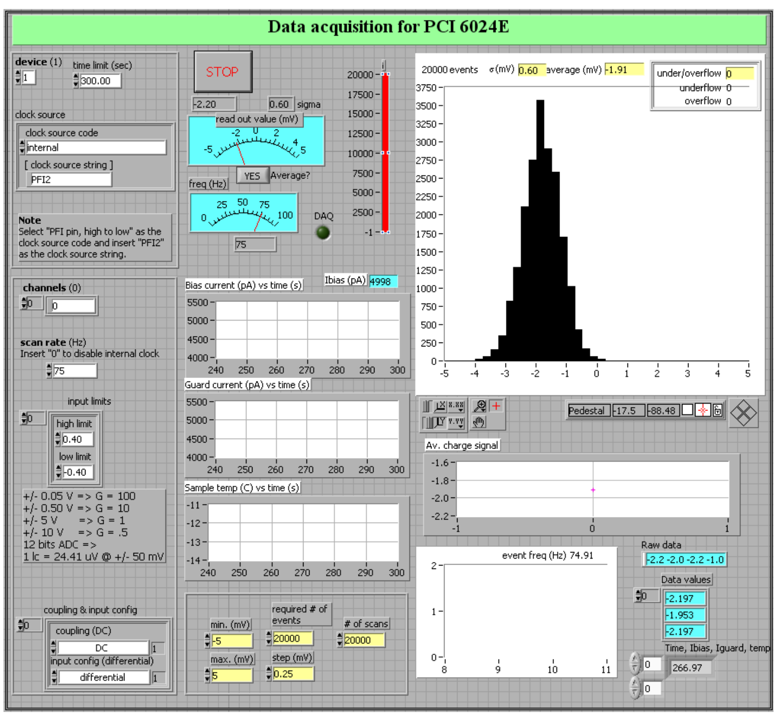

Figure 6: The control panel for the noise measurements on the UCS. The data shown are from a system prior to the board and sensor being attached.

measurement. Finally, the step is the binning; a value of 0.5 mV was used. The Data Acquisition Board is a National Instruments 6024E board which connects the computer with the LabVIEW code to the DAQ box and the rest of the equipment. It communicates commands and acts as the hardware controller.

The DAQ box contains the power supply for the preamplifier section of the characterization station, samples the signal, and sends it to the computer. It also contains a discriminator board for the input signal and a pump for circulating air into the Upgraded Characterization Station's chassis. The power supply for the bias is a Keithley 2410 SourceMeter, which was set to 11 V to bias the sensor.

The preamplifier box contains the pole-wires, the preamplifier, a board and sensor assembly, a collimator, and a cooling assembly. The pole-wires are a series of six unshielded conductive poles that connect the PCB to the preamplifier (Figure 7). The preamplifiers and signal shapers used in the UCS are an Amptek A250 and A275, and are used in combination with a type 2SK152 Field Effect Transistor (FET). They serve to shape and amplify the signal before it is sent to the DAQ box. The board and sensor assembly (Figure 8) is a movable structure upon which the PCB and collimator are attached. It can be adjusted so that the particle beam can be directed to different parts of the sensor. The collimator is a plastic tube (in order to minimize bremsstrahlung events) surrounded by a dense tungsten cone placed directly above the sensor (Figure 9), there to ensure that only the sensor – and not the nearby photomultiplier tube or other electronics – is irradiated. The cooling assembly takes in air from the DAQ box, cools it, and passes it over the PCB and its attached sensor when the device is operating. It cools only the board; cooling the other electronics requires additional equipment.

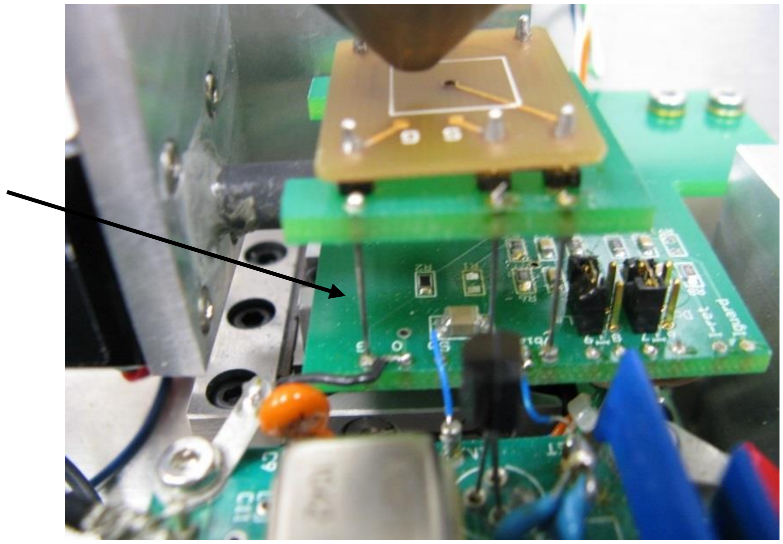

Figure 7: The arrow points to one of the pole-wires, which act simultaneously as current channels and structural supports. The old PCB is shown here as the brown board at the top of the stack.

The PCB of the UCS is the electronic platform on which experimental devices rest, and where they are connected to the electronics of the station. A physical picture and circuit diagram of the board can be seen in Figure 10 and Figure 11. The board is designed in such a way that the six pole-wires will connect from the sensor and

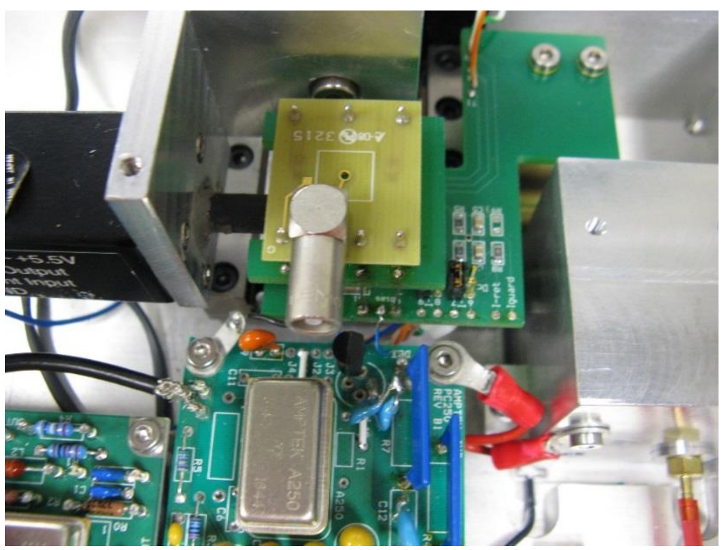

Figure 8: The board and sensor assembly, with the new PCB (the light green board) attached.

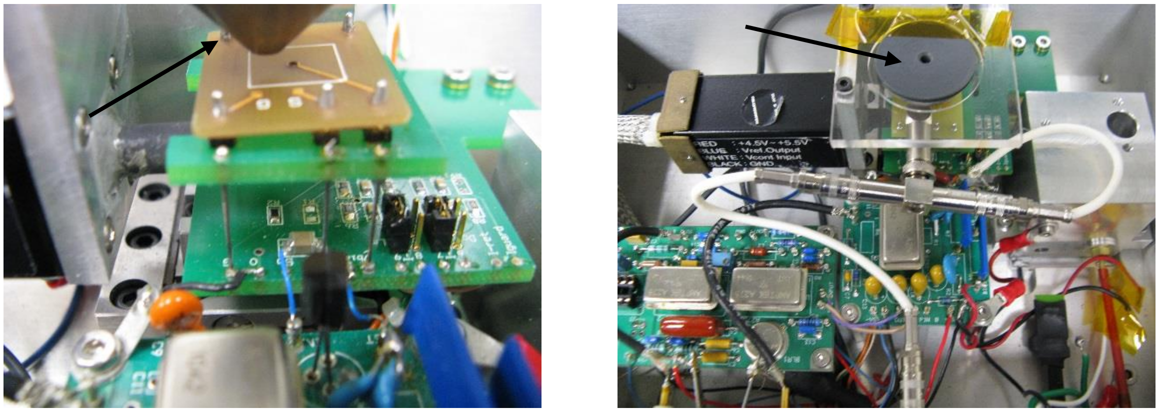

Figure 9: The arrow points to two views of the collimator. A radiation source is placed on top of the collimator, directly above the hole, and the cone directs a narrow, collimated beam towards the sensor. This is to ensure that only the sensor is irradiated. The photomultiplier tube is the black box on the left side of the right picture.

thermistors on the board to the preamplifier. In Figure 11, sites 1 and 2 are the signal-in and signal-out locations. Site 3 is the ground connection. Sites 4-6 connect to the two thermistors on the back of the board and transmit the reading from them to the DAQ board and LabVIEW program. For the purposes of measuring the noise from the UCS itself, the temperature of the board is not a significant contributing factor, and as such data from these thermistors are not used in this analysis. The gain of this station[16] is $534\ \mathrm{e^-/mV}$.

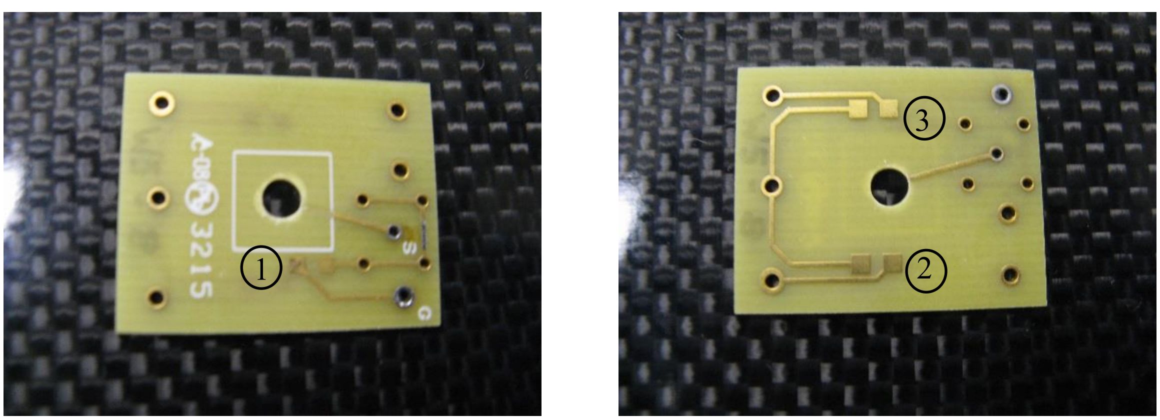

Figure 10: The front (left) and back (right) of the new PCB. The five-hole section is where the coaxial cable connects; the two pairs of pads at locations 2 and 3 are where the thermistors attach.

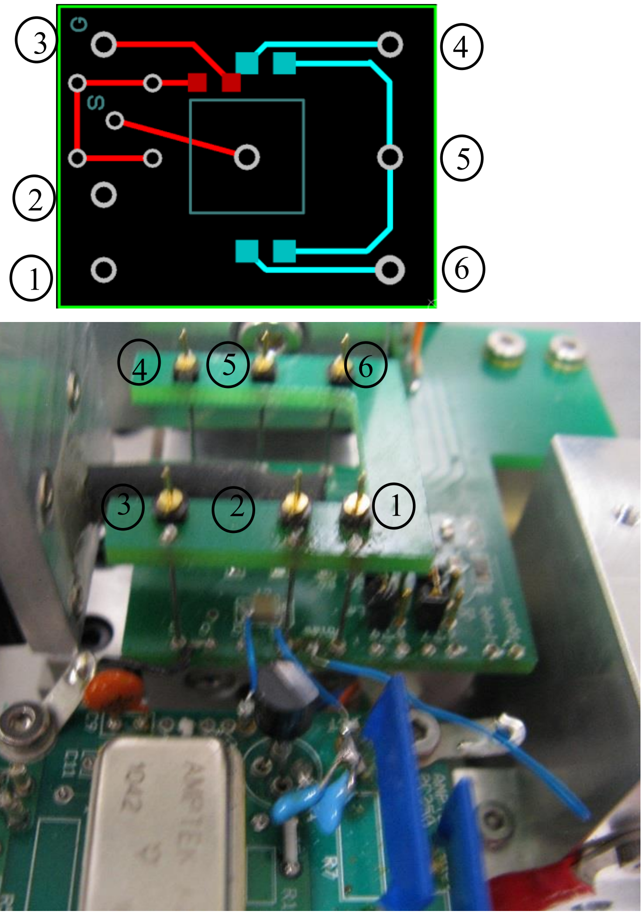

Figure 11: The circuit diagram (top) of the new PCB. Red lines represent connections on the top of the board, while blue lines represent connections on the bottom. The numbers correspond to the attachment sites in the bottom figure, and are further described in the text.

7.4.3 Modified Interface (PCB) Board

To reduce the noise contribution from exposed conductors, a new printed circuit (interface) board was designed that bypassed the pole-wires, sites 1 and 2; as a ground, site 3 does not need to be bypassed, and the thermistors are not sensitive enough to noise to need a bypass. The board was modified to accept a LEMO cable, for minimum volume. The connector on the other side of the cable is soldered directly to the electronics, the coaxial configuration of the connector potentially reducing the radiative noise. The coaxial cable both applied the bias voltage and carried the detector signal out to the readout electronics. This was done using the circuit design CAD freeware *PCB Artist*.

For the modified board to settle into its cradle, it needs six, 45 mil diameter holes in a configuration that matches the pins of the UCS (sites 1-6). This configuration can be seen in Figure 11, and forms the basis for both the original and the modified boards. Sites 4, 5, and 6 are separated from their neighbor by 300 mils; sites 1 and 2 by 200 mils, and 2 and 3 by 500 mils. A conical socket was soldered into each hole, so the PCB could connect to the system. The modified PCB requires an additional five, 32 mil-diameter holes to accommodate the coaxial cable's connection (Figure 10). The four outer holes are separated by 200 mils in both directions, while the central one sits in precisely the center. These holes do not have any sockets soldered in; instead the coaxial cable's connector is soldered directly to the board. There is also a central, 45 mil-diameter hole, which acts as an access point for wire bonds to attach to the back of the sensor. All of the holes are plated. This board additionally has three pairs of metalized pads, at locations 1, 2, and 3 in Figure 10. Locations 2 and 3 are solder attachment points for the thermistors. The right pad at location 1 is for signal out, while the left pad is for ground; current is routed to and from these locations through the wire bond. Signal in is provided through the central hole. All pads, connectors, and hole plating are made of copper coated with electroless nickel immersion gold (ENIG), which is composed of a layer of gold over catalyzed copper, with a nickel barrier to prevent copper/gold interdiffusion[17]. It has low contact resistivity, does not readily tarnish, and bonds to solder, making it an excellent material for the PCB.

The installation of the modified PCB also demands rewiring of the UCS to bypass the pole-wires. Normally, current is routed from the DAQ box, through a pair of RC circuits, to the sensor and the preamplifier assembly (see Figure 12 for the circuit diagram). The capacitor on the right side acts to protect the FET transistor from high current. The coaxial bypass involves disconnecting two wires that connect the PCB's cradle to the main electronics of the UCS. One end of the coaxial cable is stripped, the conductor attached in series with the capacitor preceding the transistor and the shell attached to ground. This alters the circuit, excising the resistor/capacitor series. Resistor-capacitor (RC) circuits like these are often used as a form of low-pass noise filter. Low frequency noise is less able to pass through the capacitor into the ground than high frequency, and as such RC circuits serve to filter out high-frequency noise. These were installed for the UCS because its original power supply, an Applied Kilovolts model HP001ZIP025, was very noisy, with 55 mV of noise at high frequencies[18]. The current Keithley 2410 SourceMeter power supply produces substantially less noise: at high frequencies, it has a noise of ~20 mV[19]. This was thought to make the RC filters less

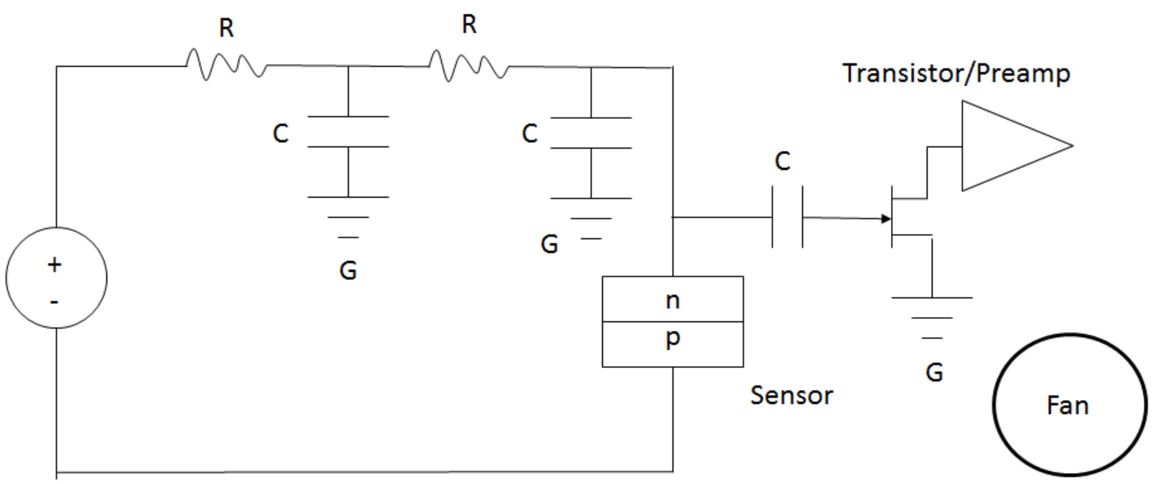

Figure 12: The default circuit diagram for the UCS. The fan is included, despite not being attached to the rest of the circuit, due to its being a potential source of noise for the system.

necessary for the current power supply. The new circuit diagram, with the RC circuits excised, can be seen in Figure 13.

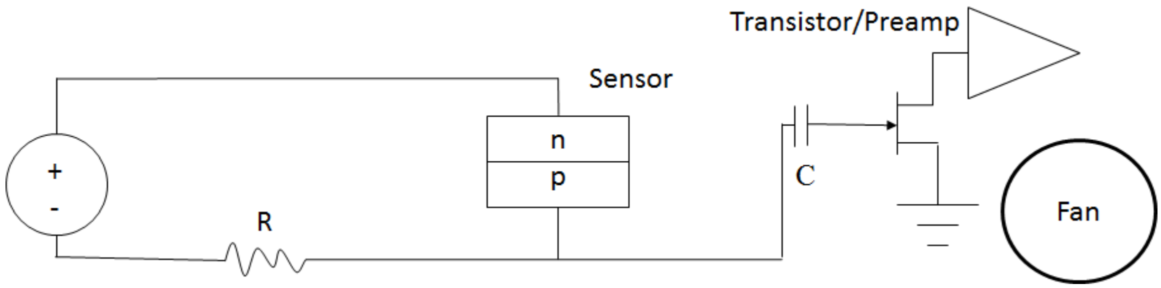

Figure 13: The modified circuit diagram for the UCS. Note that the capacitor/resistor series has been removed.

7.4.4 Noise Measurements in the Upgraded Characterization Station

The UCS has four potential sources of noise. The first is the pole-wires, which the modified PCB is meant to correct. The second is the readout electronics, most notably the type 2SK152 FET; this transistor is the primary source of noise from this section, while the A275[20] and A250[21] electronics produce very little noise, per their specifications. The third is the fan and cooling apparatus. The electronics from this system may create a non-negligible amount of radiative noise, while fans are known to create mechanical noise, which turns into electronic noise. This source of noise could be mitigated by exchanging the current air-cooling fan for a liquid cooling system. The final major source of noise in the UCS derives from leakage current in the sensor itself. This noise source cannot be mitigated, as it is integral to the sensor.

The new PCB was operated under several conditions. The first condition measures the noise from the system alone, without either of the PCBs attached. The second consists of three measurements: the noise from the system when the old PCB is attached, when the new PCB is attached, and when the new PCB is attached and the

LEMO connector soldered on, but the LEMO cable is not in place. The sensor was not connected to the readout during any of these measurements. These four measurements can be found in Figure 14, and as can be seen they are nearly identical, as one would expect. This is because, in each case, the noise is sourced solely from the preamplification section of the UCS. The noise from the system can be calculated from the Gaussian standard deviation σ, as the full-width at half-maximum (FWHM): $2\sqrt{2\ \ln 2} * \sigma$. The LabVIEW code that runs the UCS automatically calculates the σ as a part of its process, and the value it finds can be found at the top of each image in Figure 14. The standard deviations are 1.85, 1.85, 1.88, and 1.88 mV, corresponding to a FWHM of 4.36, 4.36, 4.43, and 4.43 mV respectively. The difference is split between no board/the old board, the first two, and the different states of the new board, the latter two. This tiny increase in noise is thought to be a consequence of the traces on the new PCB being substantially closer than those on the old one, leading to some small increase in capacitance. Regardless, this difference in noise is at the limit of what the UCS can measure, and is not considered significant.

Once the sensor is attached, we examine both signal and noise simultaneously. Noise measurements are taken when the board and sensor are attached, the sensor is biased, and a 1 millicurie Strontium-90 source is applied to the sensor. This is in part to ensure that anything done to reduce the noise doesn't also decrease the signal by a corresponding degree. The thermal noise and noise from leakage current from the sensor is an integral part of the readout noise. The signal is produced when a minimum ionizing particle from the Strontium-90 source passes through the sensor, generating a pulse of ~20,000 electrons (35-40 mV after amplification), in coincidence with a hit in the plastic scintillator directly beneath the sensor, attached to a photomultiplier tube. This pulse of charge flows through a 10 nF AC coupling capacitor – sized in such a way that it appears as a short circuit to the charge pulse but an open circuit to the DC sensor bias current – and is collected by the preamplifier. The preamplifier then outputs a voltage signal, proportional to the amount of charge from the sensor, which is shaped by the electronic

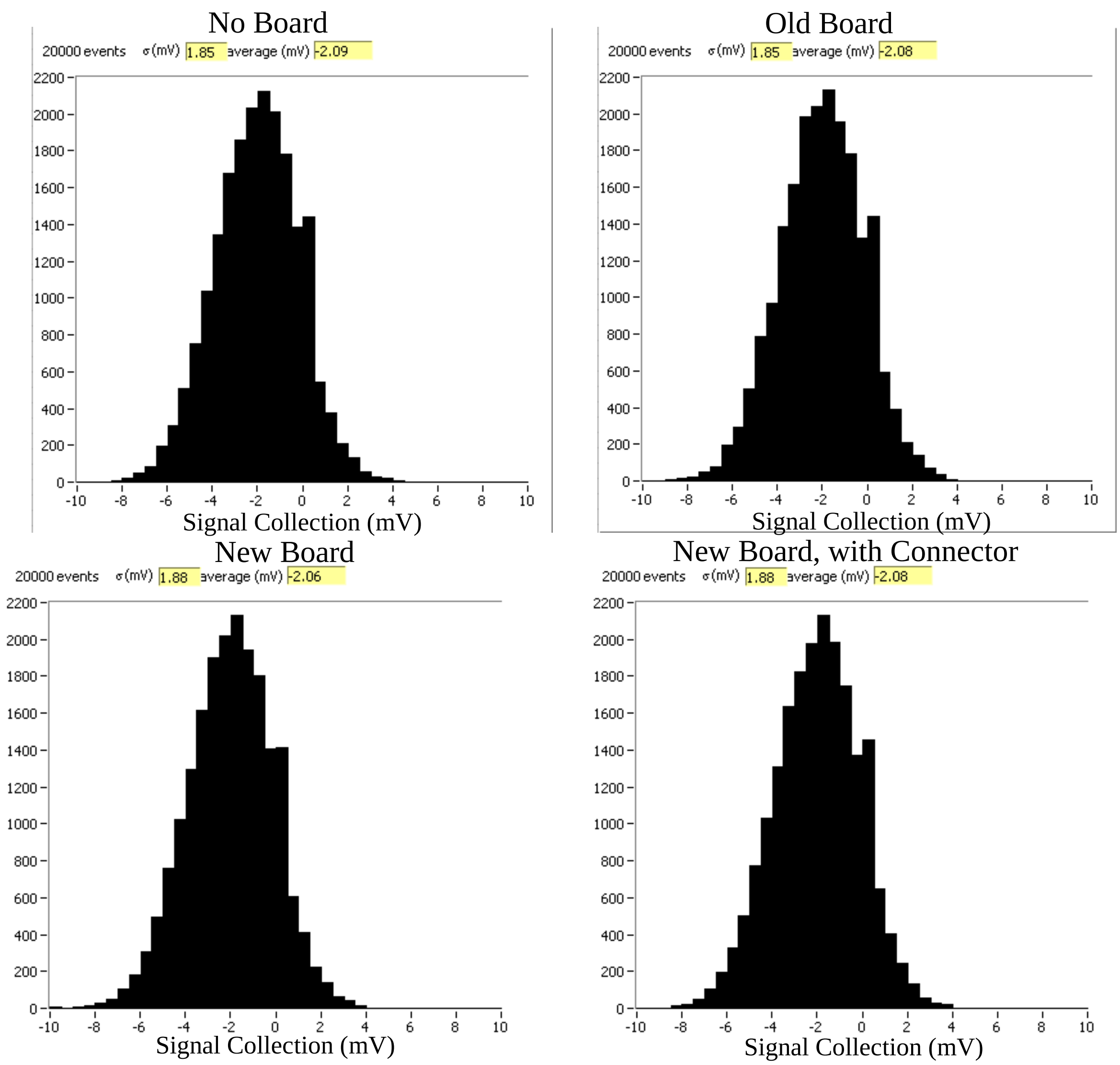

Figure 14: The signal from the UCS when no board was attached, when the old board was attached, when the new board was attached, and when the new board was attached with the coaxial connector soldered on. None of these measurements included a sensor.

filters, and then routed to the DAQ box for further shaping. The DAQ box performs analog/digital conversion of the signal, and sends it to the computer and LabVIEW program. It is during this process, where the signal proceeds from the sensor to the computer, that noise is picked up; that is, the electronics (which include capacitors, resistors, and various unshielded sections where radiated or conducted noise can be picked up) generates a “signal” that does not originate from a coincidence between the sensor and PM. The noise takes the form of a Gaussian peak to the right of the main, Landau-shaped signal in a histogram of the voltage change (in millivolts) of the incoming signal from the UCS (Figure 15). Unlike the noise in Figure 14, the Gaussian σ is not calculated directly by the LabVIEW code, but must instead be found through the fitting of a Gaussian curve to the noise. This is also shown in the right-hand plot of Figure 15; the $\chi^2 = 0.85$ for this fit, while the $\sigma = 4.19$ mV, giving a FWHM of 9.87 mV. The position of the Landau signal, to the left or right of the Gaussian noise, is dependent on the direction in which the sensor has been biased. It is important to ensure that the signal-

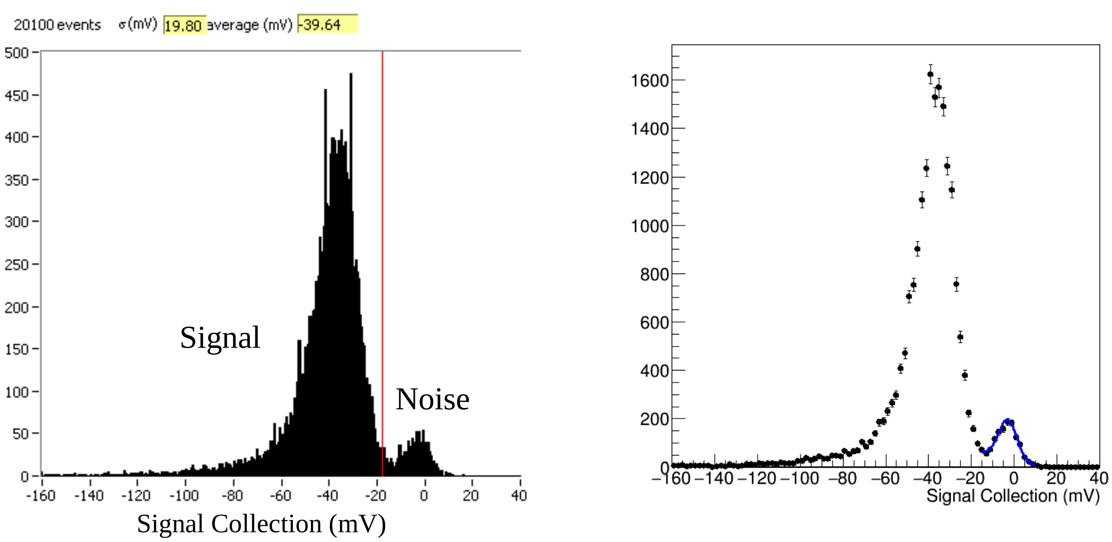

Figure 15: The left image is the signal and noise from the UCS when the board and sensor are attached and biased and a source of ionizing particles is supplied; the red line is a cursor. The right image is a fit of the noise curve.

to-noise ratio, the absolute value of the most probable value of the Landau divided by the mean of the Gaussian, is as high as possible; i.e., that the charge pulse from the signal is greater than that from the noise.

As this is a histogram, the amplitude represents how many hits were achieved at a given voltage (mV), or how many hits were detected at a given charge pulse. While the amplitude is not directly useful, its distribution allows one to find the most probable value of the Landau signal, and the mean of the Gaussian; from this millivolt value, it is possible to determine the average number of electrons coming from the signal and the noise. The standard deviation, or sigma, of the curve, informs the reader of the spread of the noise and signal as a function of voltage; Landau fluctuations – a consequence of the statistics of the physical energy distribution as beta particles from the Strontium-90 source pass through the material of the sensor – means that the resulting ionization creates a spread of signals across the horizontal axis. The same is true of the noise, although the spread is caused by varying leakage currents, thermal effects in the sensor and electronics, and changing RF electric fields in the interior of the UCS. This is important because in some sensors the width of the noise can grow to the point where it swamps the signal, making it impossible to separate them. In the case of the type of sensor shown in Figure 15, a 220 μm planar silicon sensor, the signal is large enough that it can be easily separated from the noise; however, in diamond sensors, the signal is so small that it can’t be easily disentangled. Thus, reducing the noise from extrinsic sources is critical to proper experimentation with diamond sensors.

In a third study, the sensor is connected to the readout and bias circuitry, but no bias voltage is applied. While it was known that the LEMO cables connecting the sensor to the high voltage and readout amplifier would add capacitance to the system, the dependence of the UCS amplifier noise on capacitance was not well-understood; as such, the bypass had to be installed blind, without knowing what effect it would have on the noise beforehand. Measurements were taken both for the original and new PCBs. These measurements can be found in Figure 16. The widths of the two graphs are fairly close, indicating a similar level of noise between the new and old system when the sensor is unbiased. In this case, the width of the Gaussian has expanded substantially relative to Figure 14; this is because the amplifier is now being loaded by the capacitance of the sensor.

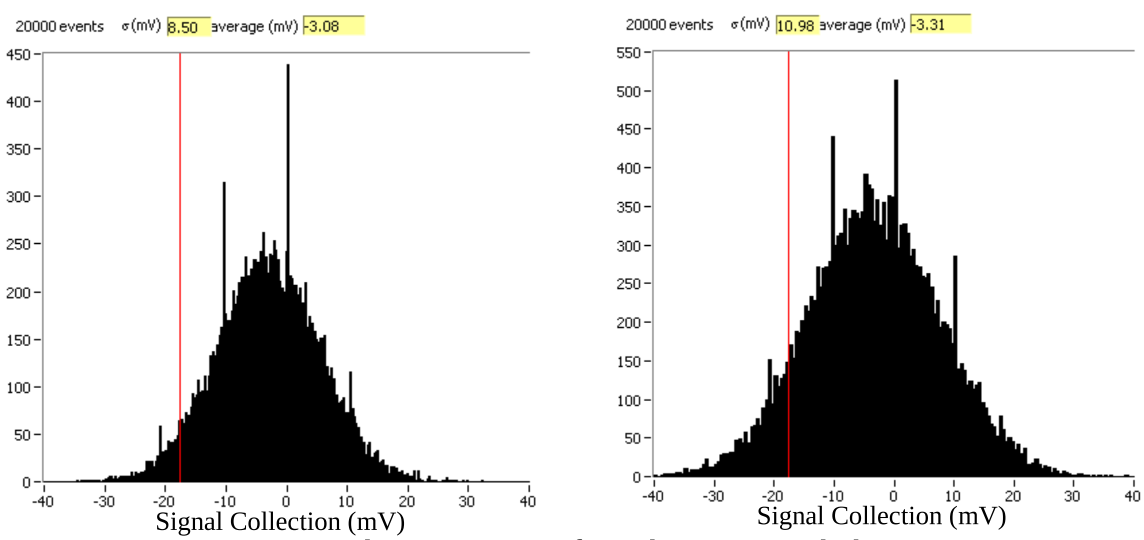

Figure 16: Signal measurements from the system with the sensor attached, but with no bias voltage applied. The graphs are from the original board (left) and the new (right).

In a fourth study, an 11 V reverse bias is applied. The resulting measurements from the old and new PCBs can be found in Figure 17, and as before are nearly identical. When the sensor is biased, the capacitance of the sensor is reduced, reducing the overall noise.

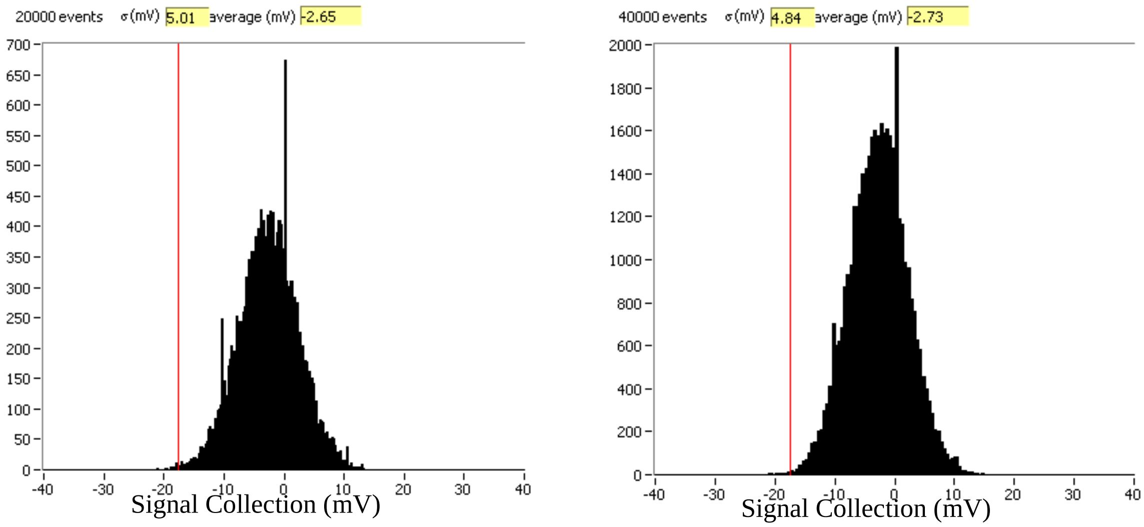

Figure 17: The signal from the system with the sensor attached and a +11 V bias applied. The graphs are from the old board (left) and the new (right).

The final study was a measurement of the noise from the entire, biased system when the 220 μm planar silicon sensor was being excited by the 1 millicurie Strontium-90 source. The results of the two measurements can be found in Figure 18. The graph on

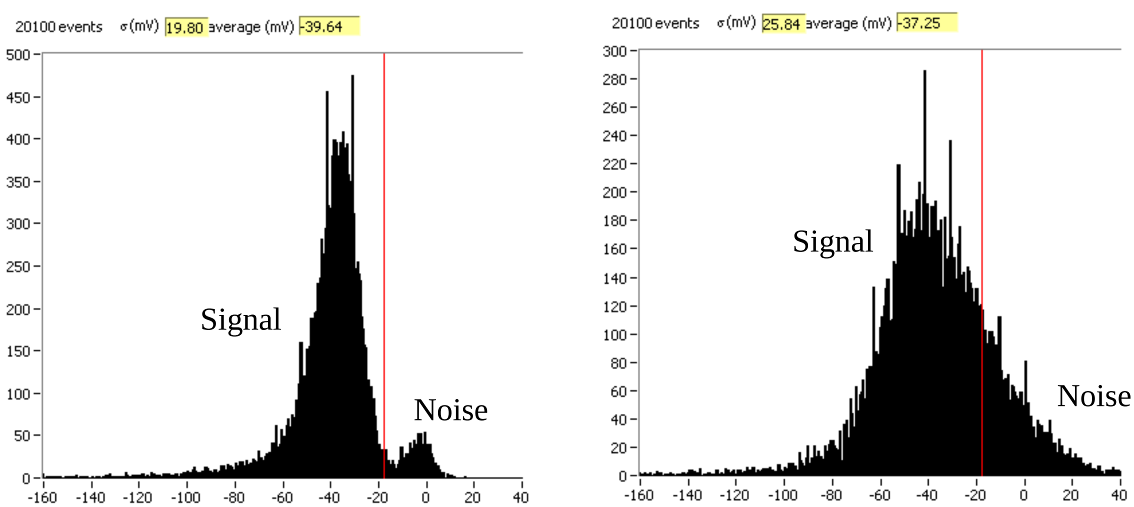

Figure 18: Signal and noise measurements with the sensor attached, the bias applied, and a source irradiating the sensor. The left represents the original board without the coaxial bypass, and the right, the new board with the coaxial bypass. Note that the signal has expanded and swamped the noise bump in the right-hand image. The new board and coaxial cable does not reduce the noise.

the left, from the original PCB is what we would expect[22], comprised of a large signal in the form of a Landau curve and a smaller Gaussian curve, the noise.

The right-hand image in Figure 18 shows the same measurement, but using the new board. Note how the signal and noise distributions have become overlapped. The reason for this is not understood, but the signal appears to be in approximately the same place as it is for the old board. Thus, it does not appear as if the new PCB configuration has a better signal-to-noise ratio than the old PCB configuration.

The fan is another potential contributor of noise in the UCS. Measurements were taken with the original PCB configuration when the fan was both on and off; as the fan did not have a power switch, it was turned on and off using an alligator clip clamping its power wire. The result, and the fits of the noise curves, can be seen in Figure 19. The fit of the Fan Off noise curve has a σ of 5.00 mV, giving a FWHM of 11.77 mV at $\chi^2 = 3.60$, while the Fan On noise curve has a σ of 5.07 mV, a FWHM of 11.93 mV, and $\chi^2 = 5.79$. Thus, the fan is not observed to be a significant source of noise.

Cooling electronics can reduce their noise. However, cooling them to the point that there is a significant impact on the noise usually requires that the temperature be reduced below the freezing point, which can result in condensation and damage. To avoid condensation, the interior is usually purged with nitrogen gas, to displace the humid local atmosphere. The FET was cooled using two different techniques: a stream of cold high-pressure nitrogen gas, and dry (CO_2) ice placed directly on the transistor.

A stream of cold high-pressure nitrogen gas generated by an N_2-fed vortex tube was applied through an opening in the UCS, using a Loc-Line flexible tube (Figure 20) to

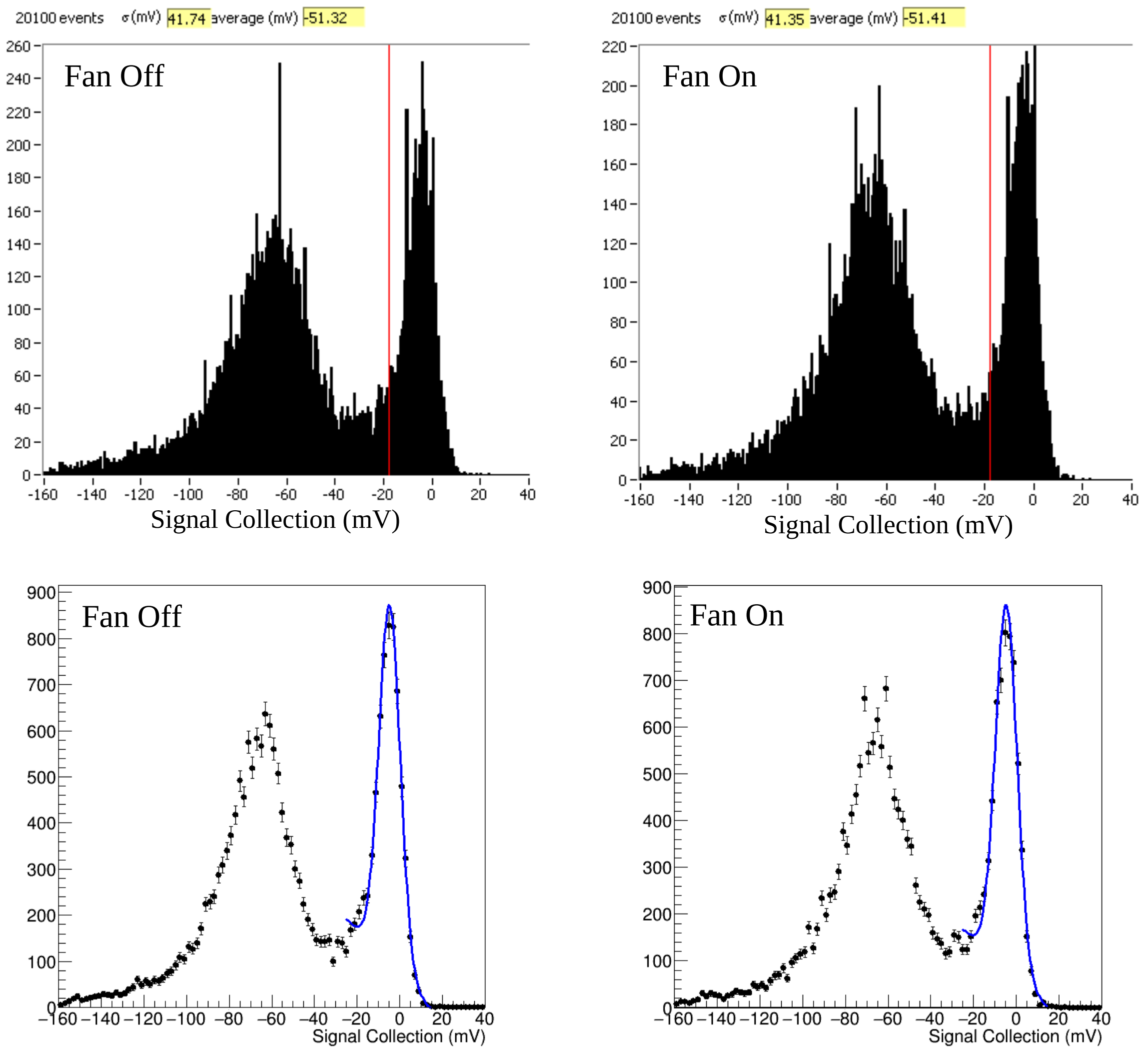

Figure 19: Signal and noise measurements with the fan on and off (top) and the fits of the noise (bottom). Note that these measurements are nearly identical. The original planar silicon sensor was damaged while being moved between PCBs, and was replaced with a 3D sensor[23], which has different noise characteristics.

direct the nitrogen stream toward the FET. The stream was at 70 PSI, and after five minutes had reduced the stream-side of the transistor to -2.5° C, and the other side to -1.5° C. Room temperature was ~23° C. The result of this noise measurement, and the fit of the noise curve, from experiment can be found in Figure 21. The fit of the noise curve has a σ of 4.86 mV, giving a FWHM of 11.44 mV at $\chi^2 = 5.60$. Comparing this noise measurement to the Fan On measurement of Figure 19 (the default state of the UCS),

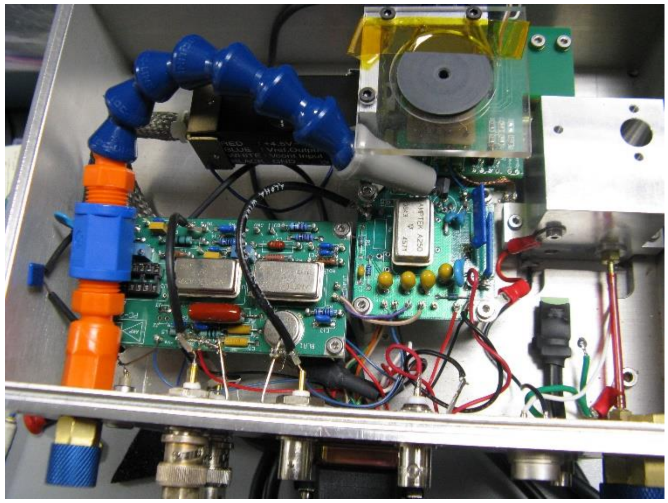

Figure 20: The Loc-Line flexible tube, used to direct the nitrogen stream towards the FET.

using nitrogen to reduce the temperature by 25° C reduced the noise by 0.49 mV, ~4%, and therefore did not have a significant (>10%) effect on the noise; thus we applied dry ice directly to the transistor, to cool it further and examine the result.

The transistor has a small surface area, about 20 mm^2 per face, and extends about a half centimeter above the rest of the electronics. Further, the transistor does not have any nearby supporting structure on which to rest a chip of dry ice. In order to hold the dry

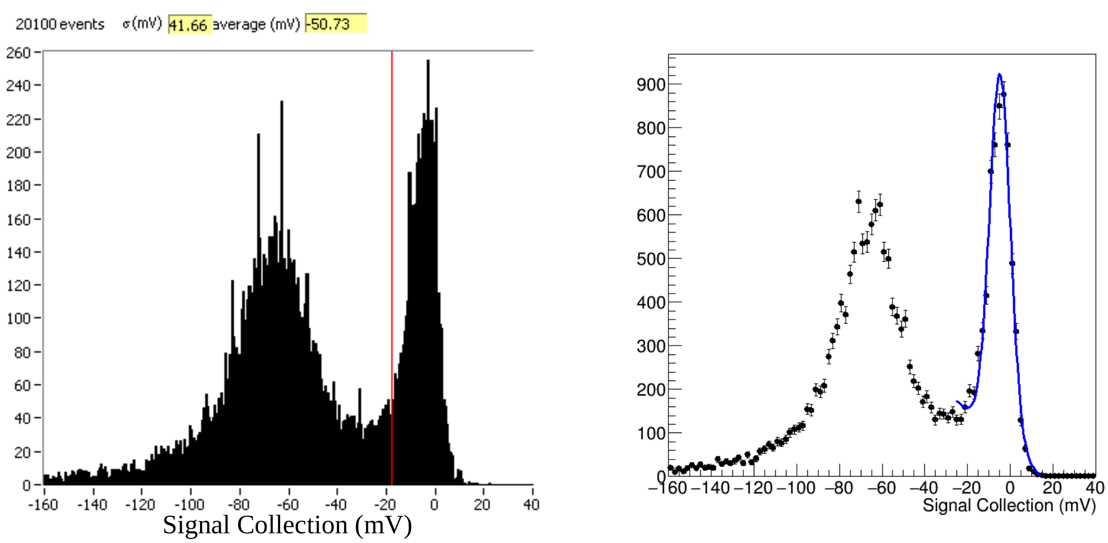

Figure 21: Signal and noise measurements with a nitrogen stream and its corresponding noise fit.

ice, a small plastic cup was wrapped around the transistor (Figure 22) and filled with powdered dry ice. This cooled the transistor to a temperature of -75° C. The result of this experiment and its noise fit can be seen in Figure 23. Despite the change in vertical scale, a careful examination of both plots shows that the peaks of the Landau and Gaussian curves have roughly the same relative height, with the difference being created by fluctuations in the data. The fit of the noise curve has a σ of 4.88 mV, giving a FWHM of 11.49 mV at $\chi^2 = 3.61$, a decrease in the noise inferior to that of the nitrogen stream. This inferior performance is due to the dry ice powder evaporating before the measurement was completed. A similar experiment was attempted using a solid piece of dry ice, but this resulted in transistor failure. There is a gap here between the amount of cooling that can be performed by a dry gas stream, and a piece of dry ice; other methods exist, such as using specialized refrigerators, but the need to cool the FET and not cool other, more temperature-sensitive electronics makes them non-viable. Consequently, the only method remaining is to add an additional electronic noise filter.

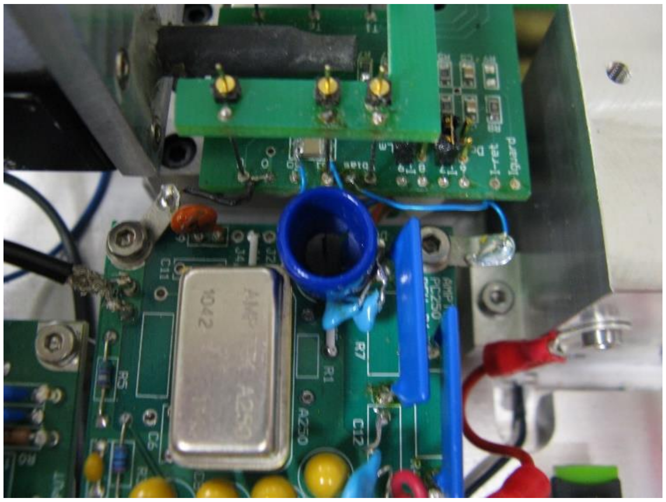

Figure 22: The plastic cup made to hold dry ice powder, currently empty. The FET can be seen inside the cup.

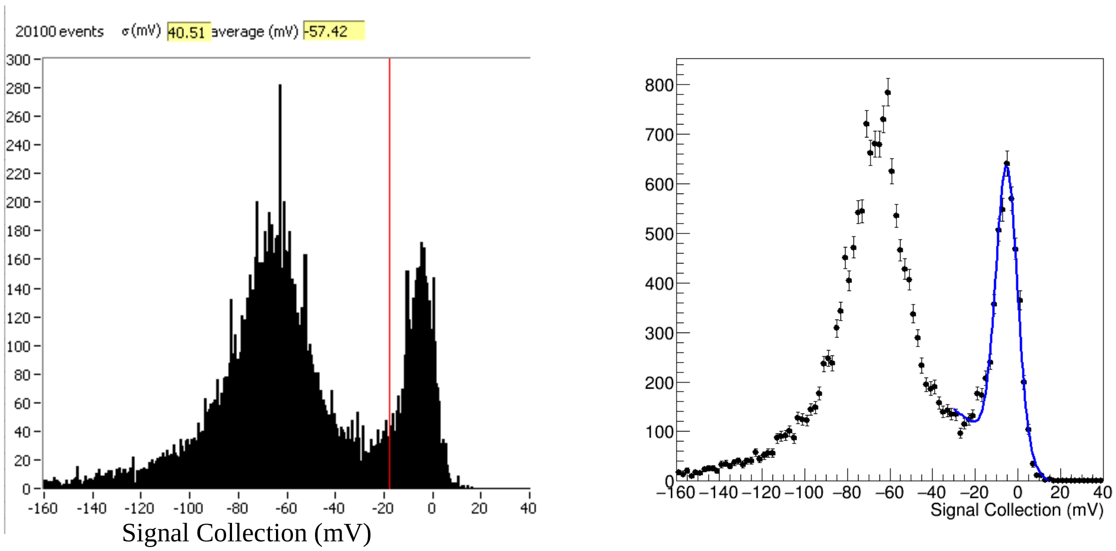

Figure 23: A noise measurement, and its fit, after the plastic cup was filled with powdered dry ice. The ice evaporated before the experiment was finished.

None of the methods described here have been successful in reducing the noise in the UCS. The new PCB exhibited approximately the same amount of noise as the old PCB. Disabling the system's fan, in an effort to eliminate noise from the motor, did not have a significant effect on the noise from the system. Finally, cooling the FET in the UCS using a nitrogen stream and dry ice did not reduce the noise to a sufficient degree. Therefore, the only other available possibility to reduce the noise is to add an additional electronic noise filter. The UCS by default has two electronic noise filters, in the form of two A275 pulse amplifiers. Adding a new A275 is simply a matter of plugging it in, in series with the other two.

7.4.5 Application to Proton Irradiations

While the modified PCB was originally designed for use in the Upgraded Characterization Station, it also found use in an experiment at LANSCE in a study of the effects of irradiating a silicon sensor while the sensor was biased. The sensors in question needed to be biased from the top and the bottom, and the modified PCB was designed for this purpose – the central hole was made so that wire bonds could be attached to the bottom of such sensors.

The particular type of sensor that was being examined was a 3D sensor, a type of sensor in which the electrodes, instead of being implanted on the surface, are perpendicular, penetrating into the substrate of the sensor. The reason for making a sensor with this configuration is that this geometry makes the sensor considerably more radiation hard, as it is possible to make the distance between electrodes small enough that the effect of charge trapping on the signal is suppressed, even for very large radiation fluences. More details can be found in [23,24]. The study was focused primarily on characterizing the electrical behavior of 3D diodes.

During irradiation, the bias voltage was applied with a wire bond attached to the n-side (top) through the grounding pad, and to the p-side (bottom) of the 3D diode through the central hole of the PCB. The diodes are sensitive to light; it was necessary to cover them with dark plastic covers, attached by Kapton tape (Figure 24).

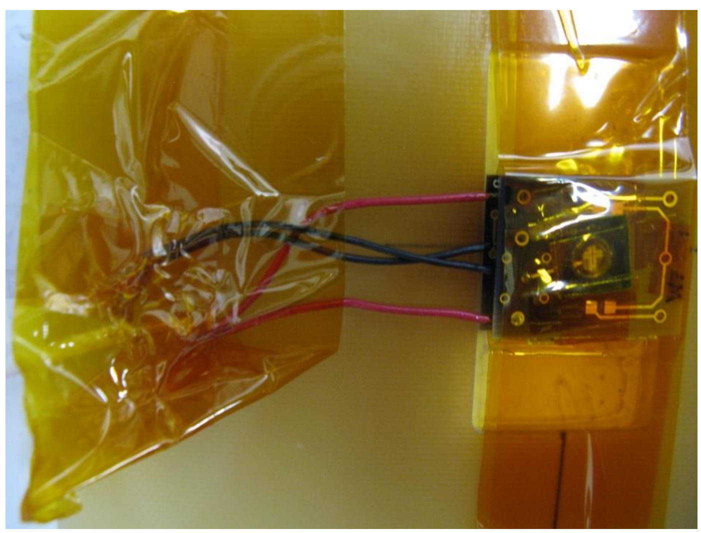

Figure 24: The irradiated sensor, encased in plastic and Kapton tape. The wires on the left are for the purposes of biasing the sensor during irradiation.

7.5 References

1. http://rd50.web.cern.ch/RD50/NIEL/default.html
2. RD2 Collaboration (1995). Fluence and Dosimetric Measurements For a $\pi^{\pm}$ Irradiation Facility. Nucl. Phys. Proc. Suppl. 44, 503-509.
3. Blokland, Willem, Dey, Joseph, & Vogel, Greg (1997). A New Flying Wire System for the Tevatron. Proceedings of the 17th IEEE Particle Accelerator Conference (Vancouver), Ed. M. Comyn et al., C970512, 2032 (1997).
4. Glaser, M., Ravotti, F., & Moll, M. (2006). Dosimetry assessments in the irradiation facilities at the CERN-PS accelerator. IEEE Trans. Nucl. Sci., 2016-2022.
5. Bisello, D., Candelori, A., Kaminsky, A., Pantano, D., & Wyss, J. (2001). Radiation damage of standard and oxygenated silicon diodes irradiated by 16-MeV and 27-MeV protons. IEEE Trans. Nucl. Sci. 48, 1020-1027.
6. Palni, Prabhakar, et al (2013). A Method for Real Time Monitoring of Charged Particle Beam Profile and Fluence. Nucl. Instr. And Meth. A, Vol. 735, 213-217.
7. http://www.mouser.com/ds/2/311/BPW%2034%20F,%20Lead%20(Pb)%20Free%20Product%20-%20RoHS%20Compliant-369678.pdf
8. A. B. Rosenfeld, et al. (2003). Neutron Dosimetry With Planar Silicon p-i-n Diodes. IEEE Trans. Nucl. Sci. vol. 50 (6), pp. 2367 - 2372.
9. http://www.tek.com/sites/tek.com/files/media/media/resources/Series_2400_DS_041216.pdf
10. http://exodus.poly.edu/~kurt/manuals/manuals/Keithley/KEI%20706%20Instruction.pdf

11. http://www.ni.com/labview/

12. Taddeucci, T.N., Ullmann, J., Rybarcyk, L.J., Butler, G.W., and Ward, T.E. (1997). Total cross sections for production of ^{7}Be, ^{22}Na, and ^{24}Na in p + ^{7}Li and p + ^{27}Al reactions at 495 and 795 MeV. Phys. Rev. C 55, 1551–1554.

13. Morgan, G. L. *et al* (2003). Total cross sections for the production of ^{22}Na and ^{24}Na in proton-induced reactions on ^{27}Al from 0.40 to 22.4 GeV. Nucl. Instrum. Methods Phys. Res. B 211, 297–304.

14. Palni, Prabhakar (2014). Evidence for the Heavy Baryon Resonance State Λ_b^{*0} Observed with the CDF II Detector, and Studies of New Particle Tracking Technologies Using the LANSCE Proton Beam. University of New Mexico Ph.D. Dissertation, http://digitalrepository.unm.edu/cgi/viewcontent.cgi?article=1051&context=phyc_etds.

15. Hartjes, Fred (2011). Design plans of Nikhef characterisation station. http://www.nikhef.nl/~i56/ (Note that the manual and associated files may be found under Documentation).

16. Josey, Brian P. (2012). Charge Collection Distance of Diamond Vertex Detectors. University of New Mexico Honors Thesis, http://physics.unm.edu/pandaweb/undergraduate/programs/honorsThesis/2012_Josey.pdf.

17. Cullen, Don et al. (2001). Effects of Surface Finish on High Frequency Signal Loss Using Various Substrate Materials. IPC EXPO.

18. http://www.appliedkilovolts.com/docs/datasheets/HPZ.pdf

19. http://www.tek.com/sites/tek.com/files/media/document/resources/2410RevD_DocSpec.pdf

20. http://amptek.com/products/a275-pulse-amplifier/

21. http://amptek.com/products/a250-charge-sensitive-preamplifier/

22. https://www.digchip.com/datasheets/parts/datasheet/192/2SK152-pdf.php

23. Parker, S. et al. (1997). A proposed new architecture for solid-state silicon detectors. Nucl. Instrum. Meth. A 395, 328.

24. Spieler, Helmuth. "Electronic Noise." Semiconductor Detector Systems. Oxford: Oxford UP, 2005.

Chapter 8: Conclusions and Outlook

Motivations for a search for the supersymmetric $B_s \to \mu^+\mu^-\mu^+\mu^-$ decay have been presented. A trigger study was performed, evaluating signal efficiency and background suppression for the twelve triggers being used in this analysis. Using Monte Carlo simulations, major background decays were identified and studied. Of the seven background decays studied, the SM $B_s \to 4\mu$, $B_s \to \varphi(\to KK)\mu\mu$, $B_d \to \omega(\to \pi\pi)\mu\mu$, $B_d \to \rho^0(\to \pi\pi)\mu\mu$, $B_s \to \psi(2S)(\to \mu\mu)K^*(\to K^+\pi^-)$, $B_s \to J/\psi\,(\to \mu\mu)\varphi(\to \mu\mu)$, and $B_d \to K^*(\to K^+\pi^-)\mu\mu$, with hadronic tracks misidentified as muons, the largest contributors are the $B_s \to J/\psi\,\varphi$, followed by the $B_d \to K^*\mu\mu$. The former can be eliminated by applying window cuts around the mass of the J/ψ and φ. By excluding any B events with daughters in a 5σ window around the mass of the J/ψ (±312 MeV) and the φ (±121.5 MeV), this background is reduced by a factor of ~10^6, far below the level of the signal. The $B_d \to K^*\mu\mu$ background can be eliminated in two ways: using a similar mass window cut around the mass of the K^* (±139.41 MeV, in this case), or by creating a fit of the background's mass curve, and subtracting the fit from the collision data. The next step is to study combinatorial and non-b-decay backgrounds and to perform the fine background reduction, by using neural network Boosted Decision Tree techniques to find the optimal selection criteria. After that has been completed, research on the collision data using these criteria can begin. That is beyond the scope of this dissertation.

A project to refine the High-Level Trigger of the ATLAS Experiment was completed. This project focused on the B-Triggers, triggers made to save events including a bottom quark. About 10% of these events produce a J/ψ meson as part of their decay, which itself produces a clean, strong dimuon signal for detection; this project focused on optimizing one of the J/ψ vertex selection criteria, the cut on the J/ψ χ^2, which describes the vertex quality. This was studied for both Run-1 (2012) and Run-2 (2015) data. Based on the results of the studies, it was recommended that the J/ψ χ^2 cut be reduced from $\chi^2 < 20$ to $\chi^2 < 10$, and the corresponding trigger was integrated in parallel with the original selection criteria. Furthermore, for Run-2, signal efficiency, background rejection, and signal efficiency vs. background rejection plots were created to guide strategy for the future. As part of the studies, correlation plots between various High Level Trigger data (such as mass, kinematics, geometry, and so on) and the J/ψ χ^2 were studied, to determine if there was any significant dependence of the J/ψ χ^2 on other terms; no such correlation was found. Finally, a study of IBL data in Period H – during which the IBL was on only intermittently – showed that the J/ψ χ^2 vertexing efficiencies did not vary significantly based on the state of the IBL.

A diode array designed for rapid real-time monitoring of the fluence from a charged particle beam was presented, along with a description of the code needed to run the array. The ability to measure fluences in real time is invaluable in the development of new radiation-hard technologies intended for environments like that in detectors at the LHC. The diode array can be enhanced further by using either smaller and more closely-spaced diodes, to decrease pitch and increase resolution, or by using more radiation-hard diodes (such as diamond or 3D), to increase radiation hardness and make the array viable for higher fluences, in the range beyond 10^{15} neq/cm^2.

An attempt was made to reduce the noise of the Upgraded Characterization Station, a device that can be used to measure how a sensor's efficiency changes with radiation damage, in order to make the study of lower-signal sensors (such as diamond) feasible. Attempts were made to reduce noise from thermal and radiative sources, including designing a new PCB that could bypass certain exposed wires. None of these methods were successful in reducing the noise by more than 10%. The next recommended step is to attach a third Amptek A275 Pulse Amplifier in series. The PCB was used successfully in an experiment to irradiate a silicon sensor while the sensor was biased.

Appendix A: Results of Fits to Monte Carlo Event Distributions

Three different fits have been presented in this dissertation: the fits of the mass of the K^*, the B_d, and the B_s. These were performed using RooFit. Presented here are the values that were put into the RooFit code to achieve the fits.

The K^* mass fit used a Gaussian and a Landau curve added together; the values of the fitting parameters can be found in Table 1. Note that the two parameters of the Landau distribution, the location parameter and the scale parameter, are called "mean" and "sigma" in RooFit. The standard deviation for distributions like the Gaussian and Crystal Ball functions are called "sigma" in RooFit. Upper and lower bounds must be provided to RooFit for these functions for the fit to converge; these bounds are given here.

K^* Mass	RooGaussian		
Parameter	Value	Upper Bound	Lower Bound
Mean	883.14	884	882
Sigma	46.47	47	46
	RooLandau		
Location Parameter	893.017	894	892
Scale Parameter	13.111	13.2	13.0
	Fraction		
K	0.3611	0.364	0.359

Table 1: The fitting parameters for the K^* mass. These are the parameters used for the fit presented in Figure 5.7.

The fitting parameters for the B_d mass can be found in Tables 2-4. As before, the upper and lower bounds are provided, for the purpose of replicating the fit in RooFit.

B_d Mass	RooCBShape (Crystal Ball)		
Parameter	Value	Upper Bound	Lower Bound
Mean	5051.92	5054	5050
Sigma	140.311	142	139
α	0.7843	0.865	0.703
n	7.5405	23.9	-8.73
	RooGaussian		
Mean	5130.39	5132	5129
Sigma	60.6311	62	59
	Fraction		
P_{B_d}	0.875065	0.884	0.866

Table 2: The fitting parameters for the B_d mass, peak, corresponding to Figure 5.11.

B_d Mass	RooExponential 1		
Parameter	Value	Upper Bound	Lower Bound
Exponent a	0.00756955	0.00758	0.00756
	RooExponential 2		
Exponent b	0.00205961	0.00208	0.00204
	RooExponential 3		
Exponent c	0.00205961	0.00208	0.00204
	Fraction		
$L_{B_d,1}$	0.999814	0.999817	0.999811
$L_{B_d,2}$	0.260287	0.500	0.021

Table 3: The fitting parameters for the B_d mass, left sideband. This corresponds to the fit in Figure 5.12.

B_d **Mass**	RooGaussian		
Parameter	Value	Upper Bound	Lower Bound
Mean	4003	6300	1700
Sigma	289	322	256
	RooPolynomial (3rd Order)		
a_1	43078	43200	43000
a_2	-14.1283	-14.10	-14.2
a_3	0.0011963	0.00120	0.00119
	Fraction		
R_{B_d}	0.999858	0.9999	0.9998

Table 4: The fitting parameters for the B_d mass, right sideband, corresponding to Figure 5.13.

The fitting parameters for the B_s mass can be found in Tables 5-7, and as before the upper and lower bounds are provided.

B_s **Mass**	RooBreitWigner		
Parameter	Value	Upper Bound	Lower Bound
Mean	5367.6	5380	5350
g	145	154	136
	RooGaussian		
Mean	5354	5380	5330
Sigma	60.8	69.8	51.8
	Fraction		
P_{B_s}	0.875383	0.892	0.859

Table 5: The fitting parameters for the B_s mass, peak. These parameters created the fit in Figure 5.15.

B_s Mass	RooGaussian		
Parameter	Value	Upper Bound	Lower Bound
Mean	6490.06	8530	4450
Sigma	273.111	306	241
	RooPolynomial (3rd Order)		
b_1	117.748	150.	86.0
b_2	0.047535	0.0829	0.0122
b_3	0.0000111111	0.0000135	0.00000879
	Fraction		
L_{B_s}	0.999939	0.99995	0.99993

Table 6: The fitting parameters for the B_s mass, left sideband. These fitting parameters were used to construct the fit in Figure 5.16.

B_s Mass	RooGaussian		
Parameter	Value	Upper Bound	Lower Bound
Mean	5257.28	5330	5190
Sigma	97.4294	112	83.6
	RooExponential		
Exponent d	-0.005887	-0.00517	-0.00662
	RooPolynomial (3rd Order)		
c_1	-10635.4	-9890	-11400
c_2	1.15947	1.29	1.03
c_3	0.00022909	0.000256	0.000202
	Fraction		
$R_{B_s,1}$	0.0255336	0.0263	0.0248
$R_{B_s,2}$	0.997947	0.998	0.997

Table 7: The fitting parameters for the B_s mass, right sideband, corresponding to Figure 5.17.